

2014

Developing A Stable Lattice Boltzmann For Computational Dynamics Applications

Saeed J. Almalawi
Lehigh University

Follow this and additional works at: <http://preserve.lehigh.edu/etd>



Part of the [Mechanical Engineering Commons](#)

Recommended Citation

Almalawi, Saeed J., "Developing A Stable Lattice Boltzmann For Computational Dynamics Applications" (2014). *Theses and Dissertations*. Paper 1411.

This Dissertation is brought to you for free and open access by Lehigh Preserve. It has been accepted for inclusion in Theses and Dissertations by an authorized administrator of Lehigh Preserve. For more information, please contact preserve@lehigh.edu.

**DEVELOPING A STABLE LATTICE BOLTZMANN METHOD FOR
COMPUTATIONAL FLUID DYNAMICS APPLICATIONS**

By

SAEED J. ALMALOWI

Presented to the Graduate and Research Committee
of Lehigh University
in Candidacy for the Degree of
Doctor of Philosophy

In

Mechanical Engineering

Lehigh University

(January 2015)

COPYRIGHT (SAEED J. ALMALOWI)

(2015)

Approved and recommended for acceptance as a dissertation in partial fulfillment of the requirements for the degree of Doctor of Philosophy.

Date

Prof. Alparslan Oztekin

(Committee Chair)

Accepted Date

Committee Members:

Prof. Jacob Kazakia

Dr. Justin Jaworski

Dr. Keith Moored

Dr. Muhannad Suleiman

ACKNOWLEDGMENT

I would like to express my special thanks of gratitude to my supervisor Prof. A. Oztekin as well as our principals: Prof. J. Kazakia, Dr. J. Jaworski, Dr. M. Suleiman, and Dr. K. Moored who gave me the golden opportunity to do this wonderful research on the topic of advanced numerical simulation using LBM, which also guided me at every step in this research. I came to know about so many new things and I am really thankful to them.

Secondly, I would also like to extend my thankful to my parents who helped me a lot to finish this research within limited time. I will not forget my wife (Maryam) and my two sons (Wesam and Roselyn) for their patience during this time of research. I owe a lot for them.

I would like to thank the Saudi Arabian government and Taibah University for their financial support during my graduate study.

My final thanks go to all the people who are actively involved in my life and stay behind it.

I conducted this research not only to earn a degree but also to increase my knowledge.

THANKS AGAIN TO ALL WHO HELPED ME.

ACKNOWLEDGMENT	iv
LIST OF FIGURES	vii
LIST OF TABLES	xi
NOMENCLATURE.....	xii
ABSTRACT.....	1
CHAPTER 1: MOTIVATION AND OBJECTIVES.....	3
1.1. Motivation and Objectives.....	3
1.2. Background	4
CHAPTER 2: MATHEMATICAL MODELS.....	9
2.1. BGK Approximation -Single Relaxation Time (SRT).....	9
2.1. Multi-Relaxation Time -MRTLBM.....	13
2.3. Regularized –Lattice Boltzmann -RLBM.....	15
2.4. Regularized Multi-Relaxation Time -RMRTLBM.....	16
2.5. Multi-phase Flow Model	18
2.6. Lattices Boltzmann Arrangements.....	20
2.6.1 One Dimensional LBM Arrangements.....	21
2.6.2 Two Dimensional LBM Arrangements	21
2.6.3 Three Dimensional LBM Arrangements.....	22
2.7. Equilibrium Distribution Function.....	23
2.8. Lattice Boltzmann Domain and Physical Domain	25
2.9. Calculation of Stream Functions and Vorticity	26
2.10. Types of Boundary Conditions in the Lattice Boltzmann Method	28
2.10.1. Reflection Boundary Conditions	28
2.10.2. Periodic Boundary Conditions	29
2.10.3. Neumann Boundary Conditions.....	30
2.10.4. Symmetry Boundary Conditions	31
2.11. Spatial Discretization	31
2.12. Temporal Discretization.....	32
CHAPER 3: TURBULENT FLOWS PAST CYLINDERS	33
3.0. Objective	33
3.1. Introduction	33

3.2. A Mathematical Model	33
3.3. Results and Discussions	38
CHAPTER 4: RAYLEIGH BENARD CONVECTION	72
4.0. Objective	72
4.1. Introduction	72
4.2. A Mathematical Model	73
4.3. Results and Discussions	75
CHAPTER 5: INTERFACIAL FLOWS	81
5.0. Objective	81
5.1. Rising Droplets	82
5.1.1. Introduction	82
5.1.2. Validation Test	84
5.1.3. Single Droplet.....	90
5.1.4. Flow Structures and Flow Regimes	99
5.1.5. Two and Four Droplets	101
5.2. Rayleigh Taylor Instabilities	112
5.2.0. Objective	112
5.2.1. Introduction	112
5.2.2. Two Layers with $AR=1/3$	113
5.2.3. Two Layers with $AR=1$ and 2	115
5.2.4. Three Layers with $AR=2$	127
5.3. Three Dimensional Interfacial Flows Using D3Q19- Multi-Components –Shan and Chen Model.....	132
5.3.1. Introduction	132
5.3.2. A Mathematical Model	132
5.4.3. Results and Discussions	135
5.4. The effect of the Interactive Strength “G” and Limitations of Shan & Chen Model.....	146
CHAPTER 6: CONCLUSIONS	150
APPENDIX A	154
REFERENCES.....	159
Vita	164

LIST OF FIGURES

Figure 1. D2Q9 arrangement for lattice inside the flow domain.	10
Figure 2. D2Q9 arrangement for the lattice located on the bottom boundary.	29
Figure 3. D2Q9 periodic flow boundary condition.	30
Figure 4. A symmetry boundary condition about a symmetry line a-a'.	31
Figure 5. The schematic diagram of various geometries: a) the single cylinder, b) the inline arrangement, and c) the staggered arrangement for AR=10.	35
Figure 6. a) Instantaneous streamlines , b) instantaneous vorticity contours , and c) the lift coefficient versus the time , and d) the power spectrum of the lift coefficient at Re = 250 for a single cylinder geometry.	40
Figure 7. a) Instantaneous streamlines, b) instantaneous vorticity contours, and c) the lift coefficient vs time and the Fast Fourier Transform of the lift coefficient at Re = 50.	42
Figure 8. a) Instantaneous streamlines , b) instantaneous vorticity contours, and c) the lift coefficient vs time and the Fast Fourier Transform of the lift coefficient at Re = 100.	43
Figure 9. a) Instantaneous streamlines, b) instantaneous vorticity contours and c) the lift coefficient vs time and the Fast Fourier Transform of the lift coefficient at Re = 500.	44
Figure 10. a) Instantaneous streamlines, b) instantaneous vorticity contours and c) the lift coefficient vs time and the Fast Fourier Transform of the lift coefficient at Re = 1000.	45
Figure 11. Instantaneous streamlines and vorticity contours at various Reynolds number: a) 10000 and b) 20000 for flow past a single cylinder.	46
Figure 12. a) Instantaneous streamlines and b) instantaneous vorticity contours for flow past inline cylinders at Re =50.	48
Figure 13. The lift coefficient vs time and the FFT of the lift coefficient. The lift coefficient is calculated a) 1 st cylinder, b) 2 nd cylinder , c) 3 rd cylinder , and d) 4 th cylinder at Re = 50.	50
Figure 14. a) Instantaneous streamlines and b) instantaneous vorticity contours for the flow past inline cylinders at Re = 500.	50
Figure 15. The lift coefficient vs time and the FFT of the lift coefficient. The lift coefficient is calculated a) 1 st cylinder, b) 2 nd cylinder , c) 3 rd cylinder , and d) 4 th cylinder at Re = 100.	52
Figure 16. Instantaneous streamlines and b) instantaneous vorticity contours for flow past inline cylinders at Re = 500.	53
Figure 17. The lift coefficient vs time and the FFT of the lift coefficient. The lift coefficient is calculated a) 1 st cylinder, b) 2 nd cylinder , c) 3 rd cylinder , and d) 4 th cylinder at Re = 500.	55
Figure 18. a) Instantaneous streamlines and b) instantaneous vorticity contours for flow past inline cylinders at Re = 1000.	55
Figure 19. The lift coefficient vs time and the Fast Fourier Transform of the lift coefficient. The lift coefficient is calculated a) 1 st cylinder, b) 3 rd cylinder, and c) 4 th cylinder at Re = 1000.	57
Figure 20. Instantaneous streamlines and vorticity contours for flow past inline cylinders at a) Re =10000 and b) Re = 20000.	58
Figure 21. a) Instantaneous streamlines contour and b) instantaneous vorticity contours for flow past staggered cylinders at Re = 50.	58

Figure 22. The lift coefficient vs time and the Fast Fourier Transform of the lift coefficient. The lift coefficient is calculated a) 1 st cylinder, b) 2 nd cylinder, c) 3 rd cylinder, and d) 4 th cylinder at Re = 50.	60
Figure 23. a) Instantaneous streamlines contour and b) instantaneous vorticity contours for flow past staggered cylinders at Re =500.....	61
Figure 24. The lift coefficient vs time and the Fast Fourier Transform of the lift coefficient. The lift coefficient is calculated a) 1 st cylinder, b) 2 nd cylinder, c) 3 rd cylinder, and d) 4 th cylinder at Re = 500.	63
Figure 25. a) Instantaneous streamlines contour and b) instantaneous vorticity contours for flow past staggered cylinders at Re = 1000.....	63
Figure 26. The lift coefficient vs time and the Fast Fourier Transform of the lift coefficient. The lift coefficient is calculated a) 1 st cylinder, b) 3 rd cylinder, c) 3 rd cylinder, and d) 4 th cylinder at Re = 1000.	65
Figure 27. Instantaneous streamlines and vorticity contours for flow past staggered cylinders at a) Re =10000 and b) Re = 20000.	66
Figure 28. Strouhal number as a function of the Reynolds number for a single cylinder geometry. Line connecting triangles denotes prediction and the squares denote the experimental measurement by Davis et al. [36].....	68
Figure 29. Power spectrum of the lift coefficient in the flow past an array of staggered cylinders.	69
Figure 30. a) Instantaneous streamlines and the vorticity contours and b) power spectrum of the lift coefficient. Flow field is presented for the single cylinder geometry at Re = 21400 for BR= 1/14.	70
Figure 31. Schematic diagram of natural convection cavity for AR=1.	74
Figure 32. Schematic diagram of a Rayleigh Benard problem with AR=5.	74
Figure 33. Isotherms at Ra = 1×10 ⁵ in a square cavity.	75
Figure 34. Temperature profiles at various values of the Rayleigh number in a square cavity.	76
Figure 35. a) Streamlines and b) isotherms at Ra = 1x10 ⁵ in a cavity with AR=5.	76
Figure 36. Temperature profiles plotted in the middle of the rectangular cavity for various values of the Rayleigh number.....	77
Figure 37. The Nusselt number at the top and the bottom wall at Ra = 1×10 ⁵ in the cavity with AR=5.....	79
Figure 38. Various arrangements of droplets. F ₂ denotes the droplet of lighter fluid while F ₁ denotes heavier surrounding fluid.....	83
Figure 39. Grid optimization for the rising droplet. The shape of the droplet with different grid sizes is determined at t = 0.60 sec.	84
Figure 40. Pressure difference between the inside and the outside of the droplet vs 1/r for various droplet sizes for G = 1.6.....	85
Figure 41. Density contours for different droplet sizes at various times for a single rising droplet in an infinite domain.	86
Figure 42. The droplet speed as a function of time. The terminal speed predicted by the LBM is compared against that obtain by Davis and Taylor. [54]	89

Figure 43. Density contours of a single rising droplet in an infinite domain. Images are calculated at various times.	92
Figure 44. Density contours of a single rising droplet with no-slip boundary at the bottom and top walls. Images are calculated at various times.	93
Figure 45. Density contours for the single semi-circled droplet at various times.	96
Figure 46. a) Density contours, b) streamlines contours, c) vorticity contours, and d) pressure contours of a single semi-circled droplet placed on the lower boundary at $t = 1.17$ sec.	97
Figure 47. a) Density contours, b) streamlines contours, c) vorticity contours, and d) pressure contours of a single semi-circled droplet placed on the lower boundary at $t = 2.27$ sec.	98
Figure 48. a) Density contours, b) streamlines contours, and c) vorticity contours of a single rising droplet. No-slip boundary condition is applied at side walls and periodic boundary condition at the top and the bottom walls.	99
Figure 49. a) Density contours, b) streamlines contours, c) vorticity contours and d) pressure contours for a single droplet rising in an infinite fluid. Images are shown at $t = 1.16$ sec.	101
Figure 50. Density contours of the two vertical adjacent droplets at various times.	103
Figure 51. Density contours of two semi-circled droplet placed on the lower boundary at various times.	105
Figure 52. a). Density contours, b) streamlines contours ,c) vorticity contours, and d) pressure contours of two semi-spherical droplets placed side by side at $t = 4.12$ sec. . Error! Bookmark not defined.	
Figure 53. Density contours of four droplets at various times.	109
Figure 54. a) Streamlines contours, b) vorticity contours and c) pressure contours for four droplets rising in an infinite domain at $t = 1.47$ sec.	110
Figure 55. The equilibrium pressure and the density profiles along the center line of a droplet.	111
Figure 56. Density contours of two immiscible fluids (oil and water) at various times.	115
Figure 57. Schematic diagram of the two layers.	116
Figure 58. Density contours at various times. The blue color denotes oil while the red color denotes water. The initial disturbance is periodic with the wavelength of 3π and the amplitude of 0.001.	120
Figure 59. Density contours at various times. The blue color denotes oil while the red color denotes water. The initial disturbance is periodic with the wavelength 5π and the amplitude of 0.001.	123
Figure 60. Density contours at various time. The dark blue color denotes oil while the dark red color denotes water. The initial disturbance is introduced by pulling of the interface.	125
Figure 61. Density and streamlines contours at $t = 4.35$ sec and $t = 5.3$ sec. The dark blue color denotes oil (while the dark red color denotes water. The initial disturbance is periodic with the wavelength 5π and the amplitude of 0.001.	127
Figure 62. Density contours in three layers at various times. The lower interface is disturbed by the periodic disturbances of π wavelength and 0.001 amplitude. Periodic sided walls.	129
Figure 63. Density contours in three layers at various times. The lower interface is disturbed by the periodic disturbances of π wavelength and 0.001 amplitude. Periodic side walls.	131

Figure 64. Three Dimensional density iso surfaces at a) $t = 0$ sec, b) $t = 1.2$ sec. c) $t = 1.85$ sec d) $t = 2.13$ sec, and f) $t = 2.41$ sec. Simulations are conducted for $AR=5$ with periodic boundary conditions.....	137
Figure 65. Three dimensional density iso surfaces: a) The slice in the y-z plane at $t = 0.98$ sec, b) the slice in the x-z plane at $t = 0.98$ sec, c) the slice in the y-z plane at $t = 1.20$ sec, d) the slice in the x-z plane at $t = 1.20$ sec, e) and f) the half of the domain in the x-y plane at $t = 0.98$ sec and 1.20 sec, respectively.	139
Figure 66. Velocity vectors in the x-z plane at a) $t = 1.1$ sec and b) $t = 2.1$ sec. Periodic boundary conditions are applied at the side walls.....	140
Figure 67. The density iso surfaces: a) The slice in the y- z-plane at $t = 0.98$ sec, b) the slice in the x-z plane at $t = 0.98$ sec, c) the slice in the y-z plane at $t = 1.20$ sec, and d) the slice in x-z plane at $t = 1.20$ sec. e) and f) The density iso surfaces in the half of the domain in z-plane at $t = 0.98$ sec and $t = 1.20$ sec, respectively. The no-slip boundary conditions are applied at the side walls.	143
Figure 68. The density iso surfaces at a) at $t = 0$, b) $t = 1.85$ sec, c) $t = 2.13$ sec and d) $t = 2.41$ sec. Simulations are conducted for $AR=5$ with periodic boundary conditions at the side walls of a narrow channel.....	144
Figure 69. Velocity vectors in the x-z plane at a) $t = 1.1$ sec and b) $t = 2.1$ sec. No-slip boundary conditions are applied at the side walls.....	145
Figure 70. Density profiles for various values of “G” at the interface at $t = 0.46$ sec.	146
Figure 71. Pressure profiles across the interface for various values of “ G” at $t = 0.46$ sec.	147
Figure 72. Density profiles across the interface for various values of the relaxation frequencies and $G = 1.2$ at $t = 0.46$ sec.	148
Figure 73. Mach number profiles across the interface for various values of “G” at $t = 0.46$ sec.	148

LIST OF TABLES

Table 1.1. One dimensional lattice arrangements.	21
Table1.2. Two dimensional lattice arrangements.	22
Table 1.3. Three dimensional lattice arrangements.	23
Table 1.4. Vorticity and stream function discretization at the boundary. No-slip and periodic boundary conditions are applied.	28
Table1.5. Geometric parameters	38
Table1.6. Comparison Between the present results and pervious results.	71
Table1.7. Comparison of the average Nusselt number for $Pr = 0.71$	78
Table1.8. The values of Re and EO calculated for a single droplet rising in a heavier fluid.....	90
Table1.9. Thermo-physical properties of water and oil.	113
Table 1.10. Distribution functions at the front and the back walls.	155
Table 1.11. Distribution functions at the left and the right walls.....	156

NOMENCLATURE

f	Density distribution function
f^{eq}	Equilibrium density distribution function
\mathbf{x}	Spatial coordinate
t	time
\mathbf{e}	Lattice directional velocity
\mathbf{u}	Bulk velocity of the fluid
ρ	Density
τ	Relaxation time
w	Weighting factor
D_t	Differential operator
∂_t	Differential time operator
Δt	Differential time
ε	Small parameter
P	Pressure
c	Lattice speed
Π	Momentum tensor
C_L, C_D	Lift and Drag Coefficients
Re	Reynolds number
Ma	Mach number
MRT	Multi-relaxation time
SRT	Single-relaxation time
\mathbf{m}	Distribution moment
\mathbf{m}^{eq}	Equilibrium distribution moment
\mathcal{K}	Linear moment

M	Linear mapping tensor
EO	Eötvös number
MO	Morton number
U_t	Terminal velocity
λ	Surface tension
d	Diameter of the droplet
ψ	Potential strength
θ	Normalized temperature
θ_{ref}	Normalized reference temperature
L	Length of the domain
H	Height of the domain
Ra	Rayleigh number
J	Momentum vector
g_r	Acceleration of the gravity
Nu	Nusselt number
We	Weber number
AR	Aspect ratio
T/D	Normalized offset
S	Momentum Transformation matrix dimension
Ω	Collision term
RLBM	Regularized lattice Boltzmann
f	Frequency in Hz
ν	Kinematic viscosity [m^2/s]
ν_{lb}	Kinematic viscosity per unit lattice

Subscripts

k	Lattice branch
t_n	$n = 0, 1, 2, \dots$ order of differentiation
x	x coordinate
y	y coordinate
lb	Lattice Boltzmann parameters

Superscripts

$[n]$	$n=0, 1, 2, \dots$ order of distribution function
$[i]$	$i=0, 1, 2, \dots$ order of momentum tensor

Greek's Symbol

Δ	Difference
∇	Gradient
κ	Coloring function
ω	Vorticity
ψ	Stream functions

ABSTRACT

The lattice Boltzmann method (LBM) has been employed to investigate the temporal and spatial characteristics of complex flows. Such complex flows include turbulent flows past cylinders confined in a channel, interfacial flows of two immiscible fluids and flows driven by density stratifications. Two dimensional and three dimensional thermal lattice Boltzmann models have been developed to study non-linear dynamics of these flows. Detailed formulations of the single relaxation lattice Boltzmann method are presented. Also presented by the present author are several variations of the lattice Boltzmann method. These methods include the multi relaxation lattice Boltzmann, regularized lattice Boltzmann and thermal lattice Boltzmann. Multi relaxation time converts velocity space to moment space, and regularized lattice Boltzmann uses the non-equilibrium parts of the stress. These methods are introduced to overcome stability problem of the lattice Boltzmann method. A unique lattice Boltzmann model that combines regularized and multi-relaxation time lattice Boltzmann method is introduced here to overcome the shortcoming of the lattice Boltzmann method. It is demonstrated here that the new model is stable for high speed turbulent flows. Turbulent flow structures predicted by the proposed method agree well with those observed by the experiments and those predicted by the large eddy simulations. Spatial resolution of the turbulence resolved here is equivalent to that obtained by direct numerical simulations. A two dimensional nine velocity and a three dimensional fifteen velocity lattice Boltzmann models have been employed to study interfacial flows. Body forces and interactive forces are included in these models. Several different approaches are adopted to handle different type boundary conditions imposed on the velocity and temperature fields. The nonlinear stages of

Rayleigh Taylor instabilities and droplets rising in a stagnant fluid are characterized. The developed model shows and more stable more accurate results. The thermal model was employed to study the Rayleigh-Benard convection in a square and rectangular cavity. It has been demonstrated here that the lattice Boltzmann method can be an effective computational fluid dynamics tool to tackle complex flows.

CHAPTER 1: MOTIVATION AND OBJECTIVES

1.1. Motivation and Objectives

The Lattice Boltzmann method is a tool from statistical mechanics that predicts macroscopic properties of fluids such as viscosity, thermal conductivity, and diffusion coefficient from the microscopic properties of atoms and molecules. The method has been investigated by several investigators and has been increasing in popularity since its development in the early nineties. LBM has been shown to have accuracy comparable to traditional CFD methods. Since its initial application using a single relaxation time, the method has been modified in a number of ways to improve its stability. Two well-known modifications are the Multi-Relaxation Time method (MRTLBM) and the Regularized method (RLBM). MRTLBM gained some traction especially with higher Reynolds number flows. In multi-phase applications, such as the Rayleigh-Taylor Instability, single relaxation time LBM can easily become unstable at larger density difference between the phases. MRTLBM improves the stability of the multiphase LBM model and it is enough to study this problem with Atwood number of 0.1. The Regularized LBM is proven to improve the stability for high speed flows.

The main objective here is to develop a stable lattice Boltzmann method to solve two and three dimensional complex flows problems. The Regularized Multi-Relaxation time was introduced and shown to be a stable technique to simulate turbulent flows. The method is simple in implementation and provides very stable and accurate solutions compared to the direct numerical simulation and large eddy simulation. The method is tested upon complex interfacial flows and turbulent flows past obstacles and is proven to provide an accurate solutions. Computational time required by the present model is order of magnitude less

than that of high resolution large eddy simulations and direct numerical solution for the same level of accuracy attained.

1.2. Background

The Lattice Boltzmann method (LBM) is derived from the kinetic theory. It can be used to predict the physical properties of substances from the microscopic properties of atoms and molecules. The method has been investigated by several investigators and has been increasing in popularity since its development in the early nineties. Chen and Doolen [1] account the history of the Lattice Boltzmann Method (LBM) and its evolution from the old Lattice Gas Automata method. They go on to discuss some of the classical flows studied with LBM such as: multiphase flows, suspended particles, and heat transfer problems. Historically, the lattice Boltzmann method originated from the lattice-gas cellular automata method (LGCA)[2]. The BGK which is known as the lattice Bhatnagar-Gross-Krook method has been developed rapidly and applied for many studies. The nonlinear term in the lattice Boltzmann approximated by BGK to be linear term, and this term is known as the collision term in the lattice BGK governing equation. The main idea of LBM is to bridge the gap between micro scale and macro scale by not considering individual behavior of particles alone but behavior of a collection of particles as a unit. The property of particle is represented by a distribution function. The distribution function acts as a representative for collection of particles. This scale is known as mesoscopic scale. The terminology of the kinetic theory is the essence of the lattice Boltzmann equation. In 1970 Pomeau and de Groot started working on LBM or the Lattice Gas Automata Method or HPP method [3]. They modeled the movements of particles and studied each particle movement and their initial speed and direction. The particles follow two steps: first collision steps, then

streaming or transport steps. During the collision step every node is searched for a collision, where a collision is defined as either two particles sharing a node or a particle on a boundary node. Whenever a collision is found and the velocities are updated. The velocity of each particle at each node is updated and then calculated the next neighbor's nodes. All of these processes can be done either by collision or streaming steps. The modern Lattice Boltzmann method removes the discrete particles from the model. In their place, there is the density distribution function.

The governing equation of the Lattice Boltzmann (LBE) is called the evolution equation of the distribution function of the particles. The density distribution function updates at every time step. Then, from the density distribution function the velocities are evaluated. In most mathematical models, the evolution equation is updated in two steps. In the spirit of the old Lattice Gas Automata method, the two steps are called the collision step and the streaming step. The first step, which updates the density distribution function at every node with a relaxation time and an equilibrium density distribution function, is the collision step. Following that, the density distribution function moves outward in a transport step called the streaming step. Early research in LBM compared the solutions of flow problems obtained by LBM to solutions obtained by other methods, such as: Spectral Methods [4,5]. In 1990, Benzi realized that LBM can be employed for Multi-phase flows. The basic reason that LBM can be so easily applied to problems with multiple fluids; is because there is no need to track fronts or interfaces (capturing of the interface can be traced using LBM naturally). This is due to the way that LBM model multiple fluids [6]. The coloring method of the multiple fluids is utilized to show each fluid location at every time step. The Rotman model was developed even before LBM on the Lattice Gas Automat (LGA) method [7].

Some researchers adapted the coloring method to LBM, however the method still retains several problems with the exaggerated effects of numerical noise that could be seen in (LGA). Shan and Chen model was developed which known as a more practical method. The idea in this model is to add the effects of the other fluids “external sources” which is called interactive or interparticle force between the fluids which can be added directly either in the evolution equation or in the equilibrium equation [8]. Recently, free energy method was introduced by Swift (1995). His idea is to re-derive the equation for the equilibrium density function using a free energy function. Therefore, the equilibrium can be made to include a variety of effects include the effects of multiple fluids [9]. He et al. showed that Shan and Chen model and free energy model can be derived from the Boltzmann evolution equation for the kinetic theory [10]. They apply various simplifications and approximations on the same governing equation. Therefore, each produces the same solutions with various levels of accuracy. He et al. [11] also produced their own method for dealing with multiphase problems, called the He’s method. He also derives a new equilibrium density distribution function. He’s method relies on a second equilibrium function for pressure. It is easier to model multiple fluids with Shan and Chen’s model, which can be employed to a variety of problems.

LBM has been shown to be comparable to traditional CFD methods [12]. Since its initial application using a single relaxation time, the method has been modified in a number of ways to improve its stability. Two well-known modifications are the Multi-Relaxation Time method (MRTLBM) and the Regularized method (RLBM). MRTLBM gained some traction especially with higher Reynolds number flows.

The present investigators [13] have studied Rayleigh-Taylor instabilities and droplet problems using MRTLBM. In multi-phase applications, such as the Rayleigh-Taylor instability, single relaxation time LBM can easily become unstable at low viscosities. MRTLBM improves the stability of this method enough to investigate these flows effectively. McCracken and Abraham [14] also work around this stability problem when studying two-phase oscillating liquid cylinders problem using the MRTLBM. There are far fewer examples of the Regularized method being used. Izham et al. [15] demonstrates the Regularized lattice Boltzmann method (RLBM) on a high Reynolds number lid driven cavity flow. The RLBM was implemented to improve the stability. The density of the distribution function on the collision term of the evolution governing equation is broken into its equilibrium and non-equilibrium distribution functions. The non-equilibrium distribution functions substituted into the non-equilibrium stress tensor.

In the present investigation the new lattice Boltzmann method is introduced to study high speed turbulent flows. The method introduced here is the combined multi-relaxation time and regularized lattice Boltzmann method. Such method improves the stability of the LBM and helps LBM to be applicable to study highly turbulent flows. This newly introduced unique method has been applied to study turbulent flows past a square cylinder. The turbulent flow structures in this geometry has been identified at the resolution of LES or even Direct Numerical simulations level. The present results were compared to those obtained by large eddy simulation and experimental studies. The present investigators also considered the flow past an array of square cylinders, both inline and staggered arrangements [16].

Classical methods for modeling turbulent flows include LES and Direct Numerical Simulations (DNS). Both methods are resource hogs with unacceptably long runtimes. The method used in the present study runs in a fraction of the time required by LES or DNS.

A wide range of complex flows are covered in the present study. These flows include turbulent flows and interfacial flows. The main goal of this research is to develop stable lattice Boltzmann method to study two and three dimensional turbulent and interfacial flows. Stability enhancement of lattice Boltzmann method has been demonstrated in turbulent flows pass a cylinder confined in a channel and the interfacial flows induced by Rayleigh Taylor instabilities.

CHAPTER 2: MATHEMATICAL MODELS

2.1. BGK Approximation -Single Relaxation Time (SRT)

The Lattice Boltzmann Method (LBM) was developed from the Lattice Gas Automaton method (LGA) studied by Martin et al. [17] and by Wolf-Gladrow [18]. In LGA imaginary particles are placed on the lattice and are given velocities. At each time step the particles will move along the lattice to their next position based on their velocities, this is the streaming or propagation step. Then, if multiple particles are on the same node in the lattice, certain collision rules are followed. This is called the collision step. By the collision step the velocities are updated for the next time step. This easily conserves mass and momentum. Mass is conserved by maintaining the same number of imaginary particles throughout the simulation and momentum is conserved by the rules set in the collision step. However, there are serious problems with noise due to the bulk treatment of the particles and the viscosity is hard to control due to how collisions are treated. LBM uses Boltzmann's density distribution function to create a continuous model for the particles which introduces a relaxation term. Due to this relaxation term and the fact that LBM uses a continuous distribution function, the problems with noise are smoothed out and the viscosity becomes easy to set.

Before we continue into the discussion of LBM there are a few issues that should be addressed. The lattice variables, while typically retaining the same or similar notation as their real counterparts are not the same. For example lattice viscosity is actually determined by

$$\nu_{lattice} = \frac{\delta x^2}{3\delta t}(\tau - 0.5)$$

1

As outlined by Succi [2], the general rule is to obtain the lattice parameters using the discretization parameters $\delta x = 1$ and $\delta_t = 1$. In effect this means that δx is the spacing between two adjacent lattice nodes, δ_t is the time of a single time step and τ is the relaxation time.

A description of the lattice structure is also necessary for the method. It is common to refer to the lattice being studied as DnQl, where n and l are numbers. In this shorthand, the n is the number of spatial dimensions and the l is the number of lattice directions at each node. The present study was done using D2Q9, which is depicted in Figure 1.

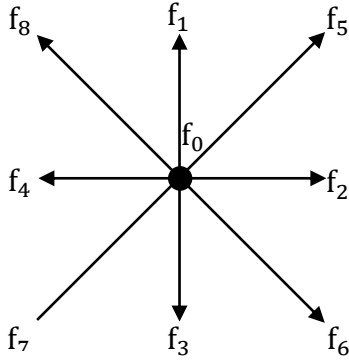


Figure 1. D2Q9 arrangement for lattice inside the flow domain.

The Boltzmann relation which all of LBM research is based on is

$$\frac{\partial f}{\partial t} + \mathbf{v} \cdot \nabla f + \frac{\mathbf{F}}{m_p} \frac{\partial f}{\partial \mathbf{v}} = \Omega(f)_{\text{collision}} \quad 2$$

In equation (2) \mathbf{v} is the particle velocity, \mathbf{F} is the term of external forces, and m_p is the particle mass. Note that the third term will be dropped as the present investigation contains no external forces. f is the density distribution function, which is to say, for some position and some time, the number of particles per volume with a velocity between \mathbf{v} and $\mathbf{v} + d\mathbf{v}$.

This form of the equation is, unfortunately, unusable since the time rate of change of "f" due to collisions on the right hand side is not easy to be determined. In the 1950s Bhatnagar et al. [19] introduced the approximation:

$$\Omega(f)_{\text{collision}} = \frac{\delta_t}{\tau} (f^{\text{eq}} - f) \quad 3$$

Here τ is the lattice relaxation time; which is, in the single relaxation time method described below, determined by the viscosity and the lattice parameters, as displaced in equation(1). The Boltzmann equation with this relation, sometimes called the BGK model, is what most LBM research is based on. The original research into the modern LBM was done on the single relaxation time method. Martinez [20] verifies the results of the method by comparing his results for a shear flow with results obtained by a spectral method. Hazi and Jimenez [21] verify a modified version of this equation for 2-D decaying turbulence in a square box against pseudo-spectral methods. Single relaxation time LBM is still popular in research since it is simple and easy to be implemented. In single relaxation time LBM the propagation and collision steps are represented in the evolution equation.

$$f_k(\mathbf{r} + \mathbf{e}_k \delta_t, t + \delta_t) - f_k(\mathbf{r}, t) = -\frac{\delta_t}{\tau} [f_k(\mathbf{r}, t) - f_k^{\text{eq}}(\mathbf{r}, t)] \quad 4$$

In equation (4) above, the left hand side represents streaming and the right hand side represents the collision. Here the function $f_k(\mathbf{r}, t)$ is the density distribution function along the lattice branch k , \mathbf{r} is the spatial coordinate, and t is time. \mathbf{e}_k is the expression for the discrete velocities along each lattice branch k , $f_k^{\text{eq}}(\mathbf{r}, t)$ is the equilibrium distribution function. f_k^{eq} is a very important term, since the appropriate selection of this function guarantees that the evolution equation satisfies the Navier Stokes equation. To select f_k^{eq}

a Chapman-Enskog expansion is applied. As Chapman and Cowling [22], the equilibrium distribution function is

$$f_k^{\text{eq}} = C \left\{ 1 + C_1 \mathbf{e}_k \cdot \mathbf{u} + C_2 \left[(\mathbf{e}_k \cdot \mathbf{u})^2 - \frac{1}{2} |\mathbf{u}|^2 \right] + \dots \right\} \quad 5$$

where \mathbf{u} is the fluid velocity. The higher order terms are unnecessary for an incompressible fluid; therefore only three constants (C , C_1 , C_2) need to be selected. To select these constants these three constraints from kinetic theory are applied

$$\sum_k f_k^{[0]} = \rho \quad 6$$

$$\sum_k f_k^{[0]} \mathbf{e}_k = \rho_0 \mathbf{u} \quad 7$$

Equation (6) and (7) are necessary to satisfy the conservation laws. Here ρ_0 is the density of the fluid and ρ is the local density. While the fluid in question is incompressible ρ is capable of small variation in ρ since in this method ρ defines pressure as described below. After applying constraints (equations (6) and (7)) to the Chapman-Enskog expansion (equation 5), yields:

$$f_k^{\text{eq}}(\mathbf{r}, \mathbf{t}) = w_k \left\{ \rho_k + \rho_0 \left(3 \frac{\mathbf{e}_k \cdot \mathbf{u}}{e^2} + \frac{9 (\mathbf{e}_k \cdot \mathbf{u})^2}{2 e^4} - \frac{3 |\mathbf{u}|^2}{2 e^2} \right) \right\} \quad 8$$

where \mathbf{e} is the lattice speed defined as

$$\mathbf{e} = \frac{\delta_x}{\delta_t} \quad 9$$

and w_k is the weighting function specific to the lattice geometry.

The full proof that the evolution equation satisfies the Navier Stokes equation can be found in He and Lou [23]; however for the sake of understanding the RLBM discussed below a

brief overview must be provided. The first step is to express the equation (10) terms in 2-D Taylor series expansion

$$f_k(\mathbf{r} + \mathbf{e}_k \delta_t, t + \delta_t) = \sum_{n=0}^{\infty} \frac{\epsilon^n}{n!} D_t^n f_k(\mathbf{r}, t) \quad 10$$

where $\epsilon = \delta_t$ is a small parameter and D_t is the operator $(\partial_t + \mathbf{e}_k \cdot \nabla)$. Then from perturbation analysis the function f_k can be expressed as in equation (11)

$$\sum_{n=0}^{\infty} \epsilon^n f_k^{[n]} \quad 11$$

and the operator ∂_t as in equation(12)

$$\sum_{n=0}^{\infty} \epsilon^n \partial_{t_n} \quad 12$$

Then substitute these definitions into the evolution equation and extract the terms of order ϵ zero, one and two. By applying the constraint equations above and with the definition of dimensionless pressure as

$$P = \frac{c_s^2 \rho}{\rho_0} \quad 13$$

The first order ϵ equation can be shown to be the Euler equation and the second order ϵ equation can be shown to be the full Navier Stokes equation.

2.1. Multi-Relaxation Time -MRTLBM

Single relaxation time LBM has a great deal of stability issues and will begin to fail even at fairly low Reynolds numbers. To solve these stability issues past investigators (d'Humieres [24]) developed the Multi-Relaxation Time Lattice Boltzmann Method (MRTLBM). At the start of the present study MRTLBM was employed to deal with the

high Reynolds numbers in the problem. In MRTLBM the evolution equation becomes the system of equations:

$$\mathbf{f}(\mathbf{r} + \mathbf{e}_k \delta_t, t + \delta_t) - \mathbf{f}(\mathbf{r}, t) = S[\mathbf{f}(\mathbf{r}, t) - \mathbf{f}^{\text{eq}}(\mathbf{r}, t)] \quad 14$$

where the bold face is used to denote a vector of k elements and S is a matrix called the collision matrix. Notice that when the collision matrix is defined as

$$S = \frac{\delta_t}{\tau} \mathbf{I} \quad 15$$

where \mathbf{I} is the identity matrix, the equation reduces to the single relaxation time LBM evolution equation. In MRTLBM the idea is to go from the velocity space where \mathbf{f} exists to a moment space where the function \mathbf{m} exists. Note that the vector \mathbf{m} is made up of elements m_B where the set B has the same cardinality as the set of k . Each moment m_B can be found using the relation

$$m_B = \phi_B \cdot \mathbf{f} \quad 16$$

This definition clearly shows that the moments are linear combinations of \mathbf{f} . From this, basic linear theory tells us that the velocity space and the moment space must have a linear mapping

$$\mathbf{m} = \mathbf{M} \cdot \mathbf{f} \quad 17$$

Now choose the collision matrix in such a way that its eigenvectors are ϕ_B the collision process will be naturally accomplished. Applying these relations to equation (14) will result in the MRTLBM evolution equation.

$$f_k(\mathbf{r} + \mathbf{e}_k \delta_t, t + \delta_t) - f_k(\mathbf{r}, t) = -M^{-1} \hat{S}[m_k(\mathbf{r}, t) - m_k^{\text{eq}}(\mathbf{r}, t)] \quad 18$$

where \hat{S} is a diagonalized new collision matrix such that

$$\hat{S} = M \cdot S \cdot M^{-1} \quad 19$$

For a more detailed derivation, please refer to d'Humieres and his colleagues [24, 25]. The Multi-relaxation time has been applied to study the complex flow in the lid driven up to $Re=20000$ [26].

2.3. Regularized –Lattice Boltzmann -RLBM

With MRTLBM alone present investigators were able to bring the flow past a cylinder to around Reynolds number of 10000 for the lattice resolution selected. Past this, the method again begins to see stability problems. A number of years ago another method was developed from single relaxation time LBM; this method, called Regularized Lattice Boltzmann Method (RLBM), was an attempt to improve the stability of single relaxation time LBM by using a non-equilibrium distribution function. However as MRTLBM grew more popular the method got less attention. In the classical RLBM, a non-equilibrium distribution function is introduced such that

$$f_k^{neq}(\mathbf{r}, t) = f_k(\mathbf{r}, t) - f_k^{eq}(\mathbf{r}, t) \quad 20$$

Similarly, a non-equilibrium stress tensor is found as

$$\Pi_{kij}^{neq} = \Pi_{kij} - \Pi_{kij}^{eq} \quad 21$$

Now introduce this definition for the relationship between the stress tensor and the distribution function as

$$\Pi_{kij} = \sum_{\mathbf{k}=0}^8 \mathbf{e}_{ki} \mathbf{e}_{kj} f_{\mathbf{k}} \quad 22$$

Notice that this is simply the velocity moment of the distribution function. Combining these two equations gets the following relation for the non-equilibrium part of the stress tensor

$$\Pi_{kij}^{neq} = \Pi_{kij} - \sum_{k=0}^8 \mathbf{e}_{ki} \mathbf{e}_{kj} f_k^{eq} \quad 23$$

Now in the interest of canceling higher order contributions to our governing equation as described in Latt and Chopard [27] the following expression is found using the Chapman-Enskog expansion.

$$f_k^{neq}(\mathbf{r}, t) \approx f_k^{(1)} = \frac{w_k}{2c_s^4} \mathbf{Q}_{kij} \Pi_{ij}^{neq} \quad 24$$

where the tensor \mathbf{Q}_{kij} is defined as

$$\mathbf{Q}_{kij} = \mathbf{e}_{ki} \mathbf{e}_{kj} - c_s^2 \delta_{ij} \quad 25$$

where δ_{ij} is the Kronecker delta function. Using this equation the modified evolution equation of the form is obtained

$$f_k(\mathbf{r} + \mathbf{e}_k \Delta t, t + \Delta t) - f_k(\mathbf{r}, t) = -\frac{\omega_k}{2\tau c_s^4} \mathbf{Q}_{kij} \Pi_{ij}^{neq} \quad 26$$

2.4. Regularized Multi-Relaxation Time -RMRTLBM

In the present investigation it was attempted to further increase the stability so as to simulate the turbulent flow past a square cylinder at much higher Reynolds numbers than what had been previously studied [16]. To do this the two methods mentioned above are combined. The same procedure as the regularized method was followed except that this was introduced.

$$f_k^{\text{neq}}(\mathbf{r}, t) = f_k(\mathbf{r}, t) - f_k^{\text{eq}}(\mathbf{r}, t) \quad 27$$

Continuing along the same reasoning as in regularized LBM the following relation is reached.

$$m^{\text{neq}} = Mf^{\text{neq}}(\mathbf{r}, t) = M \left[\frac{\omega_k}{2c_s^4} \mathbf{Q}_{kij} \Pi_{ij}^{\text{neq}} \right] \quad 28$$

$$m = Mf \quad 29$$

Substitution into the equation (14) yields to R-MRTLBM

$$f_k(\mathbf{r} + \mathbf{e}_k \Delta t, t + \Delta t) - f_k(\mathbf{r}, t) = -M^{-1} \hat{S} M [f_k(\mathbf{r}, t) - f_k^{\text{eq}}(\mathbf{r}, t)] \quad 30$$

Using this governing equation, turbulent flow past a bluff body for Reynolds numbers above 20000 can be achieved. Numerical values of components of M , m_k^{eq} , \hat{S} , w_k , and \mathbf{e}_k are given in as

$$M = \begin{bmatrix} 1 & 1 & 1 & 1 & 1 & 1 & 1 & 1 & 1 \\ -4 & -1 & -1 & -1 & -1 & -2 & 2 & 2 & 2 \\ 4 & -2 & -2 & -2 & -2 & -1 & 1 & 1 & 1 \\ 0 & 1 & 0 & -1 & 0 & 1 & -1 & -1 & 1 \\ 0 & -2 & 0 & 2 & 0 & 1 & -1 & -1 & 1 \\ 0 & 0 & 1 & 0 & -1 & 1 & 1 & -1 & -1 \\ 0 & 0 & -2 & 0 & 2 & 1 & 1 & -1 & -1 \\ 0 & 1 & -1 & 1 & -1 & 0 & 0 & 0 & 0 \\ 0 & 0 & 0 & 0 & 0 & 1 & -1 & 1 & -1 \end{bmatrix} \text{ and } m^{\text{eq}} = \begin{bmatrix} \rho \\ -2\rho + 3(J_x^2 + J_y^2) \\ \rho - 3(J_x^2 - J_y^2) \\ J_x \\ -J_x \\ J_y \\ -J_y \\ (J_x^2 - J_y^2) \\ J_x J_y \end{bmatrix} \quad 31$$

Here J_x and J_y are linear momentum in x and y directions. Components of the diagonal matrix \hat{S} are 1, 1.4, 1.4, 1, 1.2, 1, 1.2, τ and τ . The weighting function for $k = 1$ to 9 is

$$w_k = \frac{1}{9} \{4, 1, 1, 1, 1, \frac{1}{4}, \frac{1}{4}, \frac{1}{4}, \frac{1}{4}\} \quad 32$$

and the discrete lattice velocity is

$$\mathbf{e}_k = \{(0,0), (1,0), (0,1), (-1,0), (0,-1), (1,1), (-1,1), (-1,-1), (1,-1)\} \quad 33$$

2.5. Multi-phase Flow Model

To deal with multiple fluids simply introduce multiple density distribution functions: f_k^σ , with $\sigma = \{1 \dots \alpha\}$ where α is the number of fluids in the system. Now the evolution equation becomes the system of equations:

$$\frac{\partial f_k^\sigma}{\partial t} + \mathbf{e}_k \cdot \nabla f_k^\sigma = \omega(f_k^{\sigma \text{ eq}} - f_k^\sigma) + \frac{W_k c_k \mathbf{F}^\sigma}{c_s^4} \quad 34$$

As it is, this evolution equation is missing a key component to multiphase flows, inter-particle forces, \mathbf{F}_{int} . To add this effect into the multiphase flow we used the model introduced by Shan and Chen is used [28]. Also we need a common velocity and a density which can be found by what is effectively mass averaging are needed

$$\rho^\sigma = \sum_{k=0}^q \mathbf{f}_k^\sigma, \quad \mathbf{u}^\sigma = \frac{\sum_{\sigma} \frac{1}{\tau_\sigma} \sum_k f_k^\sigma \mathbf{e}_k}{\sum_{\sigma} \frac{1}{\tau_\sigma} \rho_\sigma} \quad 35$$

With this we can solve for an equilibrium velocity can be determined. Using this velocity in the calculations for $f_k^{\sigma \text{ eq}}$ will automatically account for the inter-particle forces as demonstrated in Shan and Chen. The total external forces can be treated by different ways. The force term can be added as an external term to the right hand side of the governing evolution equation (34) as, $\rho \mathbf{F}^\sigma$ and the other way is to add the force term to the LBE, by modifying velocity in calculating equilibrium distribution functions. Newton's second law of motion states that,

$$\mathbf{F} = m \mathbf{a} = m \frac{d\mathbf{u}}{dt} \quad 36$$

where \mathbf{a} and \mathbf{u} are acceleration and velocity vectors, respectively, then

$$\Delta \mathbf{u} = \frac{\tau^\sigma \mathbf{F}^\sigma}{\rho^\sigma} \quad 37$$

where τ^σ is the relaxation time of σ components

The velocity should be modified by $\Delta \mathbf{u}$ in calculating equilibrium distribution functions only,

$$\mathbf{u}^{\sigma eq} = \mathbf{u}^\sigma + \Delta \mathbf{u} \quad 38$$

The external force represents body force, interfacial force, adhesive force, or any other external forces.

$$\mathbf{F}^\sigma = \mathbf{F}^{\sigma_{int}} + \mathbf{F}^{\sigma_{body}} + \mathbf{F}^{\sigma_{adh}} \quad 39$$

Here \mathbf{F}^σ is the total inter-particle force on fluid σ per unit volume. It has been shown by Huang et al [29] that \mathbf{F}^σ can be extended to include other forces such as body forces and adhesion forces. In the present investigation adhesion forces were ignored; however, a body force was included. This was necessary since, by definition, the Rayleigh Taylor instability requires a body force in the opposite direction to a density gradient. Therefore, in the present investigation the inter-particle force is calculated using [30]

$$\mathbf{F}^\sigma = \mathbf{F}_{int}^\sigma + \mathbf{F}_{body}^\sigma \quad 40$$

$$\mathbf{F}_{int}^\sigma(\mathbf{r}, t) = -G \overline{\psi^\sigma}(\mathbf{r}, t) \sum_a w_a \psi^\sigma(\mathbf{r} + \Delta \mathbf{r}) \quad 41$$

The potential strength is determined by using Shan and Chen model [28] as

$$\psi^\sigma(\mathbf{r}, t) = \rho_0^\sigma (1 - e^{-\rho^\sigma / \rho_0^\sigma}) \quad 42$$

Since only the interactions between point and its x neighbours are being considered G can be written as:

$$G(\mathbf{r}, \mathbf{r}') = \begin{cases} 0, & |\mathbf{r} - \mathbf{r}'| > c \\ \phi^{ii}, & |\mathbf{r} - \mathbf{r}'| \leq c \end{cases} \quad 43$$

where ϕ^{ii} is a constant parameter which controls the strength of the inter-particle forces.

The gravity force is much simpler:

$$\mathbf{F}_{\text{body}}^\sigma = \mathbf{g}_r \rho^\sigma \quad 44$$

For the sake of presentation a colouring step can be added to this method in the two fluid cases. The idea is to create a function κ which is one at a node entirely dominated by the lighter fluid, negative one at a node entirely dominated by the heavier fluid, and somewhere between one and negative one for a node which consists of both the light and heavy fluid.

$$\kappa = \frac{\rho^{\text{light}} - \rho^{\text{heavy}}}{\rho^{\text{light}} + \rho^{\text{heavy}}} \quad 45$$

At any given instant this colouring function can be contour plotted to produce an image showing where each fluid is.

2.6. Lattices Boltzmann Arrangements

The common terminology of LBM arrangement is $DnQl$ which refers to the dimension of the domain and the number of distribution functions, where n denotes to the dimension of the domain and l denotes the directional velocity.

2.6.1 One Dimensional LBM Arrangements

This terminology can be employed for one-dimensional flow. It can be written as D1Q2. The lattice arrangement for D1Q2 is shown in Table 1.1. It means that one dimensional problem with two linkages or distribution functions. It can be applied for flow or heat transfer problem.

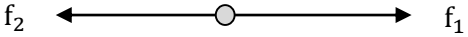
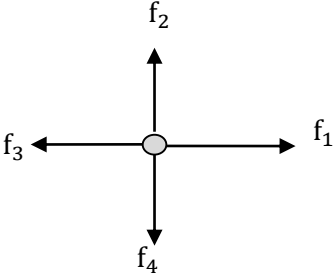
Lattice Arrangements type	Linkages / or distribution functions
D1Q2 (One dimension and two distribution functions)	

Table 1.1. One dimensional lattice arrangements.

2.6.2 Two Dimensional LBM Arrangements

There are various two dimensional lattice arrangements. As an example D2Q4, D2Q5 and D2Q9 are illustrated in Table 1.2.

Lattice Arrangements type	Linkages / or distribution functions
D2Q4 (Two dimensions and four distribution functions)	

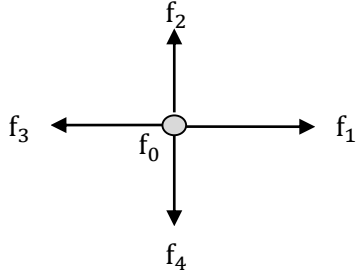
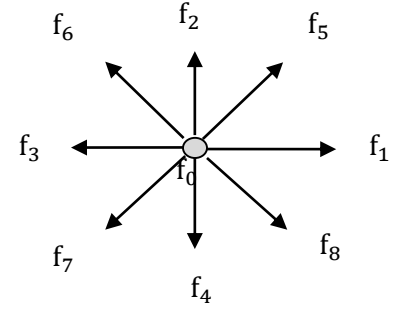
<p>D2Q5</p> <p>(Two dimensions and five distribution functions)</p>	
<p>D2Q9</p> <p>(Two dimensions and nine distribution functions)</p>	

Table 1.2. Two dimensional lattice arrangements.

2.6.3 Three Dimensional LBM Arrangements

Three dimensional lattices Boltzmann arrangements, D3Q15, D3Q19, have been employed to study three-dimensional lid-driven study [31]. It is shown that as the number of distribution functions increases, the accuracy of the simulations improves. The accuracy of the results also depends on how the boundary conditions are treated. Here in this chapter various boundaries are applied such as periodic, 2nd order accuracy boundary, and Neumann boundary.

Lattice Arrangements type	Linkages / or distribution functions
<p>D3Q15</p> <p>(Three dimensions and fifteen distribution functions)</p>	
<p>D3Q19</p> <p>(Three dimension and nineteen distribution functions)</p>	

Table 1.3. Three dimensional lattice arrangements.

2.7. Equilibrium Distribution Function

The equilibrium distribution function is the key element in implementing LBM. The different physical problem can be solved by using LBM provided that a proper equilibrium distribution function is utilized.

The normalized Maxwell's distribution function can be written as,

$$f_k = \frac{3\rho}{2\pi} e^{\frac{-3e_k^2(\mathbf{u}^2 - \mathbf{e}_k \cdot \mathbf{u})}{2}} \quad 46$$

which can be re-written as,

$$f_k = \frac{3\rho}{2\pi} e^{-\frac{3e^2}{2}} e^{\frac{3(\mathbf{e} \cdot \mathbf{u} - \mathbf{u}^2)}{2}} \quad 47$$

where $e^2 = \mathbf{e} \cdot \mathbf{e}$ and $\mathbf{u}^2 = \mathbf{u} \cdot \mathbf{u}$. Using the Taylor series expansion of exponential (e^{-x}) equation (47) can be written as

$$f_k = \frac{3\rho}{2\pi} e^{-\frac{3c^2}{2}} \left(1 + 3(\mathbf{e}_k \cdot \mathbf{u}) - \frac{3}{2} \mathbf{u}^2 + \dots \right) \quad 48$$

The general form of the equilibrium function can be written as

$$f_k^{\text{eq}} = w_k \varnothing(X, t) \left(1 + 3(\mathbf{e}_k \cdot \mathbf{u}) - \frac{3}{2} \mathbf{u}^2 + \dots \right) \quad 49$$

where \varnothing represents a temperature, a species or a density, w_k is the weighting function, \mathbf{e}_k is lattice velocity vector

$$\mathbf{e}_k = \frac{\delta_x}{\delta_t} \mathbf{i} + \frac{\delta_y}{\delta_t} \mathbf{j} + \frac{\delta_z}{\delta_t} \mathbf{k} \quad 50$$

The velocity field in two-dimensional problems can be defined as

$$\mathbf{u} = u\mathbf{i} + v\mathbf{j} \quad 51$$

The velocity field in three-dimensional problems can be defined as

$$\mathbf{u} = u\mathbf{i} + v\mathbf{j} + w\mathbf{k} \quad 52$$

where \mathbf{i}, \mathbf{j} , and \mathbf{k} are unit vectors in x, y, and z directions.

2.8. Lattice Boltzmann Domain and Physical Domain

The conversion from lattice domain to physical domain is the important issue to present results with the physical dimensions [32]. The conversion is an easy process. The dimensionless parameters that make linking between lattice and physical domain such as Reynolds number, Prandtl number, and Rayleigh number have to be selected. In this section detailed description of such conversion is provided.

$$\text{Re}_D = \left(\frac{UD}{\nu} \right)_{\text{physical}} = \text{Re}_N = \left(\frac{U_{lb}N}{\nu_{lb}} \right)_{\text{lattice}} \quad 53$$

where U is the actual velocity in [m/s], D is the characteristic dimension in [m], U_{lb} is the velocity per lattice, ν is the actual kinematic viscosity in [m²/s], ν_{lb} is the kinematic viscosity per lattice, Re_D is the Reynolds number based on the physical parameters, and Re_N is the Reynolds number based on the lattice parameters.

The actual (physical) time can be evaluated by

$$T_{\text{phy}} = \left(\frac{D}{U} \right)_{\text{phy}} \quad 54$$

and the lattice time can be calculated by

$$T_{lb} = \left(\frac{N}{U_{lb}} \right)_{lb} \quad 55$$

Since the $\text{Re}_D = \text{Re}_N$ the time can be presented in terms of the kinematic viscosity of the fluid physical and the lattice domain as follow

$$\left(\frac{D^2}{\nu} \right)_{\text{phy}} = \left(\frac{N^2}{\nu_{lb}} \right)_{lb} \quad 56$$

From equation (56) the kinematic viscosity per unit lattice (lu²/ts) can be determined

$$\nu_{lb} = \frac{(U_{lb}N)_{lb}}{(U \times D)_{\text{phy}}} \nu_{\text{phy}} \quad 57$$

Therefore, the actual time step in LBM is expressed as

$$ts = \frac{D^2 v_{lb}}{N^2 v_{phy}} \quad 58$$

In the case when the Rayleigh number characterizes the flow

$$Ra = \frac{g\beta\Delta TH^3}{\nu\alpha} = \frac{g\Delta\rho H^3}{\nu^2\rho} \quad 59$$

The kinematic viscosity per unit lattice can be defined in terms of physical domain properties (ρ , ν , and g) as

$$v_{lb} = \sqrt{\frac{\rho\nu^2}{gL^3\Delta\rho} \frac{\Delta x^2}{\Delta t}} \quad 60$$

For natural convection, selecting the product of the acceleration and the thermal expansion should be selected for the conversion process

$$g\beta = \frac{Ra \times \nu \times \alpha}{\Delta\theta N^3} \quad 61$$

where N is the numbers of lattices in the characteristic length, α , ν are kinematic viscosity (m^2/sec) and thermal diffusivity (m^2/sec), respectively, and $\Delta\theta$ is the normalized temperature difference between the hot side and the reference temperature. The normalized temperature is defined as

$$\theta = \frac{T - T_c}{T_h - T_c}, \text{ thus } \theta_h = 1 \text{ and } \theta_c = 0, \text{ and } \theta_{ref} = \frac{(\theta_h + \theta_c)}{2}, \Delta\theta = \theta_h - \theta_{ref} \quad 62$$

2.9. Calculation of Stream Functions and Vorticity

The vorticity field is determined from the definition

$$\omega = \frac{\partial V}{\partial X} - \frac{\partial U}{\partial Y} \quad 63$$

The equation (63) is discretized by using the central scheme

$$\omega(i, j) = \frac{V(i + 1, j) - V(i - 1, j)}{2\Delta X} - \frac{U(i, j + 1) - U(i, j - 1)}{2\Delta Y} \quad 64$$

The stream functions can be evaluated from the vorticity Poisson equation

$$\omega = -\left(\frac{\partial^2 \psi}{\partial X^2} + \frac{\partial^2 \psi}{\partial Y^2}\right) \quad 65$$

Discretizing equation (64) by using the central scheme for the interior nodes yield

$$2 \leq i \leq N_x - 1, \quad 2 \leq j \leq N_y - 1$$

$$\psi(i, j) = \frac{1}{\frac{2}{\Delta X^2} + \frac{2}{\Delta Y^2}} \left(\frac{[\psi(i + 1, j) + \psi(i - 1, j)]}{\Delta X^2} + \frac{[\psi(i, j + 1) + \psi(i, j - 1)]}{\Delta Y^2} + \omega(i, j) \right) \quad 66$$

The discretized equations for the boundary node is listed in Table 1.4 for various type of boundary conditions.

Type of scheme	No-slip BCs	Periodic BCs
Forward scheme	Vorticity:	Vorticity:
	$\omega = -\frac{\partial U}{\partial Y}$ (Lower)	$\omega = \frac{\partial V}{\partial X} - \frac{\partial U}{\partial Y}$ (Lower)
	$\omega = \frac{\partial V}{\partial X}$ (Left)	$\omega = \frac{\partial V}{\partial X} - \frac{\partial U}{\partial Y}$ (Left)
	Stream Function:	Stream Function:
$\psi(i, 1) = 0$	$-\omega = \frac{\partial^2 \psi}{\partial X^2} + \frac{\partial^2 \psi}{\partial Y^2}$ (Lower)	
$\psi(1, j) = 0$		$-\omega = \frac{\partial^2 \psi}{\partial X^2} + \frac{\partial^2 \psi}{\partial Y^2}$ (Left)

Backward scheme	Vorticity:	Vorticity:
	$\omega = -\frac{\partial U}{\partial Y}$ (Lower)	$\omega = \frac{\partial V}{\partial X} - \frac{\partial U}{\partial Y}$
	$\omega = \frac{\partial V}{\partial X}$ (Right)	$\omega = \frac{\partial V}{\partial X} - \frac{\partial U}{\partial Y}$ (Lower)
	Stream Function:	Stream Function:
$\psi(i, N_y) = 0$	$\omega = \frac{\partial V}{\partial X} - \frac{\partial U}{\partial Y}$ (Right)	
$\psi(N_x, j) = 0$		$-\omega = \frac{\partial^2 \psi}{\partial X^2} + \frac{\partial^2 \psi}{\partial Y^2}$ (Upper)
		$-\omega = \frac{\partial^2 \psi}{\partial X^2} + \frac{\partial^2 \psi}{\partial Y^2}$ (Right)

Table 1.4. Vorticity and stream function discretization at the boundary. No-slip and periodic boundary conditions are applied.

2.10. Types of Boundary Conditions in the Lattice Boltzmann Method

There are several models for treating boundary conditions in lattice Boltzmann method. This section describes these boundary conditions: a reflection boundary condition, a periodic boundary condition, and a mass conserving boundary condition similar to the one studied by Zou and He [33] and Kuo and Chen [34].

2.10.1. Reflection Boundary Conditions

The non-equilibrium bounce back condition states that the part of the density distribution function not contributing to the equilibrium will be reflected from the boundary. Therefore:

$$f_a - f_a^{eq} = f_b - f_b^{eq} \quad 67$$

where the direction **b** is opposite of **a**. In the no-slip no penetration case shown in Figure 2 this generates:

$$f_1 = f_3$$

$$f_5 = f_7 - \frac{1}{2}(f_2 - f_4) \quad 68$$

$$f_8 = f_6 + \frac{1}{2}(f_2 - f_4)$$

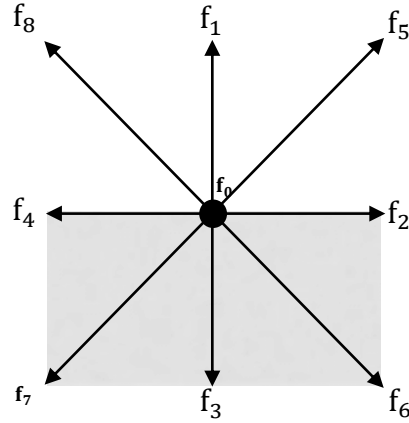


Figure 2. D2Q9 arrangement for the lattice located on the bottom boundary.

2.10.2. Periodic Boundary Conditions

Periodic boundary conditions become necessary to isolate repeating flow conditions. To explain this type of boundary condition, for instant, the leaving distribution functions from a line **a** same as the distribution functions entering to a line **b** and vice versa, as shown in Figure 3.

$$f_{8,a} = f_{8b}, f_{4,a} = f_{4,b}, \text{ and } f_{7,a} = f_{7,b} \quad 69$$

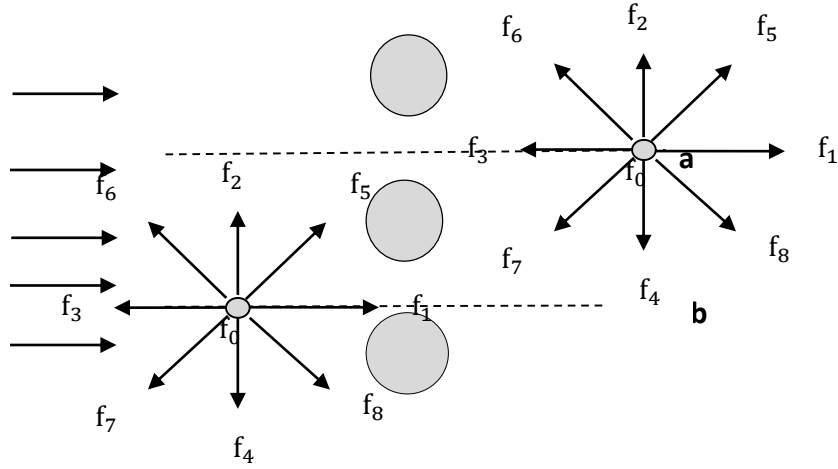


Figure 3. D2Q9 periodic flow boundary condition.

2.10.3. Neumann Boundary Conditions

Zou and He [33] and Kou and Chen [34] described a method to calculate the unknown distribution functions based on the conservation of mass and momentum in the x and y-direction. For D2Q9 arrangement there are three unknown distribution functions (f_2, f_5, f_6) and the density (ρ). They can be evaluated from:

The conservation of mass

$$\rho^\sigma = \sum_{k=0}^q f_k^\sigma \quad , \quad 70$$

The conservation of momentum in the x direction

$$\rho u = f_1 + f_5 + f_8 - f_6 - f_3 - f_7 \quad , \quad 71$$

The conservation of momentum in the y- direction

$$\rho v = f_5 + f_2 + f_6 - f_7 - f_4 - f_8 \quad , \quad 72$$

The equilibrium condition normal to the boundary; yields

$$f_1 - f_1^{eq} = f_3 - f_3^{eq}, f_2 - f_2^{eq} = f_4 - f_4^{eq} \quad 73$$

The Neumann boundary condition is shown in the Appendix A for D3Q19.

2.10.4. Symmetry Boundary Conditions

Many practical problems are symmetric about a line or a plane. Using symmetry boundary conditions will reduce the computational domain. The symmetry can be presented as a mirror of the three distribution functions around the symmetry line $a-a'$:

$$f_6 = f_7, f_2 = f_4, \text{ and } f_5 = f_8 \quad 74$$

The way to construct the symmetry is to set them equal to their mirror around the symmetry line, as shown in Figure 4.

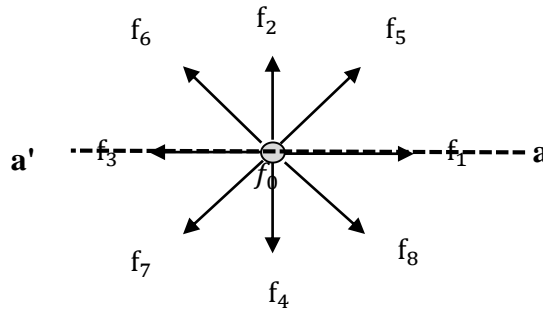


Figure 4. A symmetry boundary condition about a symmetry line $a-a'$.

2.11. Spatial Discretization

The Boltzmann equation is discretized and solved numerically. Each points of the discretized physical space of interest are assigned a lattice point. Each point is populated by discrete particles. These particles move from one lattice to another lattice site with

discrete velocities (e_k) and the colliding with each other at lattice nodes. Thus, the discretization form of the LB is referred to as the lattice Boltzmann equation. Generally, the lattice Boltzmann discretized equation is given by

$$\begin{aligned} \frac{f_k(\mathbf{r}, t + \delta_t) - f_k(\mathbf{r}, t)}{\delta t} + c_k \frac{f_k(\mathbf{r} + \Delta r, t + \delta_t) - f_k(\mathbf{r}, t + \delta_t)}{\delta r} \\ = -\frac{1}{\tau} [f_k(\mathbf{r}, t) - f_k^{eq}(\mathbf{r}, t)] \end{aligned} \quad 75$$

where $r = (x, y, z)$, $\delta r = (\delta x, \delta y, \delta z)$, $e_k = \frac{\text{Space}}{\text{time}} = \frac{\delta x}{\delta t} = \frac{\delta y}{\delta t} = \frac{\delta z}{\delta t} = \pm 1$. Note that $\delta r = e_k \cdot \delta_t$.

Equation (75) can be written as

$$f_k(\mathbf{r}, t + \delta_t) - f_k(\mathbf{r}, t) + f_k(\mathbf{r} + \delta r, t + \delta_t) - f_k(\mathbf{r}, t + \delta_t) = -\frac{\delta_t}{\tau} [f_k(\mathbf{r}, t) - f_k^{eq}(\mathbf{r}, t)] \quad 76$$

A simple algebraic manipulation yields:

$$f_k(\mathbf{r} + \delta r, t + \delta_t) - f_k(\mathbf{r}, t) = -\frac{\delta_t}{\tau} [f_k(\mathbf{r}, t) - f_k^{eq}(\mathbf{r}, t)] \quad 77$$

2.12. Temporal Discretization

To solve equation (75) and (76) numerically, the following temporal discretization is adapted:

$$f_k(\mathbf{r} + \delta r, t + \delta_t) - f_k(\mathbf{r}, t) = -\int_t^{t+\delta_t} \frac{f_k(\mathbf{r}, t) - f_k^{eq}(\mathbf{r}, t)}{\tau} dt \quad 78$$

The integrand of the right hand side of the equation (78) is assumed to be constant over one time step. That is the first integrand in the collision term which is treated explicitly, using the first order approximation. This assumption yields an artificial viscosity that can be absorbed into the real viscosity of fluid.

CHAPTER 3: TURBULENT FLOWS PAST CYLINDERS

3.0. Objective

The novel lattice Boltzmann method introduced by the present author is used to simulate turbulent flows past a cylinder. The regularized multi-relaxation lattice Boltzmann model is expected to improve the stability of the single relaxation time lattice Boltzmann method. Simulations are conducted for a wide range of the Reynolds number. In order to validate the model, predicted results from the regularized MRTLBM are compared against measured results. Turbulent flows past a cylinder are selected here to validate the newly introduced model since these flows are well-characterized and well-documented.

3.1. Introduction

Several investigators studied the flow past a circular or a square cylinder using single relaxation time lattice Boltzmann method (SRT) [35]. These studies showed that SRT becomes unstable at high values of the Reynolds number. In order to improve the stability by previous investigators is proposed a multi-relaxation time or a regularized lattice Boltzmann method. Regularized and multi-relaxation time (RLBM and MRT) proposed by the present author is employed to study turbulent flow past a single and arrays of cylinders for a wide range of the Reynolds number. The method is shown to be stable for Reynolds number as high as 21400.

3.2. A Mathematical Model

The RLBM and MRT LBM have been implemented to study turbulent flows past a single and arrays of cylinders. The predicted results have been compared with those obtained by experimental observations and by large eddy simulations [37,38]. The schematic diagrams

shown in Figure 5 illustrates the geometries considered. At the inlet the velocity profile is fully developed and it is normalized by the average velocity. The cylinder is located on $5D$ away from the inlet where D is the hydraulic diameter, $D = 4A/P$. The conservation of mass and momentum are applied in the upper and the lower boundary. These boundary conditions are referred to as Neumann boundary conditions. For the inline cylinders geometry, the distance between the origins of two successive cylinders is $2.5D$. For the staggered geometry, the cylinders are offset by T/D . No-slip and no-penetration conditions are imposed at the upper and the lower walls of the channel. At the inlet the velocity profile is

$$U = 4 \times U_{\max} (Y - Y^2) \quad 79$$

where U_{\max} is the maximum velocity at the center.

At the outlet the pressure is set to be constant. The pitch ratio (PR) is placed to be the same for the inline and the staggered geometry, as shown in Figure 5.

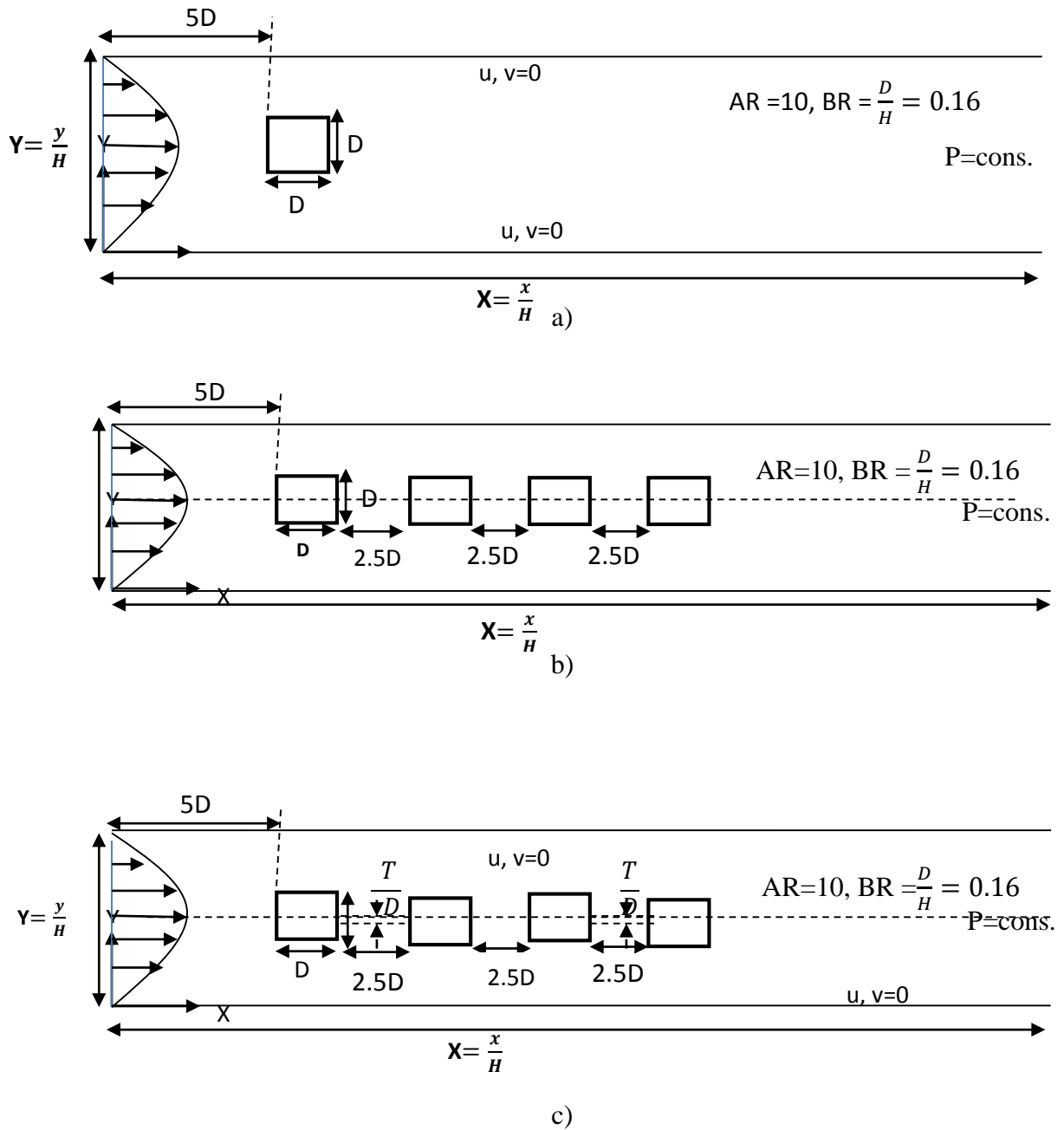


Figure 5. The schematic diagram of various geometries: a) the single cylinder, b) the in-line arrangement, and c) the staggered arrangement for $AR=10$.

The schematic diagram of geometries used in the present study is shown in Figure 5. AR is the aspect ratio and BR is the blockage ratio.

The force exerted by the fluid on the cylinder is determined from

$$F = \sum_{\text{all } x_b} \sum_{k=1}^{N_b} e_k [f_k(x_b, t) + f(x_b + \Delta x_b, t)] \times (1 - \phi(x_b + \Delta x_b)) \frac{\Delta x}{\Delta t} \quad 80$$

where N_b is the non-zero lattice velocity vectors and $\phi(x_b + \Delta x_b)$ is an indicator. The indicator can be defined as

$$\phi = \begin{cases} 0 & \text{at } x = x_f \\ 1 & \text{at } x = x_b \end{cases} \quad 81$$

where x_f is the fluid location and x_b is the boundary location

The coefficient of drag and lift are defined as

$$C_l = \frac{2 \times F}{\rho A U_{av}^2} \quad 82$$

$$C_D = \frac{2 \times F_x}{\rho A U_{av}^2} \quad 83$$

where A is the projected area ($A = D$), and the average velocity is

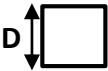
$$U_{av} = \frac{2}{3} U_{max} \quad 84$$

The Strouhal number is determined from

$$St = \frac{fD}{U_{max}} \quad 85$$

where f is the frequency of oscillations.

The geometric parameters are listed in Table 1.5.

Single square cylinder obstacle		Reynolds number ($Re = U_{max} D/v$)	
		50	250
Number of grids	N_x	150	350
	N_y	500	600
The actual velocity in m/sec	U_{max}	2.4×10^{-3}	0.0122
The size of the obstacle (Hydraulic diameter)		$D = 0.02048$ m, The scaling of the diameter D is ($D_o = D/H = 0.16$)	
The height of the channel	H	$H = 0.128$ m	
Max. velocity per unit lattice	U_{max}	0.1 (lu/ts)	
Blockage ratio	BR	0.16	
Inflow length	L_o	2D	
Aspect ratio	AR	10	
The length of the channel	$L = AR \times H$	1.28 m	
Inline and staggered square cylinder obstacle		Reynolds number ($Re = U_{max} D/v$)	
		50	250
Number of grids	N_x	150	350
	N_y	500	600

Pitch (spacing)	$SP = PR \times D$ where PR is the pitch ratio which is =2.5	If $PR = 2.5$, $SP = 0.1024m$, The scaling of spacing SP is SP_0 , thus $SP_0 = i \times D_0$ where, $i = 5$, $SP_0 = 0.625$
Normalized offset	T/D	0.25

Table 1.5. Geometric parameters

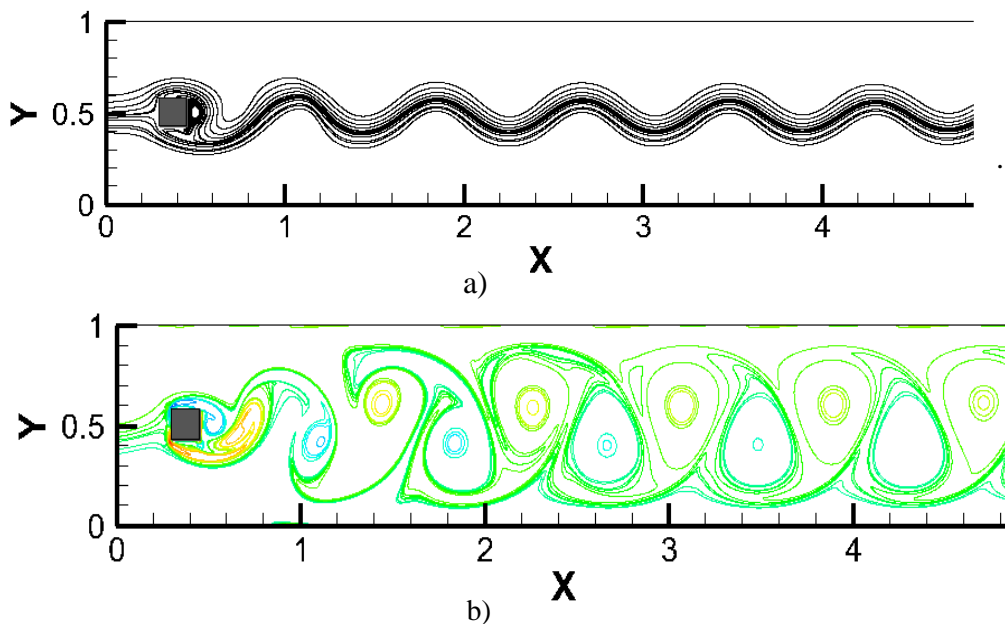
3.3. Results and Discussions

In this section the spatial and temporal structure of the flow in a single and arrays of square cylinder will be presented for the Reynolds number up to 20000 for a blockage ratio of 1/6. The spatial and temporal structures of flow are also presented for the Reynolds number of 21400 for a blockage ratio of 1/14. Simulations are carried out for various geometries: a single cylinder; tandem arrays; and staggered arrays. A wide range of the Reynolds number for selected blockage ratio is considered. Dimensions of all geometries are listed in Table 1.5.

The present and previous studies prove that flows pass bluff bodies can be simulated for the Reynolds number up to 1000 by employing a single relaxation lattice Boltzmann method. Above such Reynolds number the method becomes unstable. It is also demonstrated here that by utilizing multi-relaxation time lattice Boltzmann method the stability boundary can be extended to the Reynolds number of about 10000. Simulations

are conducted by employing the newly proposed regularized multi-relaxation lattice Boltzmann method to demonstrate that the stability boundaries can be extended further.

Figure 6 illustrates the streamlines, contours of vorticity, lift coefficient versus time, and the power spectrum of the lift coefficient at the representative Reynolds number of 250 for a single cylinder geometry. The streamlines and the vorticity contours clearly indicate the presence of eddies downstream of the blockage. The eddies are formed in the wake region directly behind the blockage. When the eddy becomes sufficiently large they detach. This phenomenon is referred to as vortex shedding. As typical of vortex shedding the position of the vortex is alternating between the top and the bottom of the wake region. This is demonstrated by the periodic nature of the lift coefficient. Power spectrum density of the lift coefficient leads to a dominant frequency, f , of 0.1017 Hz. The corresponding Strouhal number for the vortex shedding, St , is 0.1707.



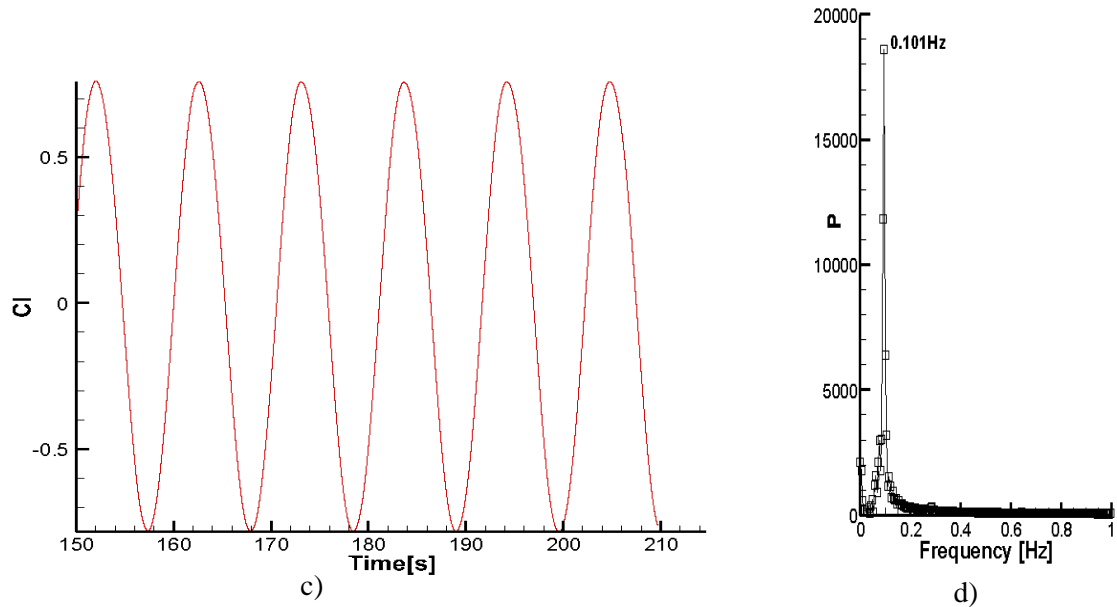
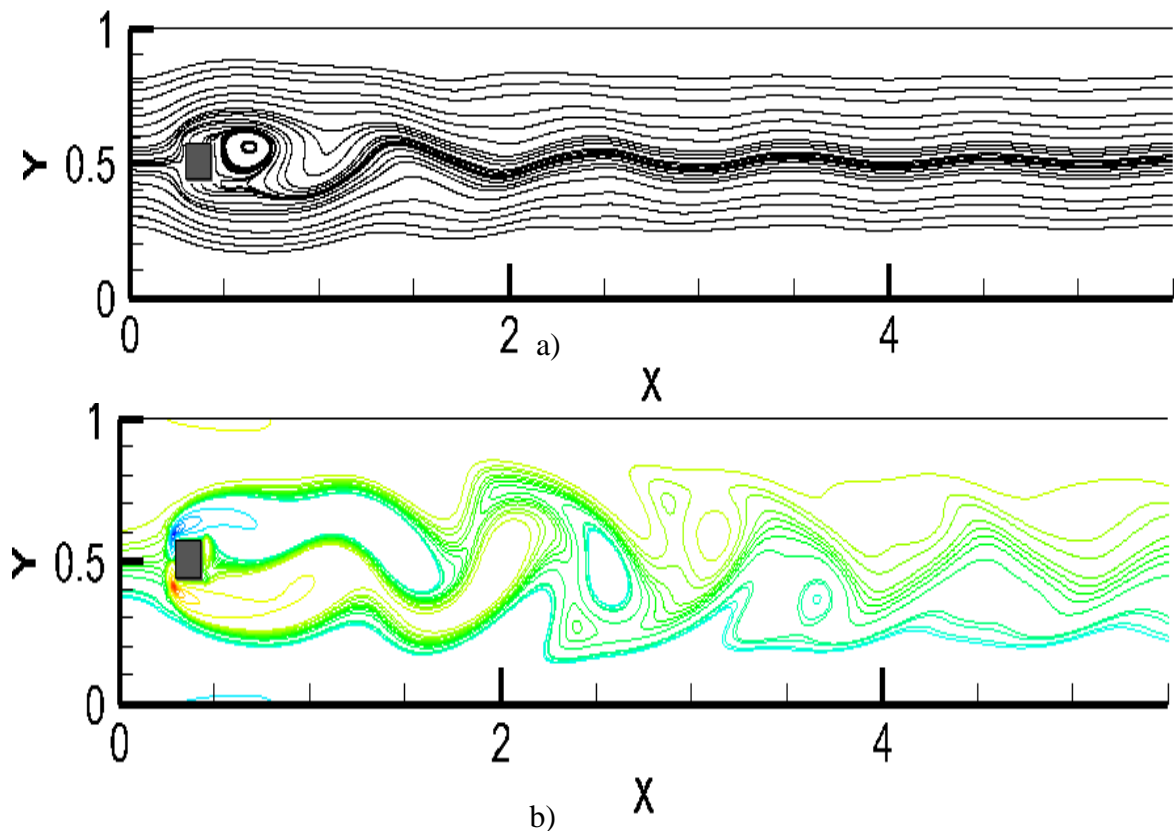
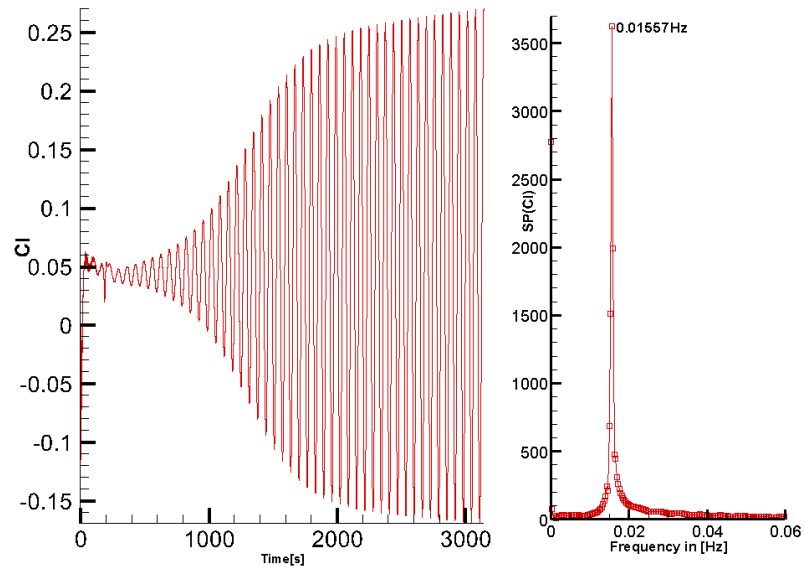


Figure 6. a) Instantaneous streamlines , b) instantaneous vorticity contours , and c) the lift coefficient versus the time , and d) the power spectrum of the lift coefficient at $Re = 250$ for a single cylinder geometry.

Figures (6-11) show the instantaneous streamlines and contours of vorticity for Reynolds number of 50,100,500, 1000, 10000, and 20000 for flow past a single cylinder geometry. At $Re = 50$, the vortex shedding from the cylinder alternates from the top and the bottom corner. The alternating vortex is not well organized but the flow in the wake region is almost perfectly periodic. This is obvious from the lift coefficient as a function of time, as shown in Figure 7. At Reynolds number of 100 and 500 the counter-rotating vortices are uniformly spaced downstream of the blockage, as shown in Figures 8 and 9. There is very little indication of interaction between the eddies and the boundaries. The vortices are losing strength downstream in the region further of the cylinder due to dissipation. When the Reynolds number is increased to 1000, the periodic nature of the flow is complicated by the boundary effects, as shown in Figure 10. Secondary eddies are forming near the boundaries, which are in turn causing a reorientation of the primary eddies shed from the

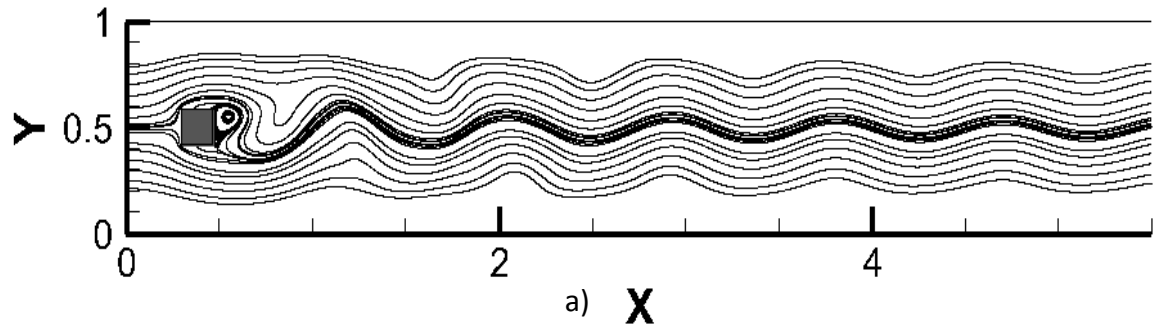
body. Clearly, this effect is very pronounced, as it can be seen even in the streamlines. As Reynolds number increases to 10000 and 20000 the influence of the boundary on eddies becomes stronger, as shown in Figure 11. This is evidenced by the secondary eddies which formed near the boundaries. By the Reynolds number of 10000 these secondary eddies are as large as the primary eddies formed by the blockage as shown in Figure 11. It is possible that the primary vortices are splitting, but it is difficult to tell since the secondary eddies have become nearly indistinguishable from the primary eddies. It should also be noted that as the Reynolds number increases the position at which the boundary effects become significant is pushed further downstream.



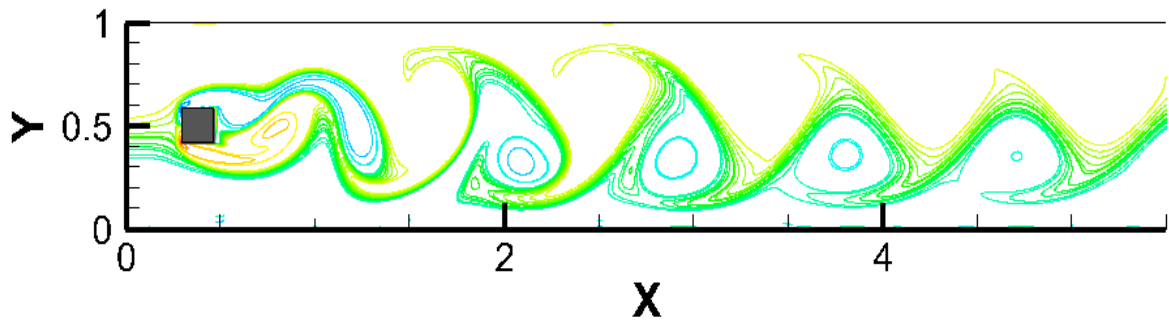


c)

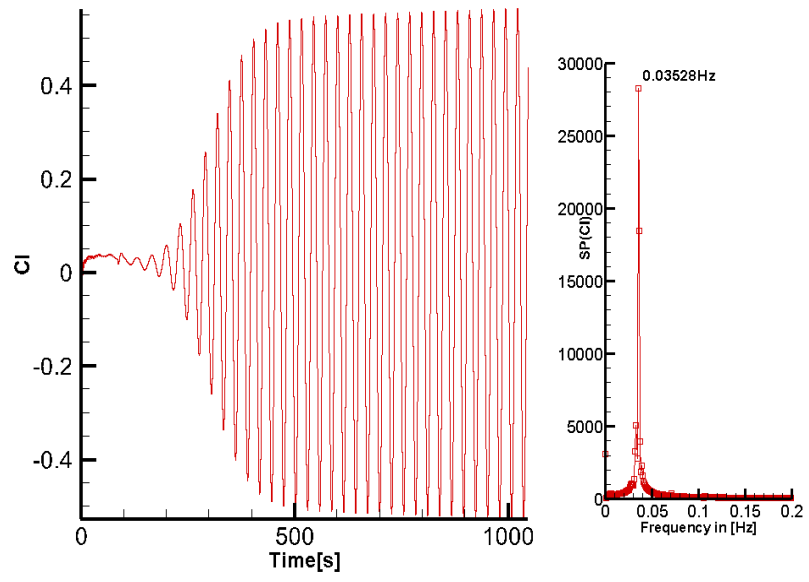
Figure 7. a) Instantaneous streamlines, b) instantaneous vorticity contours, and c) the lift coefficient vs time and the Fast Fourier Transform of the lift coefficient at $Re = 50$.



a) **X**

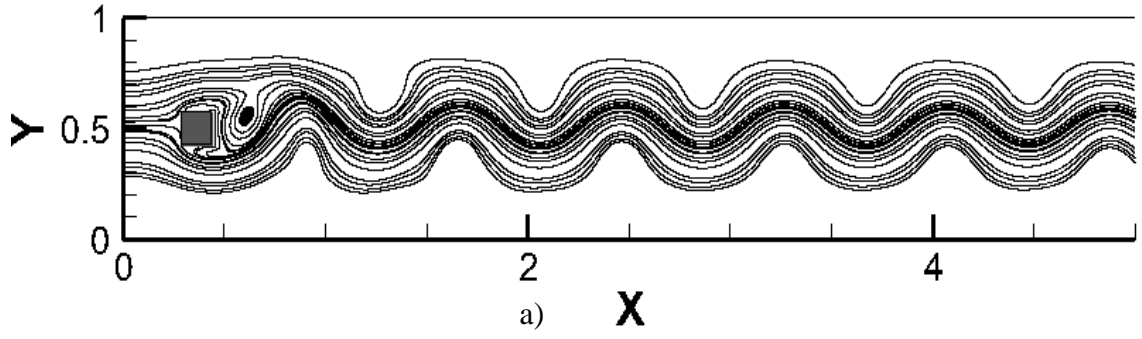


b)

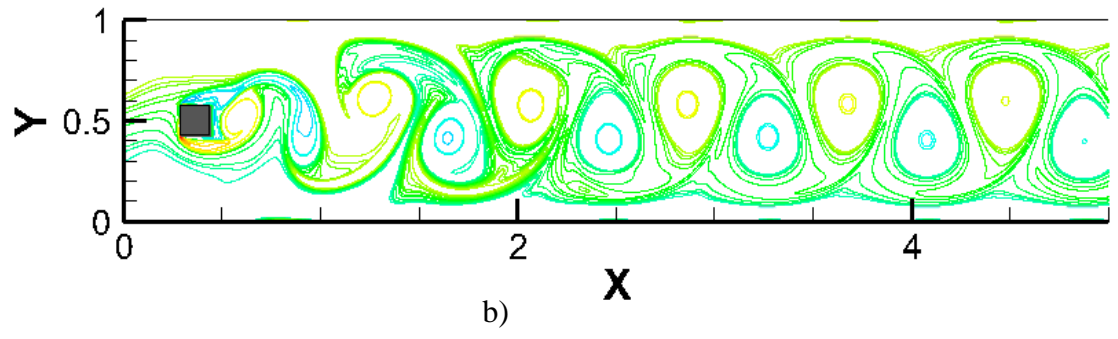


c)

Figure 8. a) Instantaneous streamlines , b) instantaneous vorticity contours, and c) the lift coefficient vs time and the Fast Fourier Transform of the lift coefficient at $Re = 100$.



a)



b)

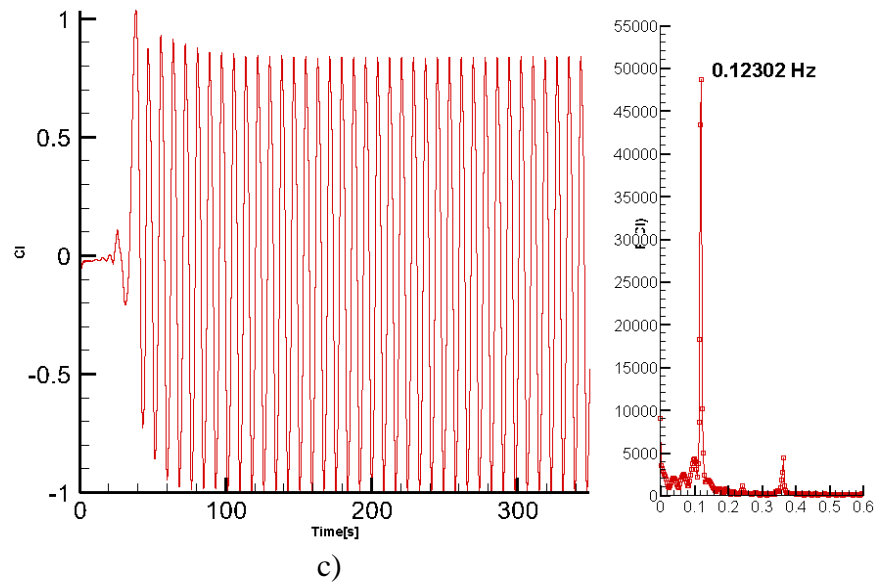
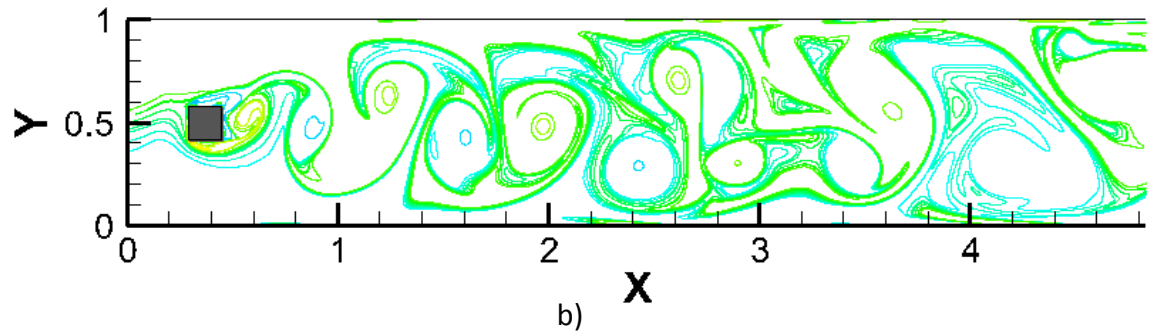
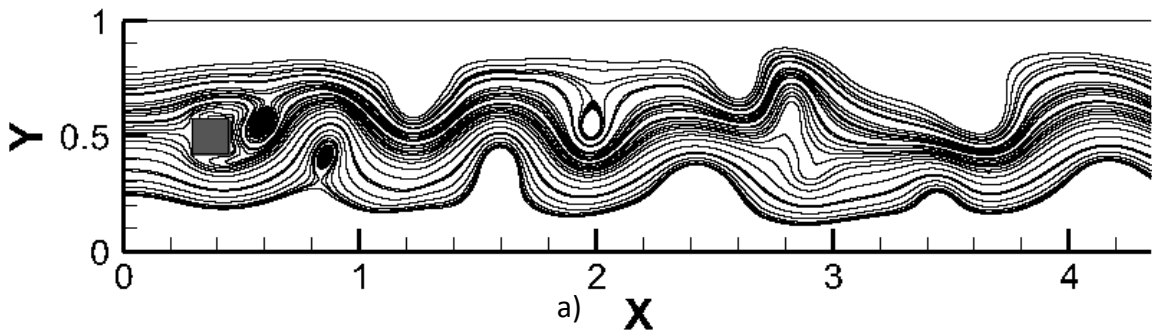
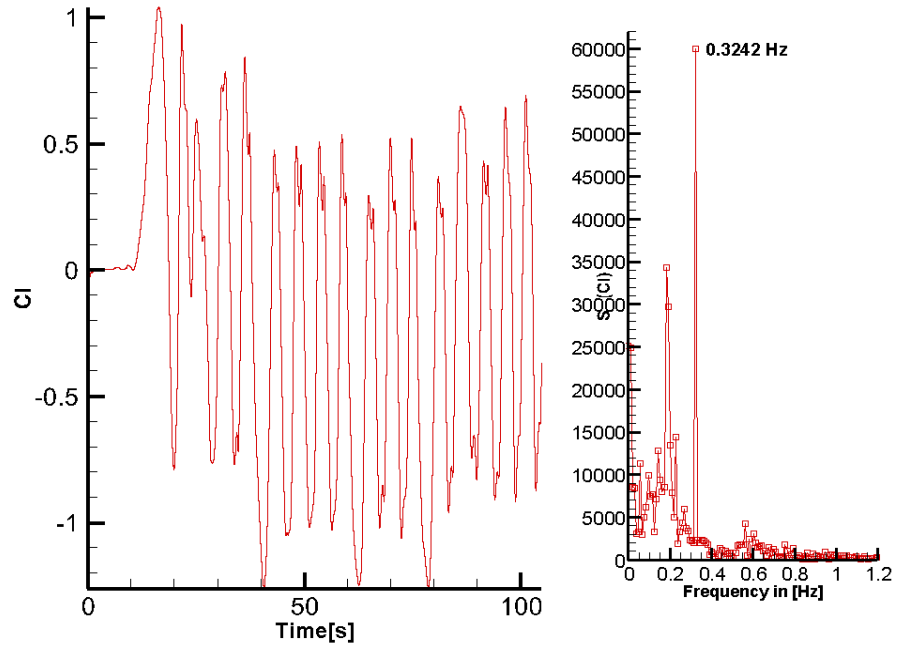


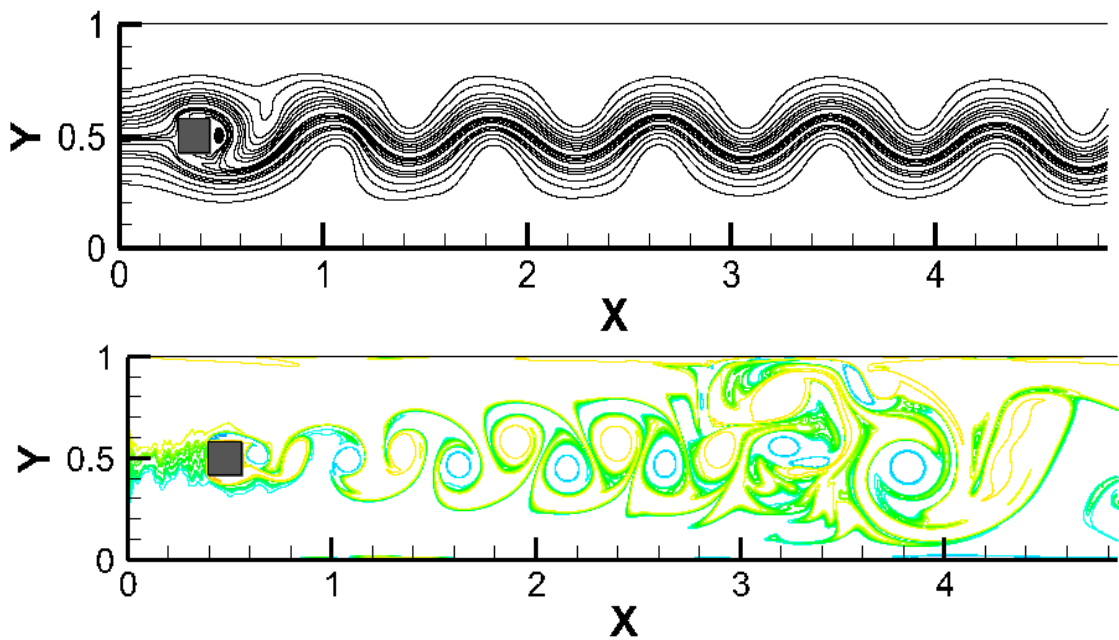
Figure 9. a) Instantaneous streamlines, b) instantaneous vorticity contours and c) the lift coefficient vs time and the Fast Fourier Transform of the lift coefficient at $Re = 500$.



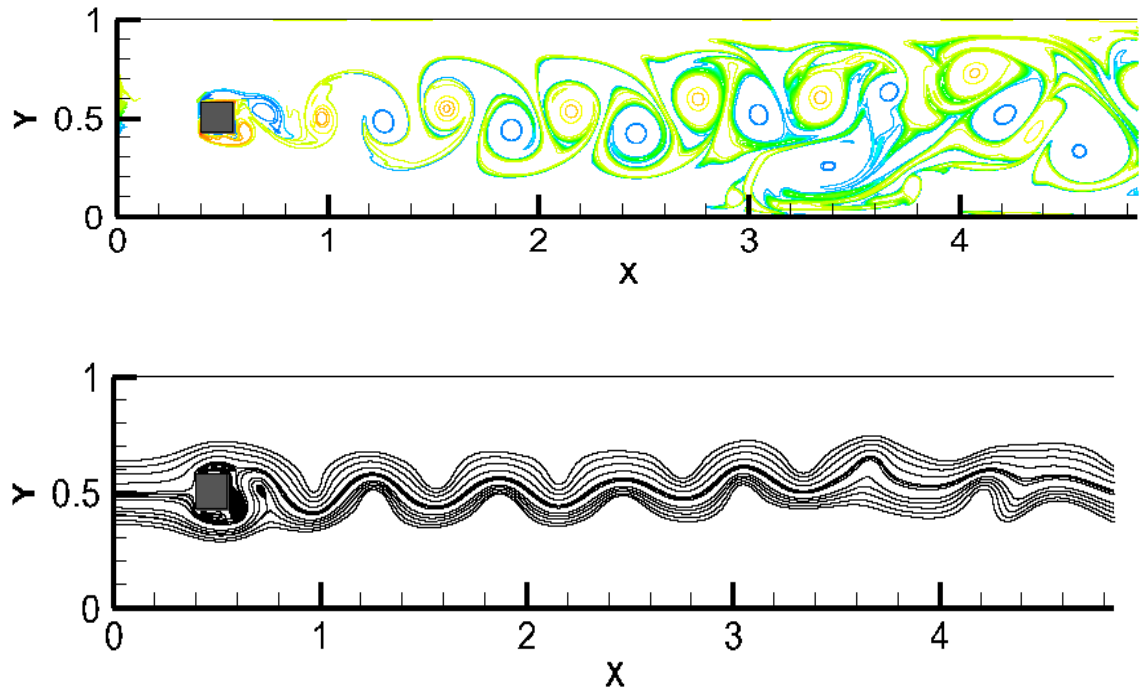


c)

Figure 10. a) Instantaneous streamlines, b) instantaneous vorticity contours and c) the lift coefficient vs time and the Fast Fourier Transform of the lift coefficient at $Re = 1000$.



a) $Re = 10000$



b) $Re = 20000$

Figure 11. Instantaneous streamlines and vorticity contours at various Reynolds number: a) 10000 and b) 20000 for flow past a single cylinder.

It is shown that the vortex shedding frequencies increases as the Reynolds number increases, as shown in Figures (7-10). The instantaneous vortices and streamlines contours depicted in Figures (7-11) clearly indicate that the flow induced by the vortex shedding has well organized structures. The vortices shed by the cylinder interact with the boundary layer.

Next, the results are presented for inline and staggered geometries for various values of the Reynolds number. The instantaneous streamlines and iso-vorticity contours for flow past a square cylinder have been examined. The lift coefficients of different cylinders in these flows are calculated and the Strouhal number are determined for various values of the Reynolds number. For the inline geometry at $Re = 50$. Flow patterns behind each cylinder

are similar. Figure 13 depicts the lift coefficients of each cylinder. They are nearly the same. Fast Fourier transform is applied to determine the dominant frequency of the periodic flow structure. The frequency of the vortex shedding from all cylinders is the same, as shown in Figure 13. Figures (12-20) show streamlines, vorticity contours and lift coefficients for the inline geometry at $Re = 100, 500, 1000, 10000,$ and 20000 . As Re increases the flow patterns behind the second cylinder and other downstream cylinder differ significantly compared to the flow pattern in the wake of the first cylinder. The interaction of eddies with the boundary layer becomes much stronger. The vortex shedding patterns from each cylinder differ significantly, as shown in Figures 13,15,17,and19. The frequencies of vortex shedding from cylinders at Re about 500 become different. Figures (21-27) show the instantaneous streamlines and vortices patterns for the staggered geometry at various values of the Reynolds number. They are shown that the vortex shedding frequencies in the leading, the trailing and in the middle cylinders are the same up to $Re = 500$. For $Re \geq 1000$ the shedding frequencies are different from cylinders. The magnitude of the lift coefficients for each cylinder is also different. The frequencies of the vortex shedding in the staggered geometry is higher than the frequencies of the vortex shedding in the inline geometry.

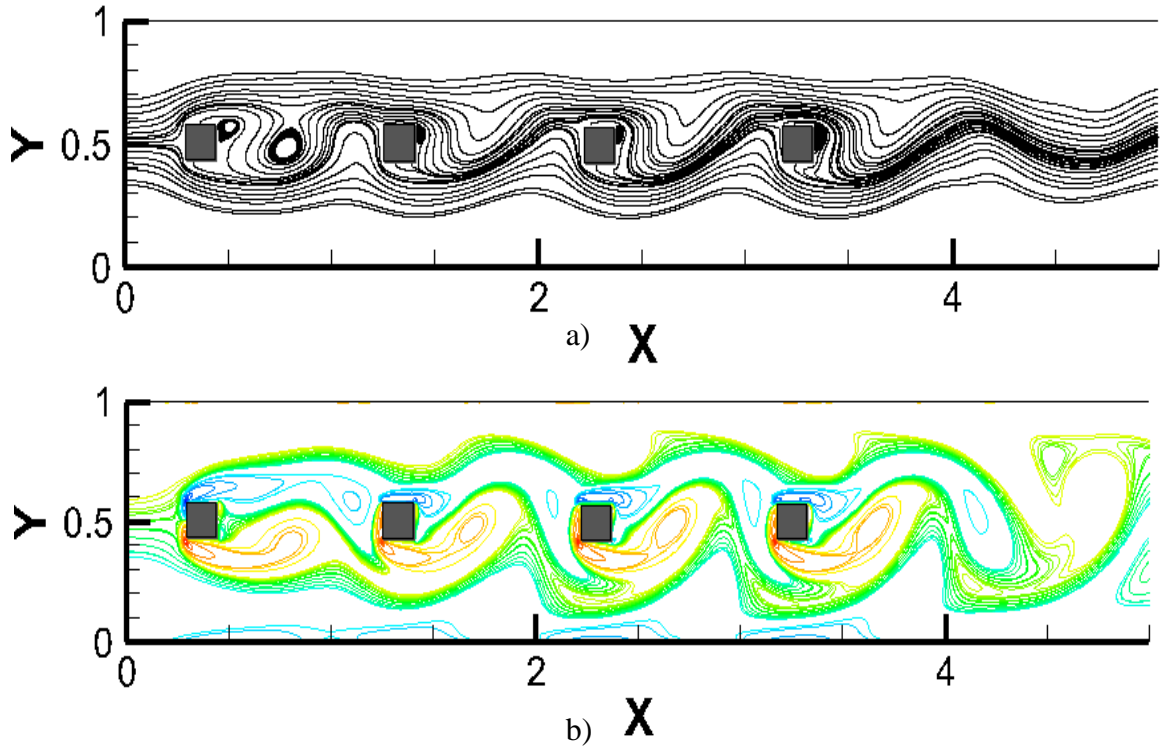
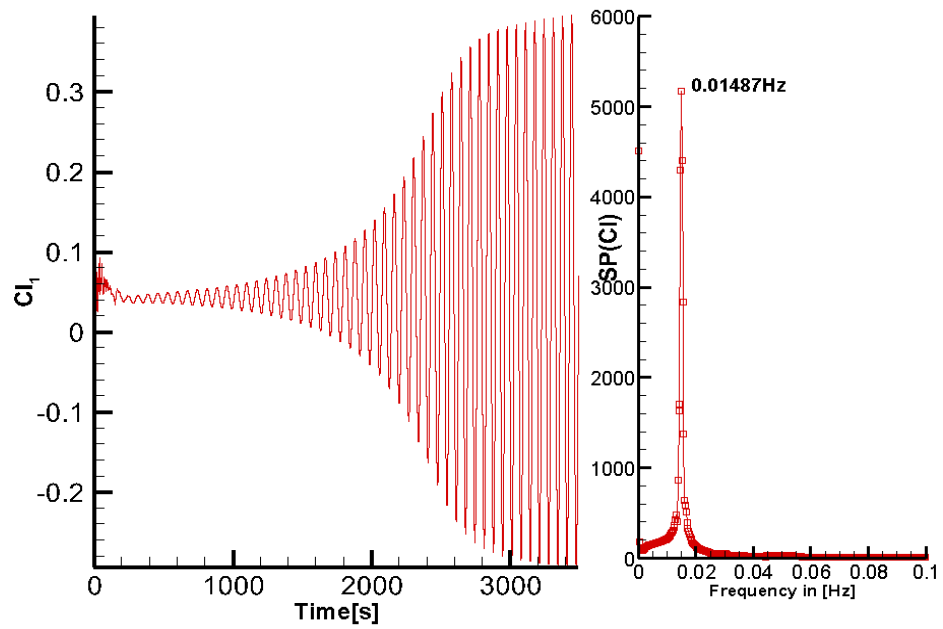
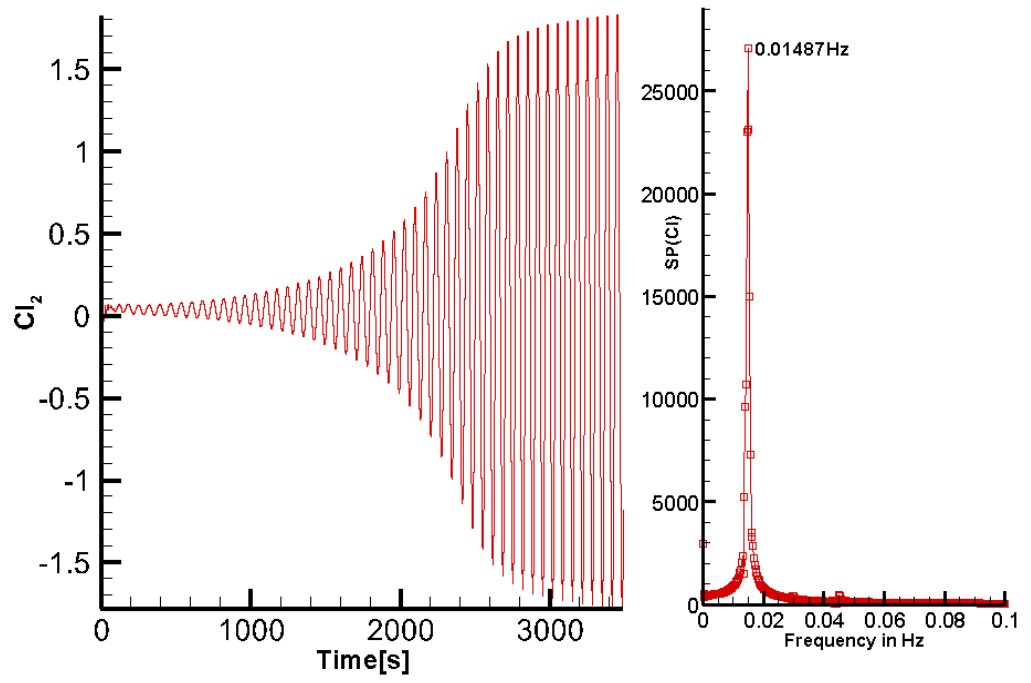


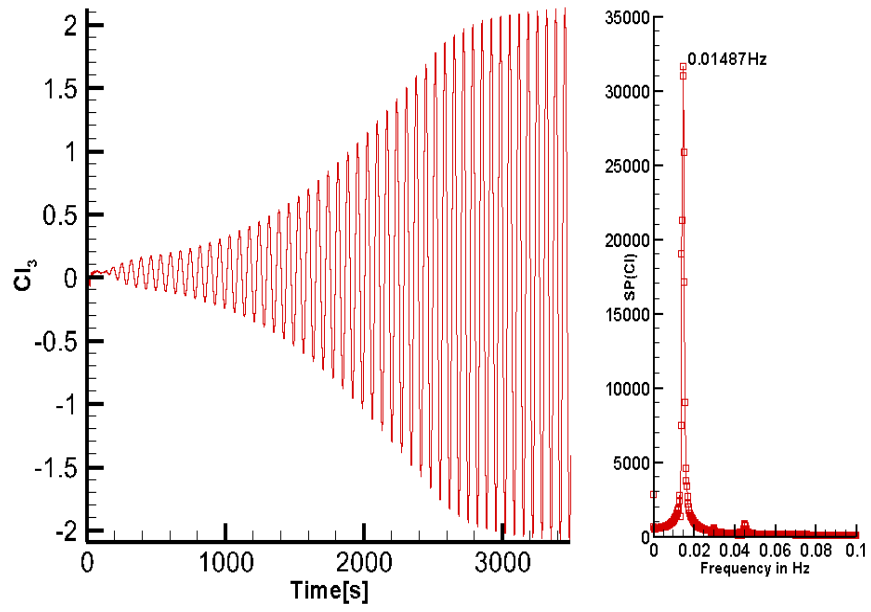
Figure 12. a) Instantaneous streamlines and b) instantaneous vorticity contours for flow past inline cylinders at $Re = 50$.



a)



b)



c)

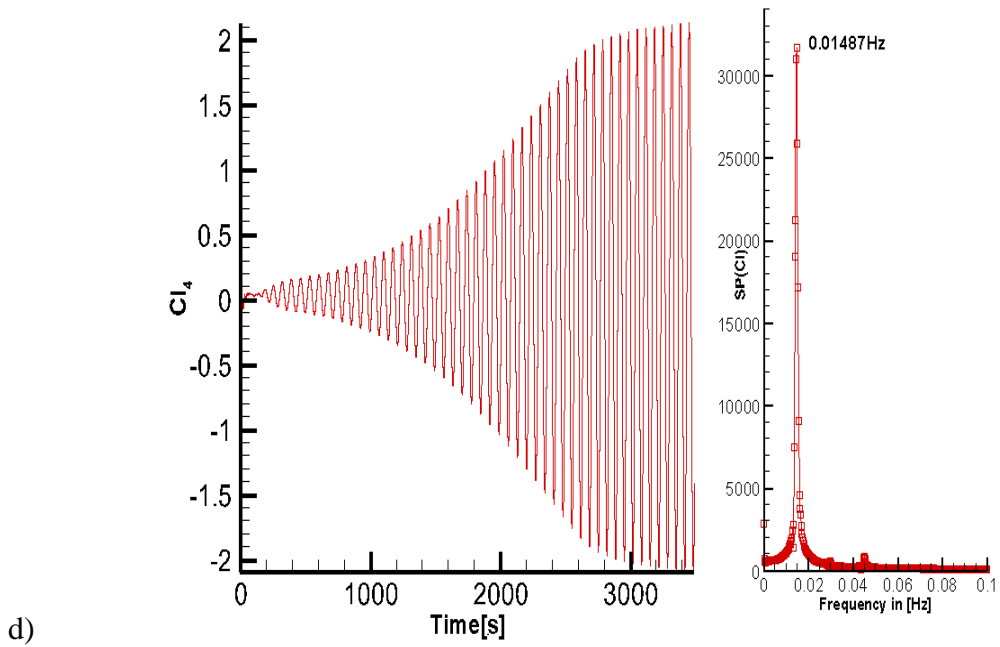


Figure 13. The lift coefficient vs time and the FFT of the lift coefficient. The lift coefficient is calculated a) 1st cylinder, b) 2nd cylinder , c) 3rd cylinder , and d) 4th cylinder at $Re = 50$.

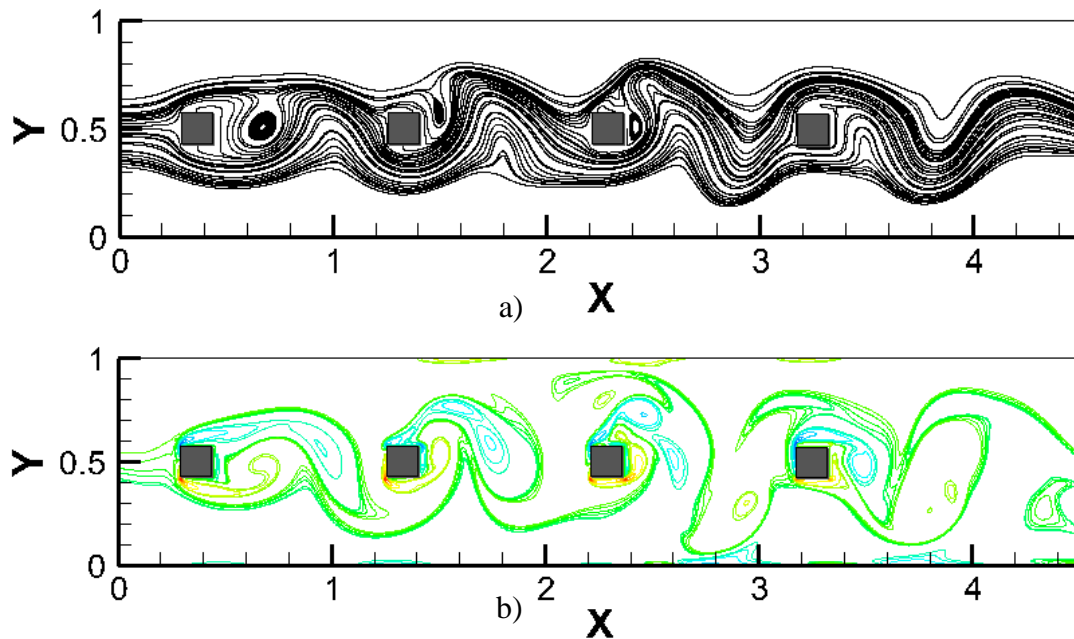
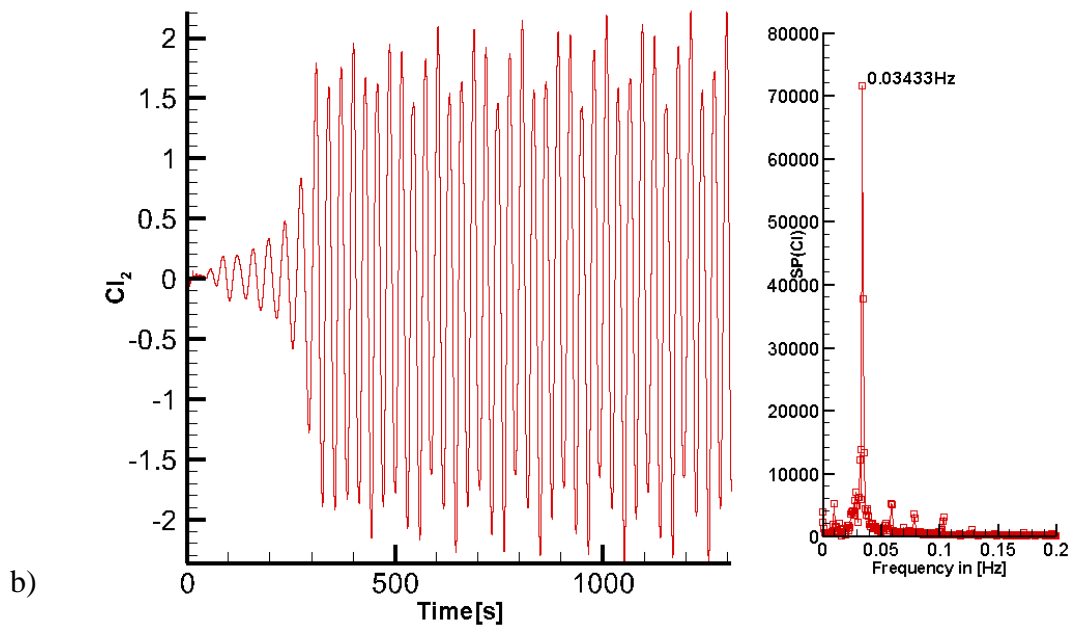
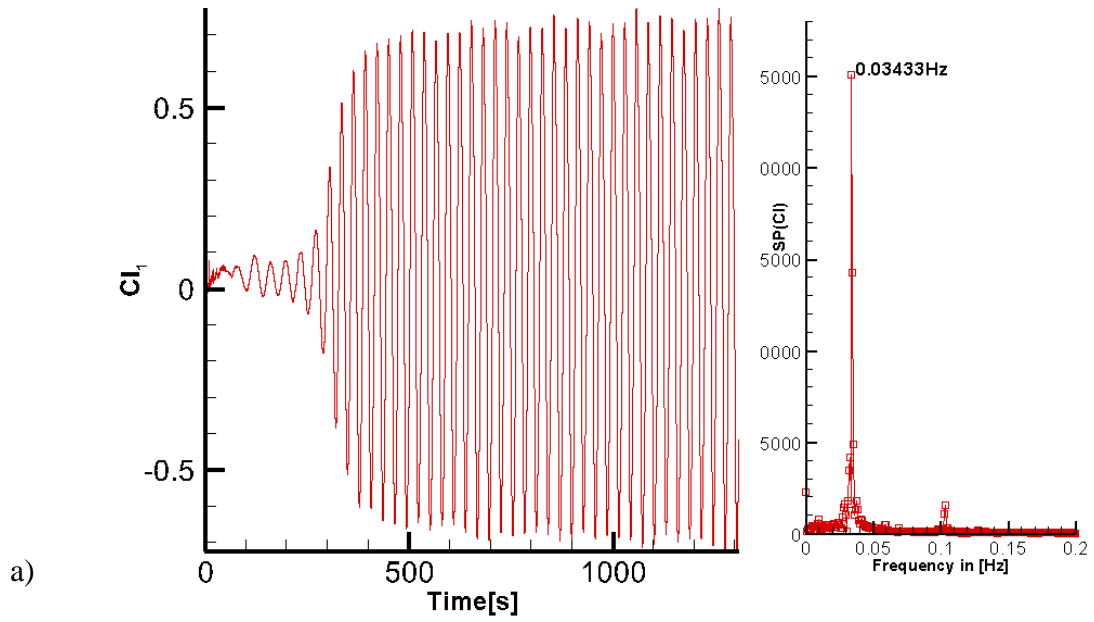


Figure 14. a) Instantaneous streamlines and b) instantaneous vorticity contours for the flow past inline cylinders at $Re = 500$.



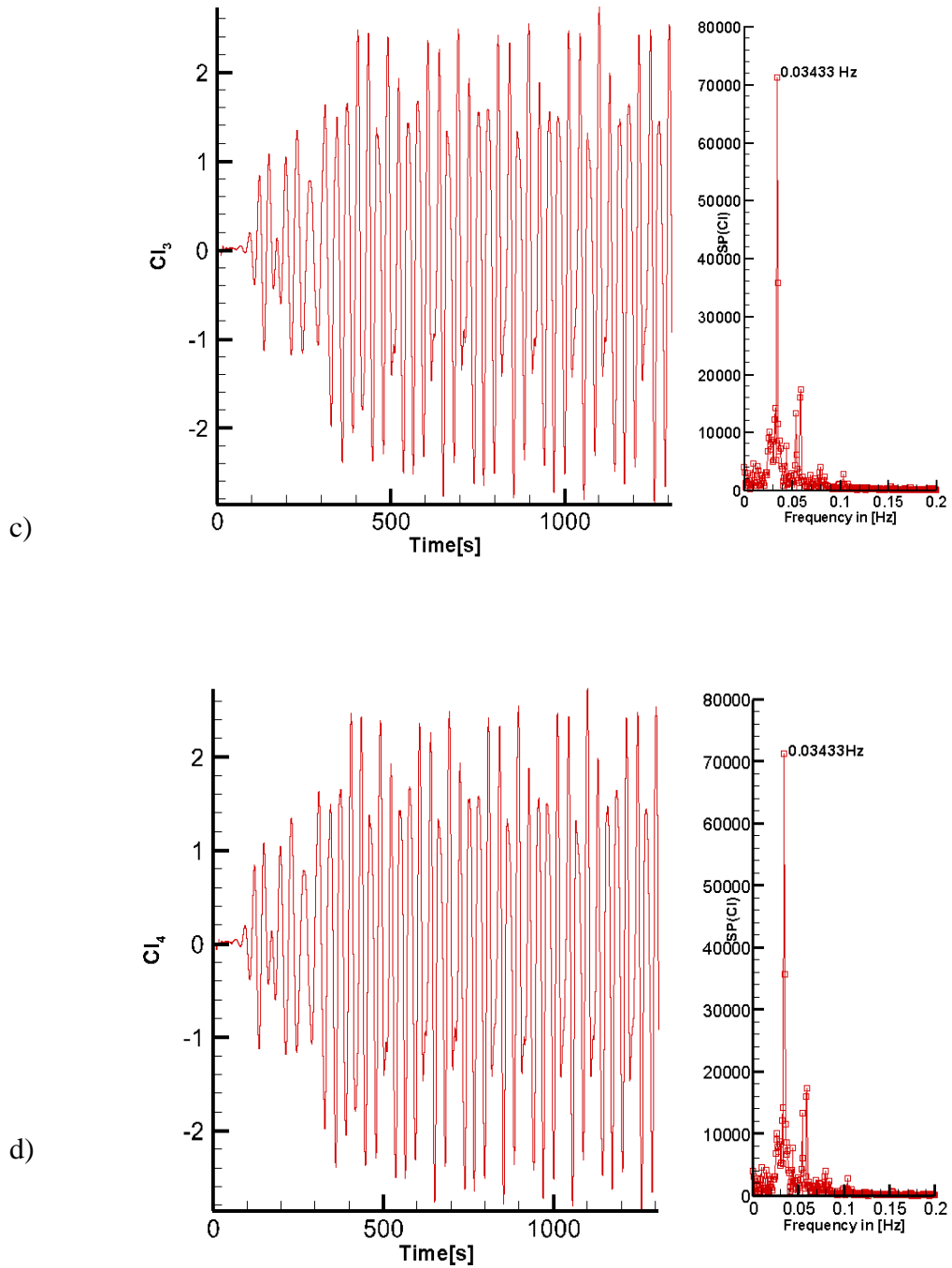


Figure 15. The lift coefficient vs time and the FFT of the lift coefficient. The lift coefficient is calculated a) 1st cylinder, b) 2nd cylinder, c) 3rd cylinder, and d) 4th cylinder at $Re = 100$.

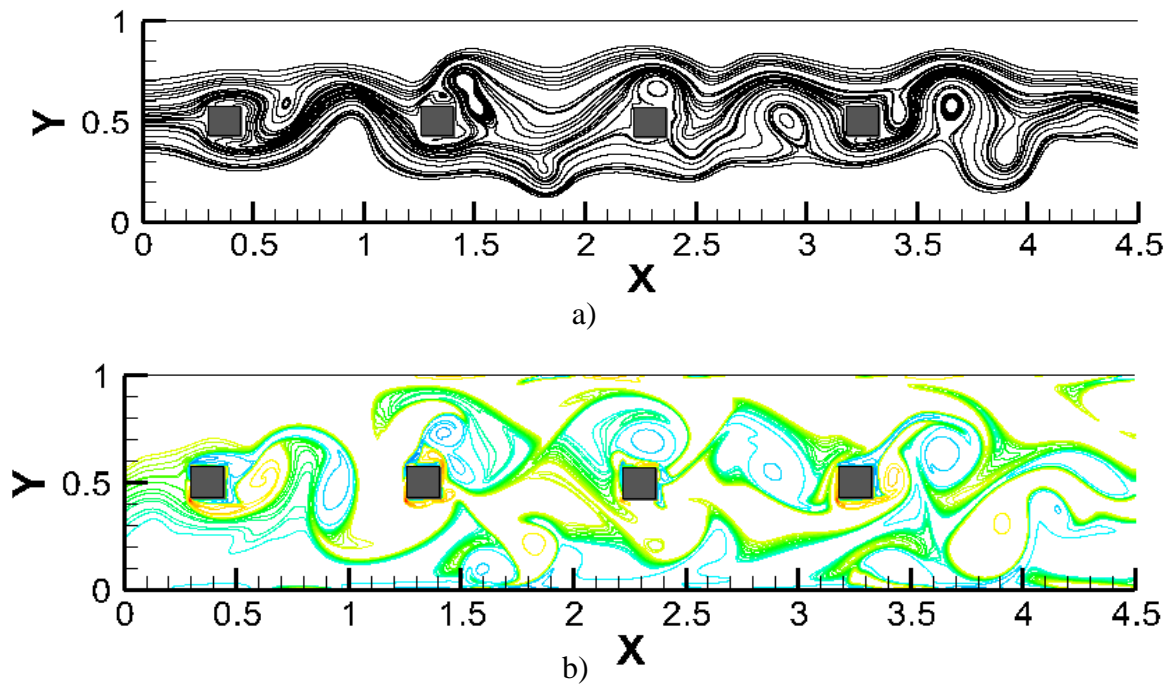
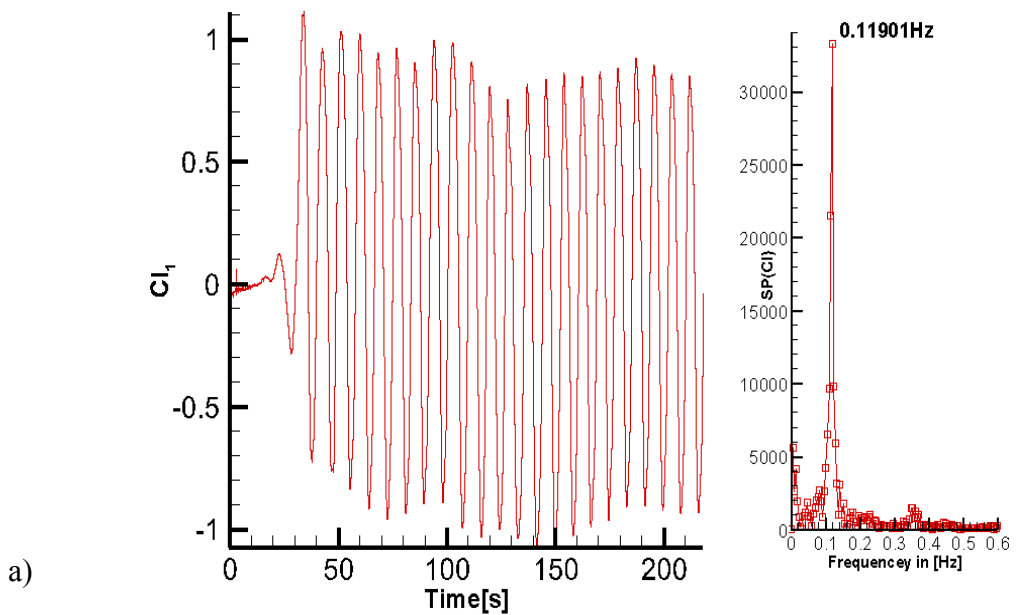
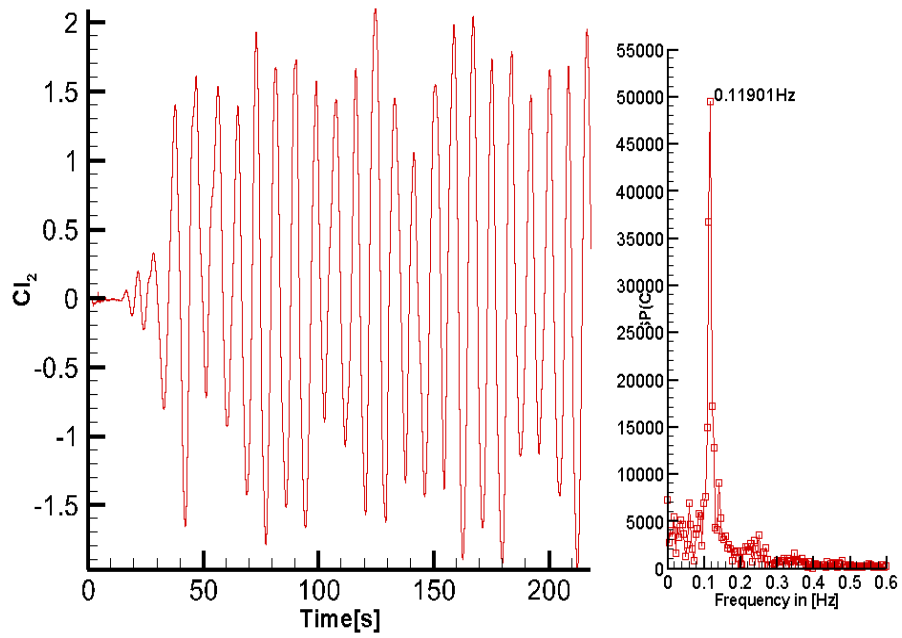
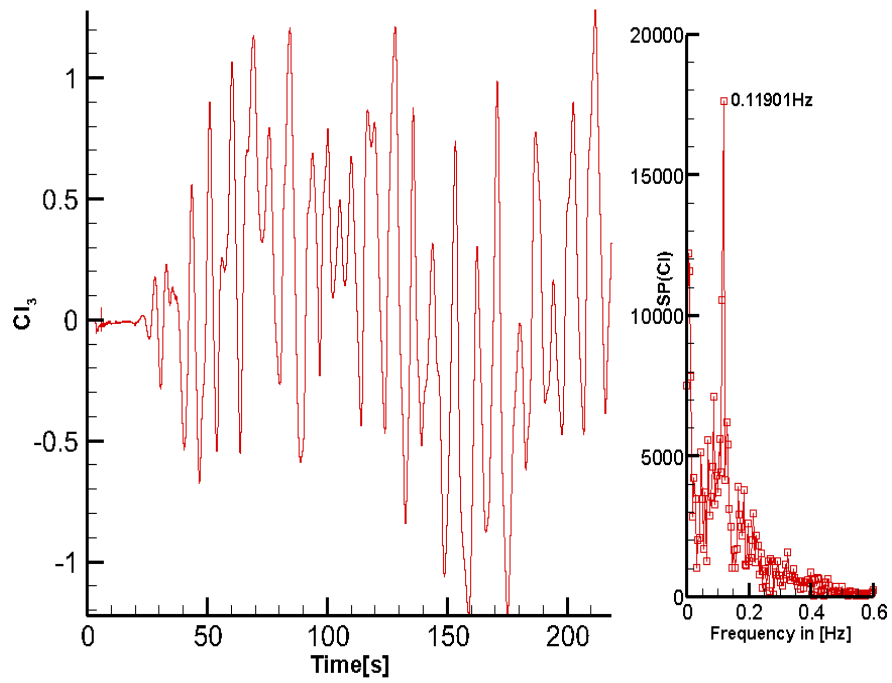


Figure 16. Instantaneous streamlines and b) instantaneous vorticity contours for flow past inline cylinders at $Re = 500$.





b)



c)

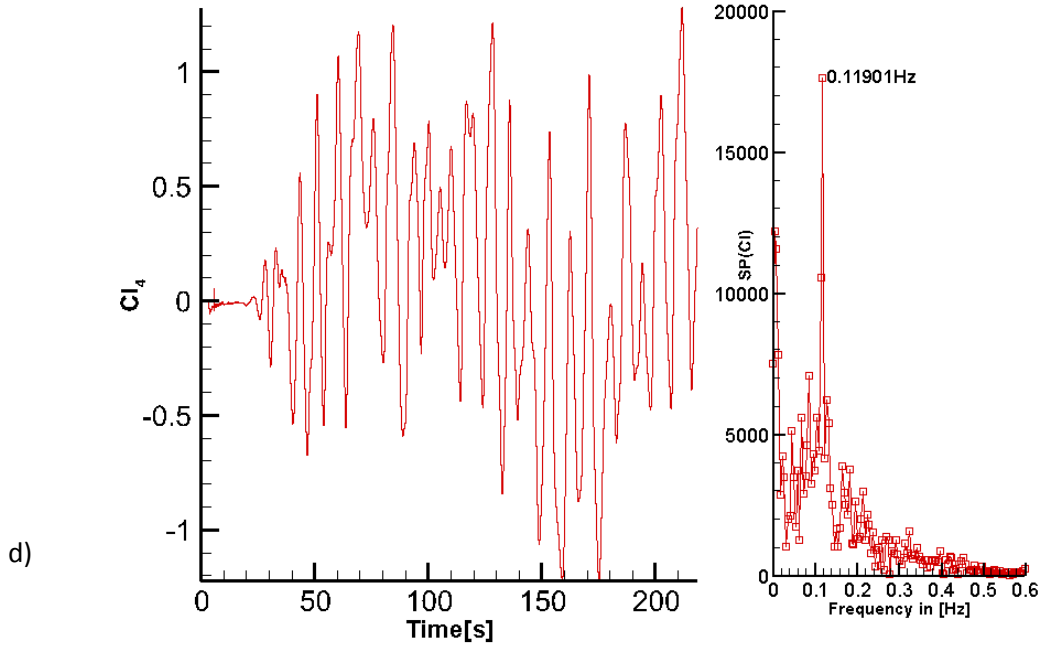


Figure 17. The lift coefficient vs time and the FFT of the lift coefficient. The lift coefficient is calculated a) 1st cylinder, b) 2nd cylinder , c) 3rd cylinder , and d) 4th cylinder at $Re = 500$.

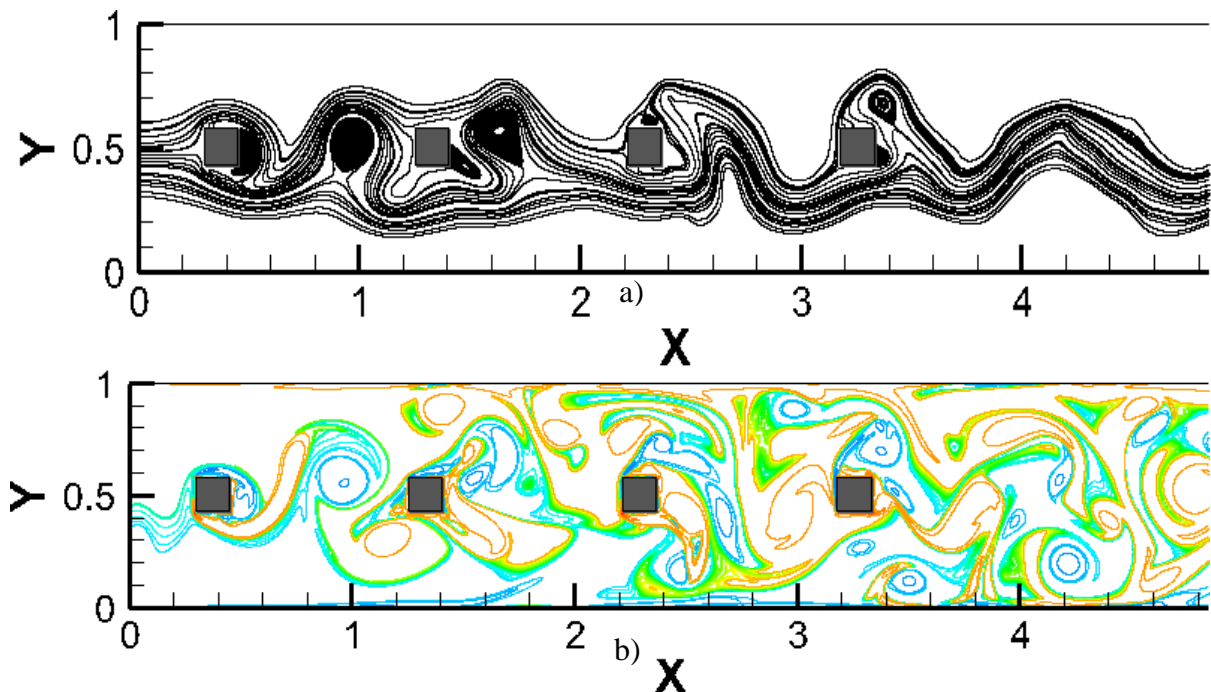
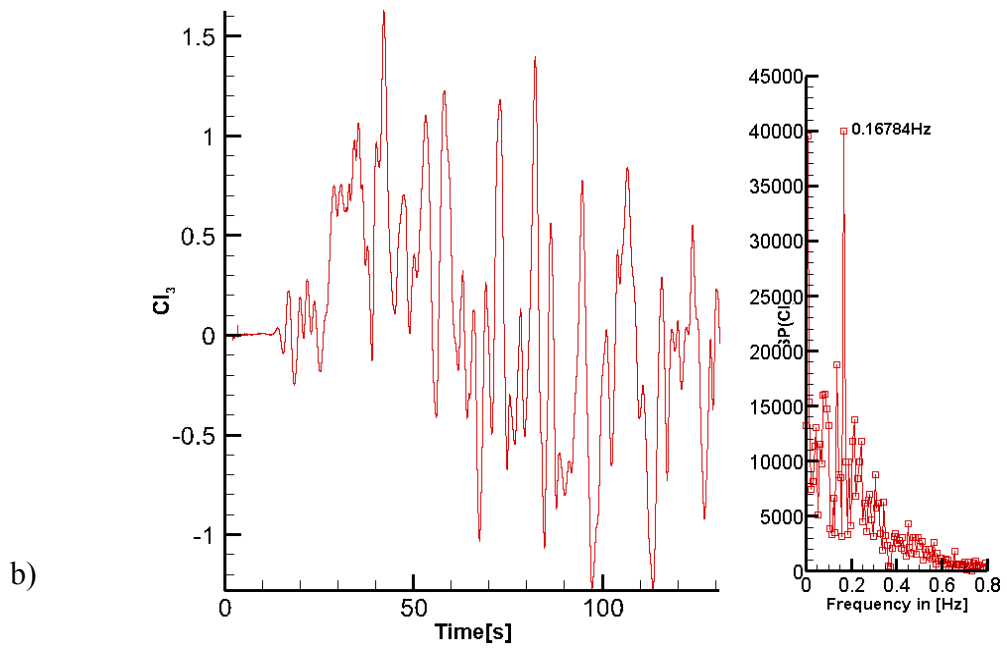
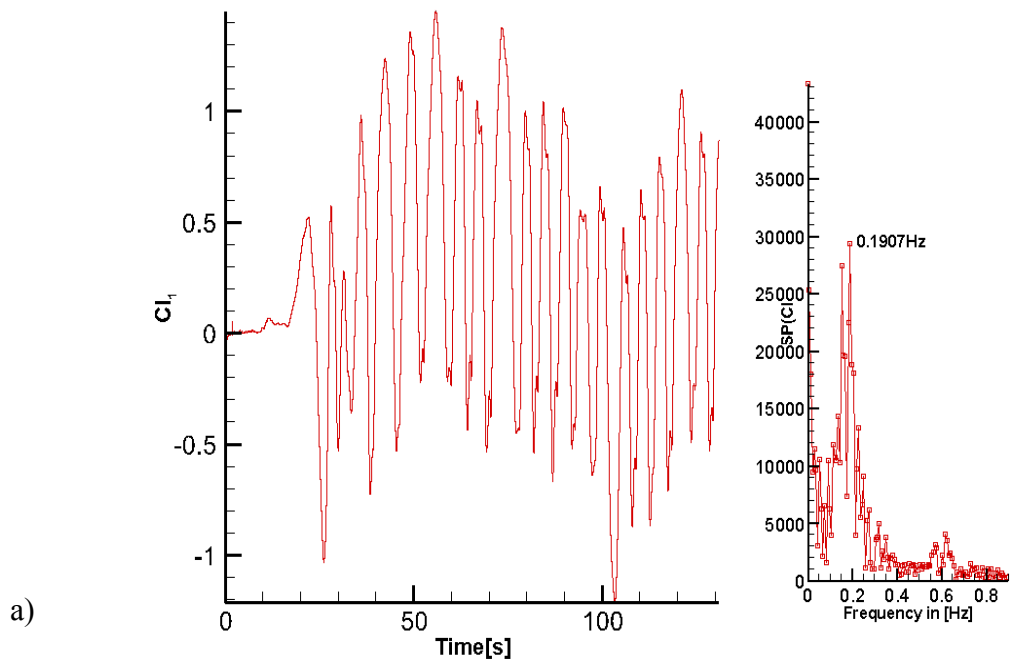


Figure 18. a) Instantaneous streamlines and b) instantaneous vorticity contours for flow past inline cylinders at $Re = 1000$.



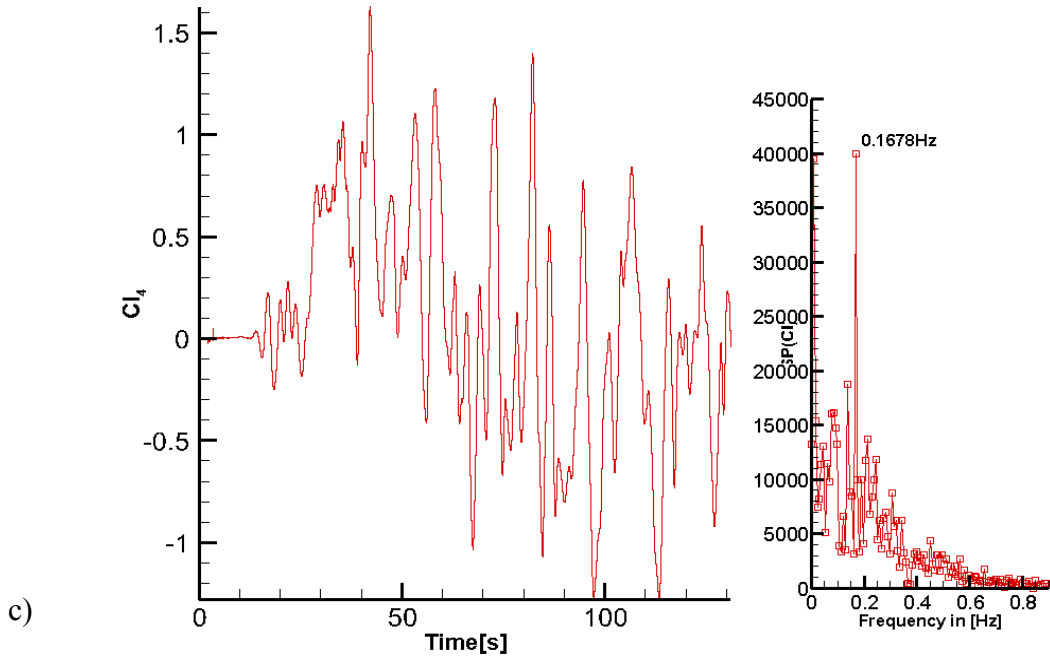
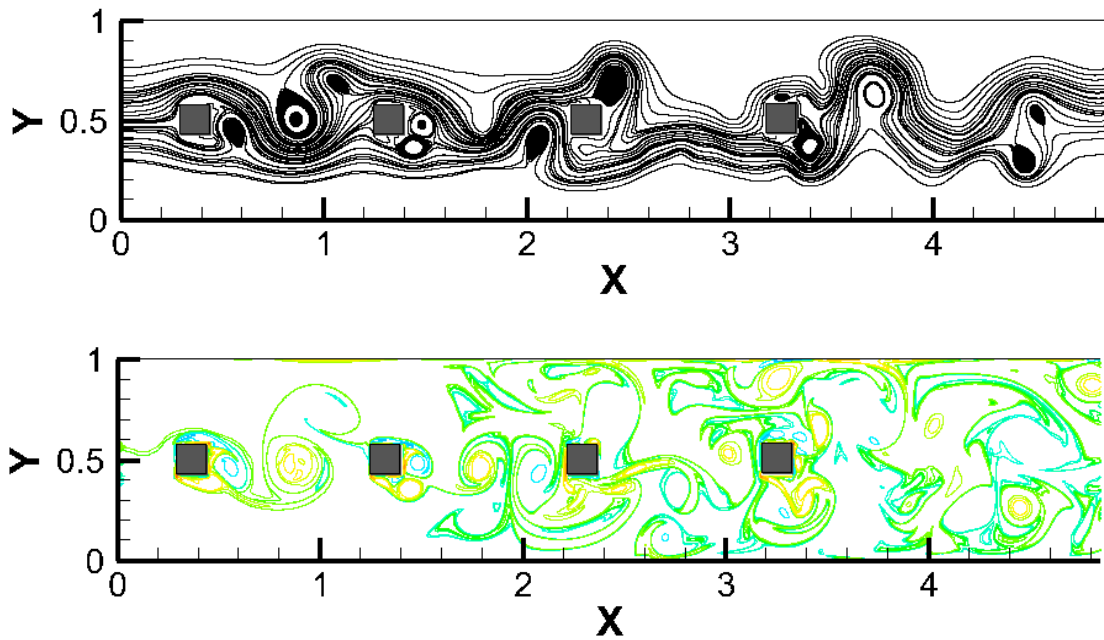
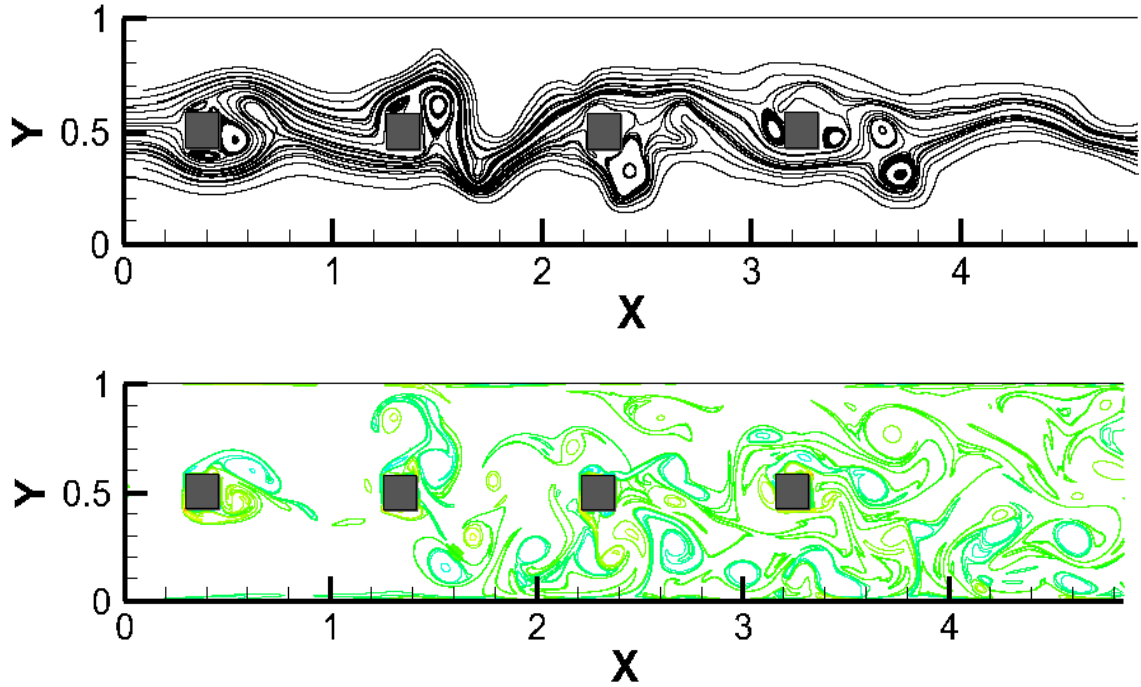


Figure 19. The lift coefficient vs time and the Fast Fourier Transform of the lift coefficient. The lift coefficient is calculated a) 1st cylinder, b) 3rd cylinder, and c) 4th cylinder at $Re = 1000$.



a) Inline $Re = 10000$



b) Inline $Re = 20000$

Figure 20. Instantaneous streamlines and vorticity contours for flow past inline cylinders at a) $Re = 10000$ and b) $Re = 20000$.

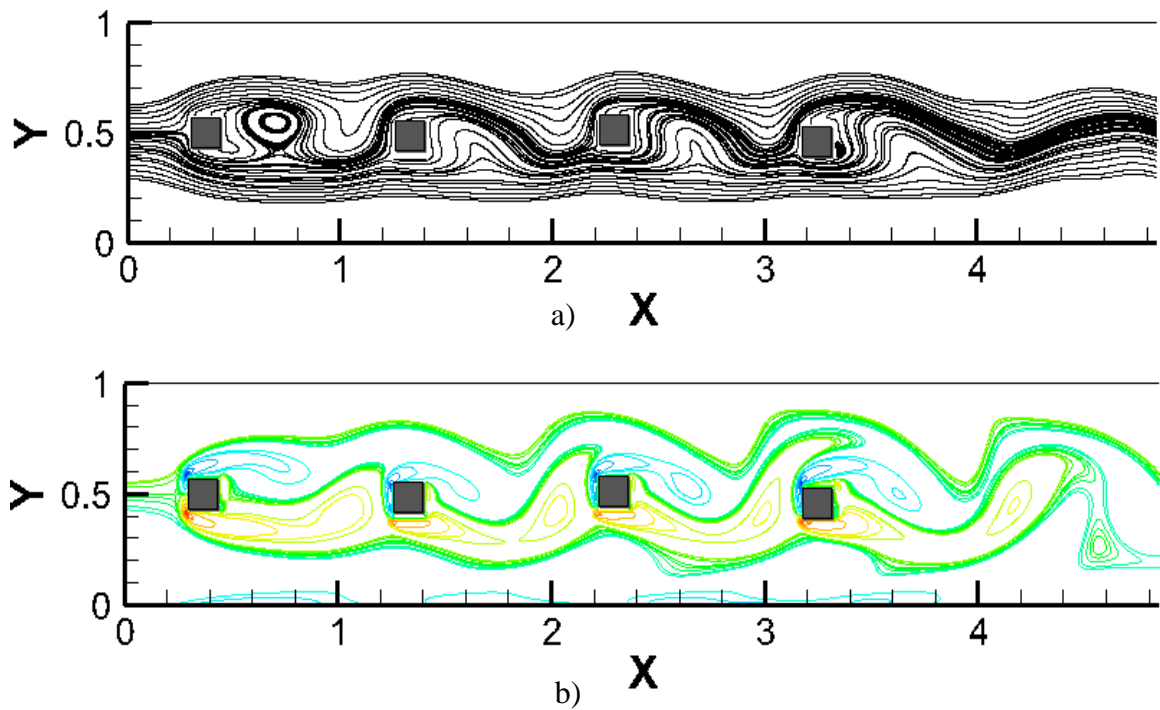
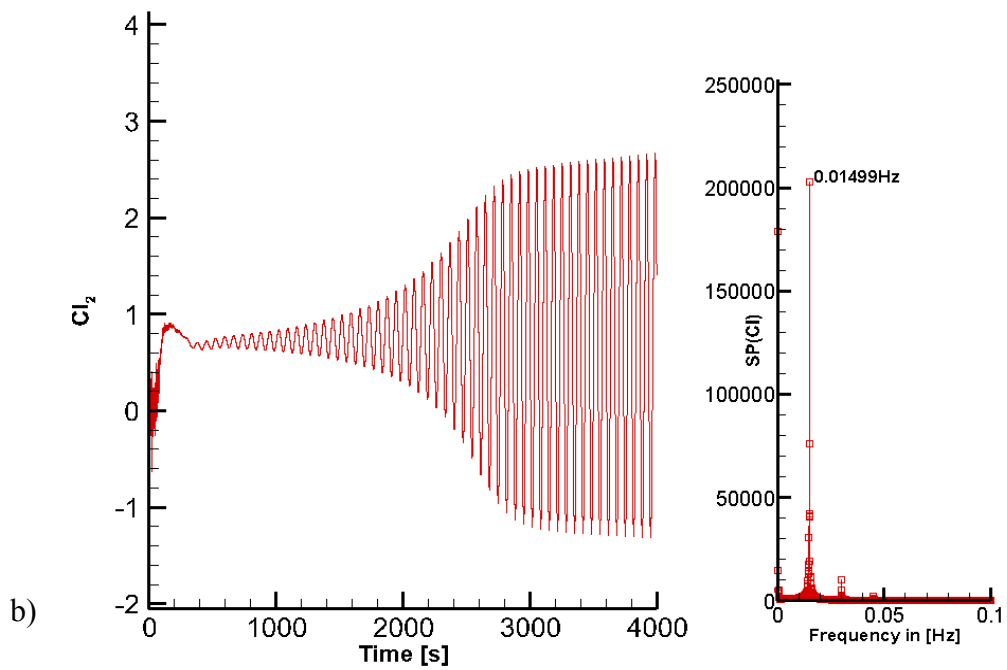
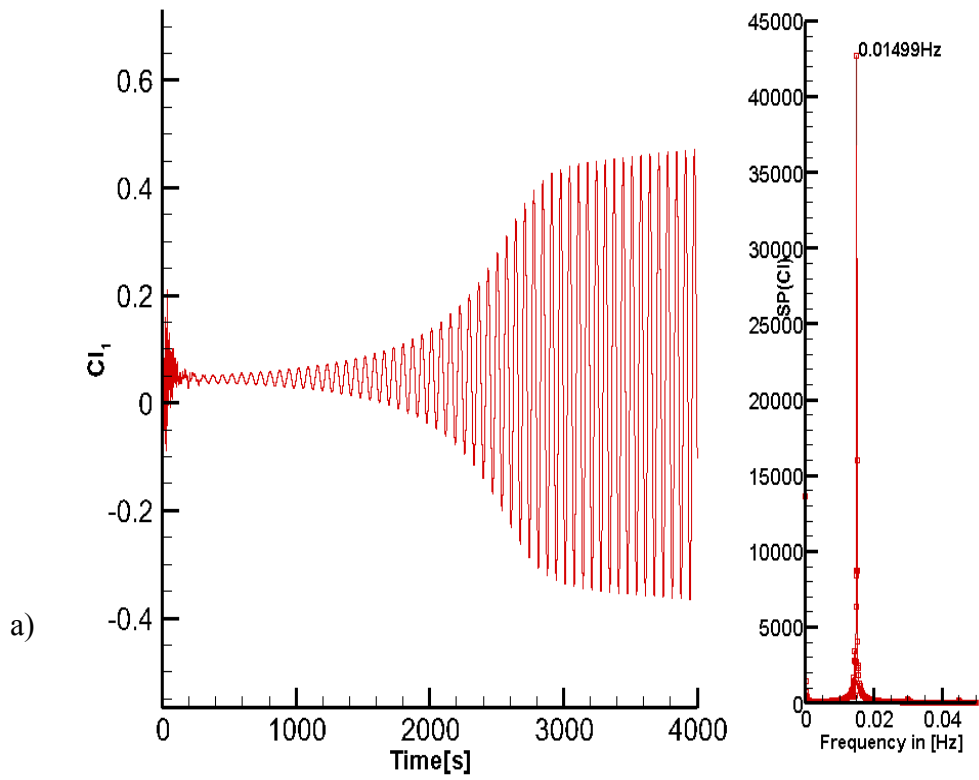


Figure 21. a) Instantaneous streamlines contour and b) instantaneous vorticity contours for flow past staggered cylinders at $Re = 50$.



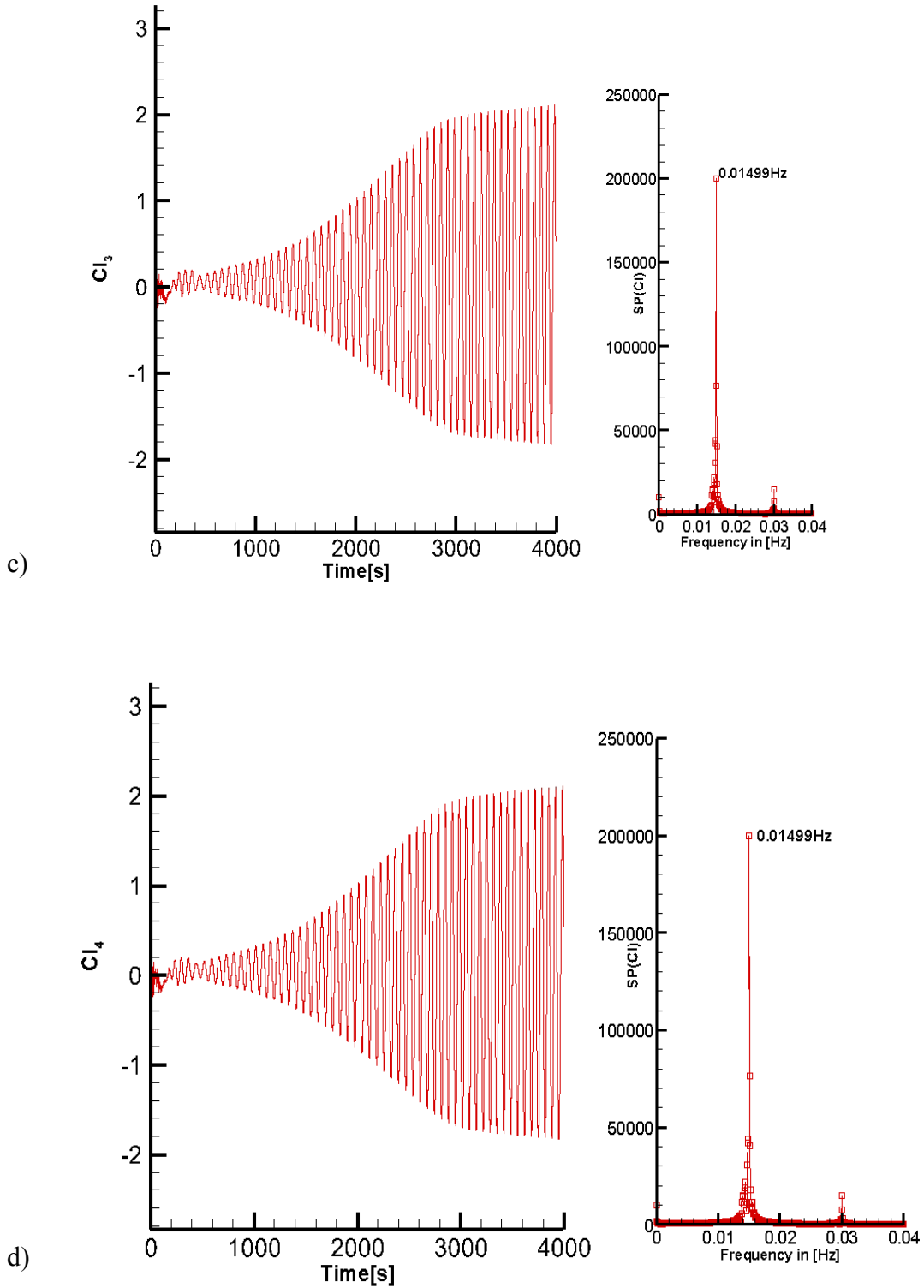


Figure 22. The lift coefficient vs time and the Fast Fourier Transform of the lift coefficient. The lift coefficient is calculated a) 1st cylinder, b) 2rd cylinder, c) 3rd cylinder, and d) 4th cylinder at $Re = 50$.

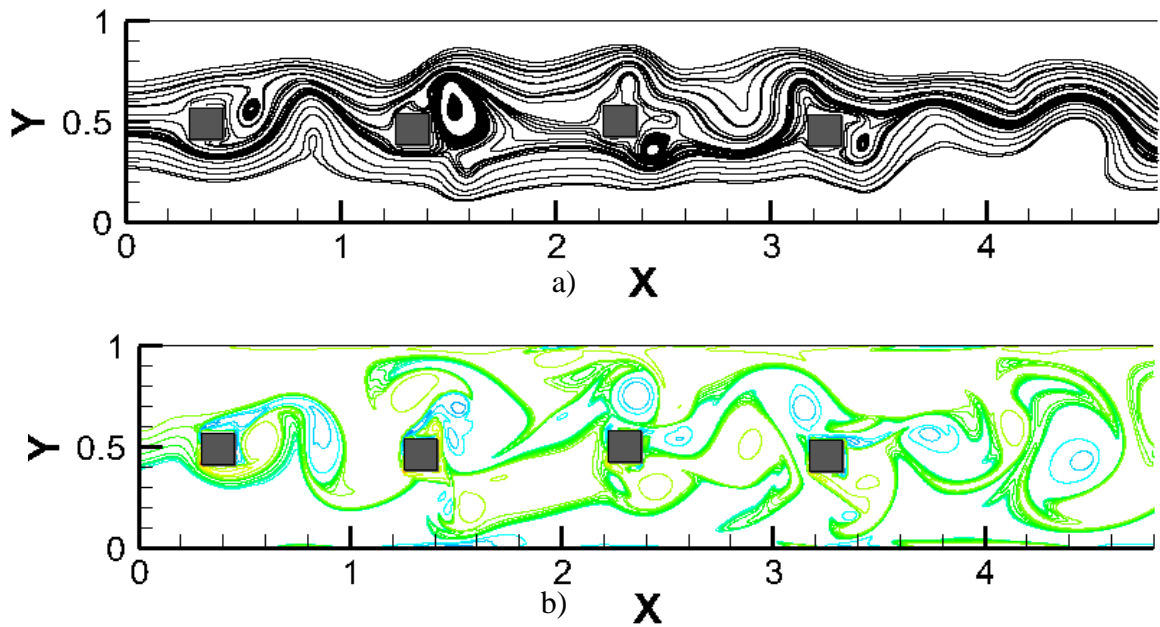
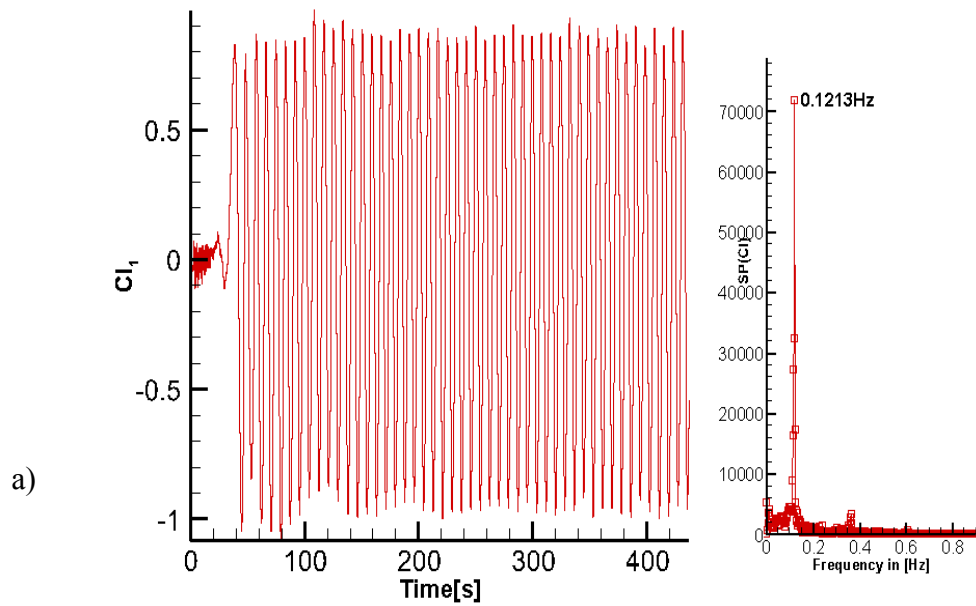
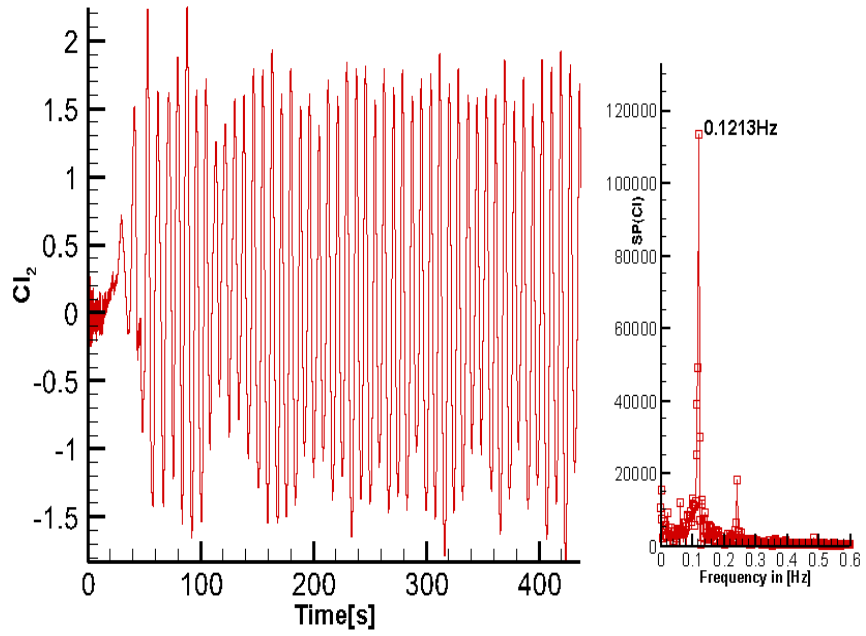
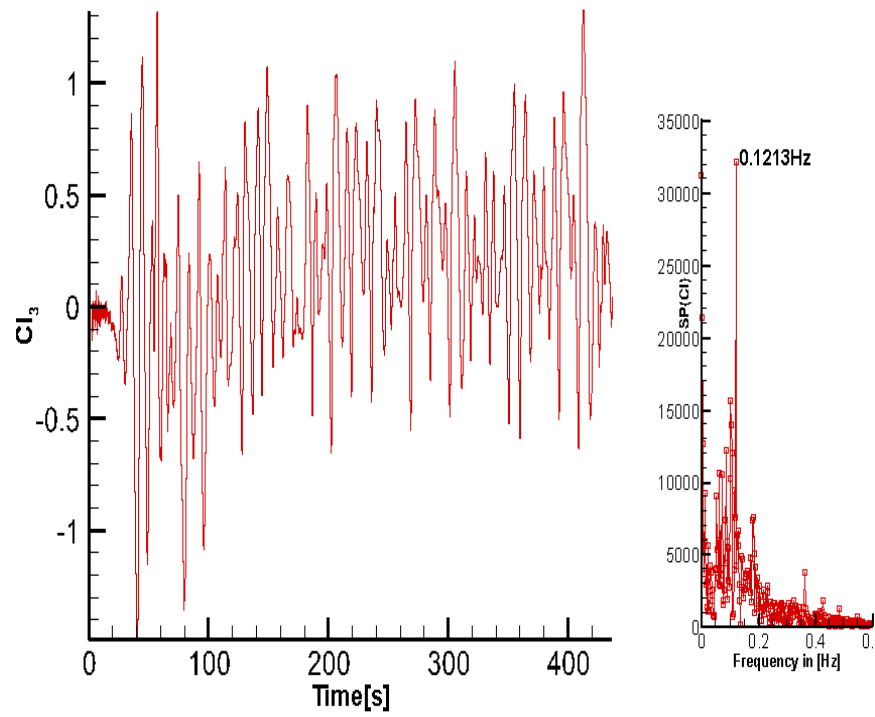


Figure 23. a) Instantaneous streamlines contour and b) instantaneous vorticity contours for flow past staggered cylinders at $Re = 500$.





b)



c)

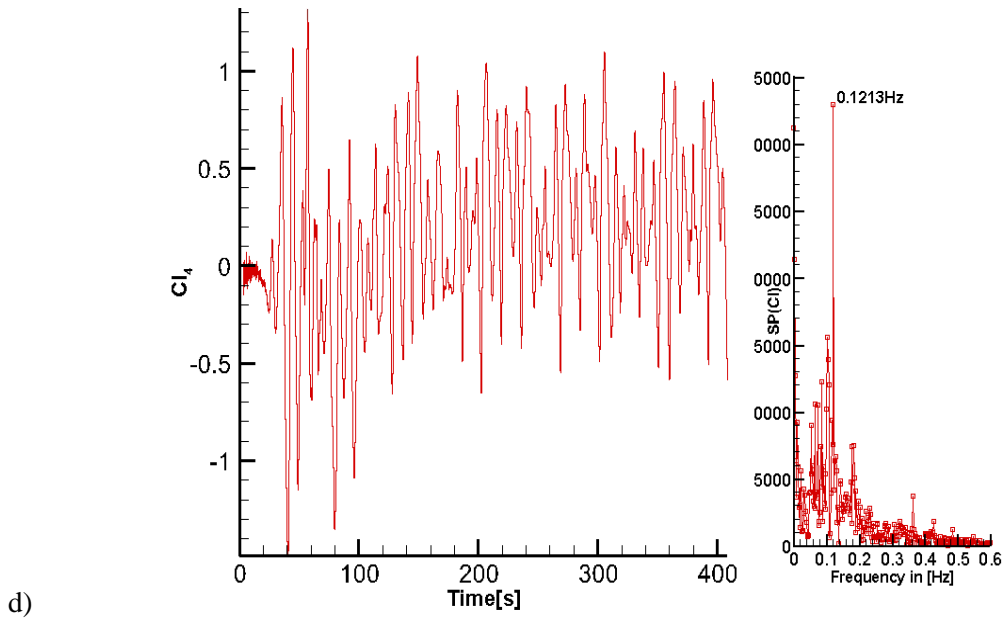


Figure 24. The lift coefficient vs time and the Fast Fourier Transform of the lift coefficient. The lift coefficient is calculated a) 1st cylinder, b) 2rd cylinder, c) 3rd cylinder, and d) 4th cylinder at $Re = 500$.

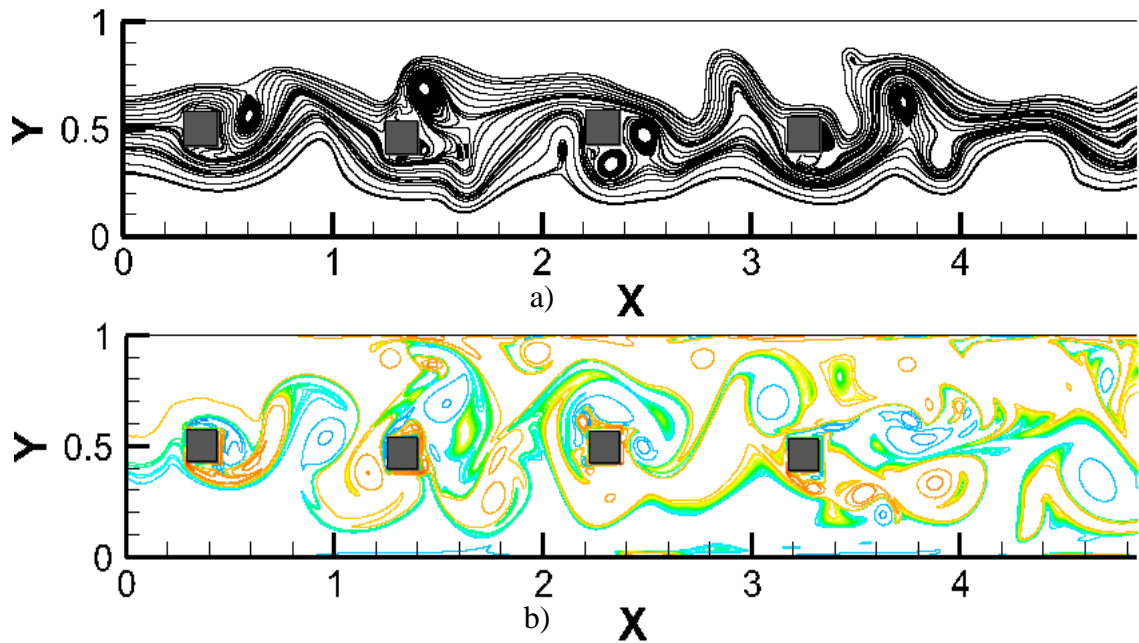
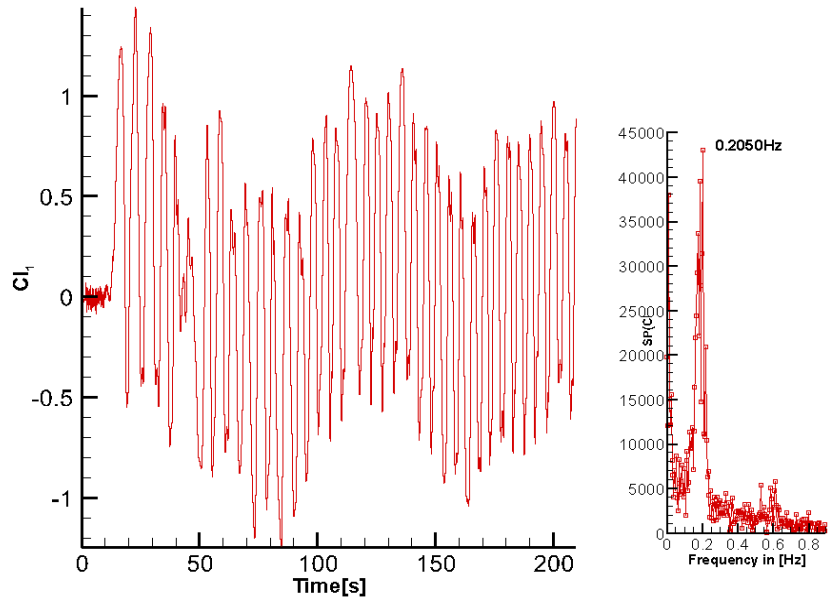
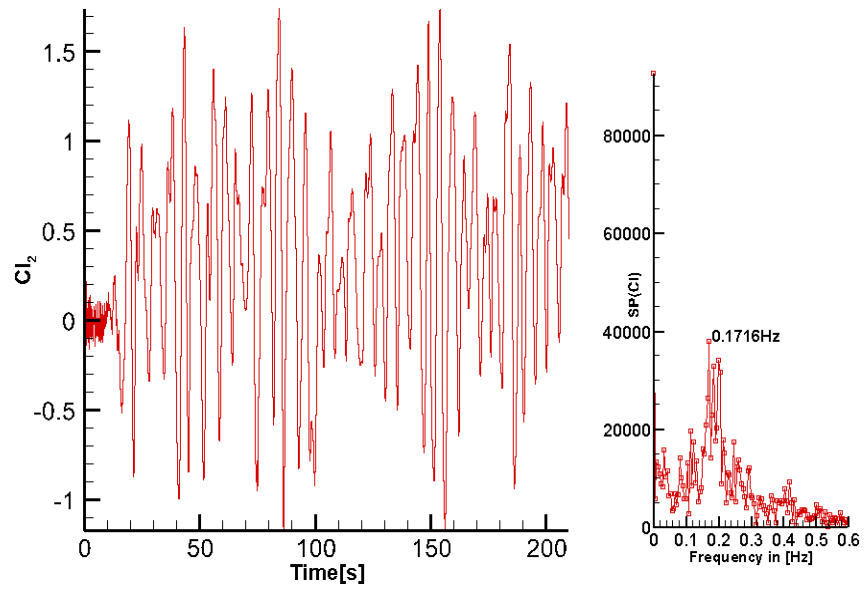


Figure 25. a) Instantaneous streamlines contour and b) instantaneous vorticity contours for flow past staggered cylinders at $Re = 1000$.



a)



b)

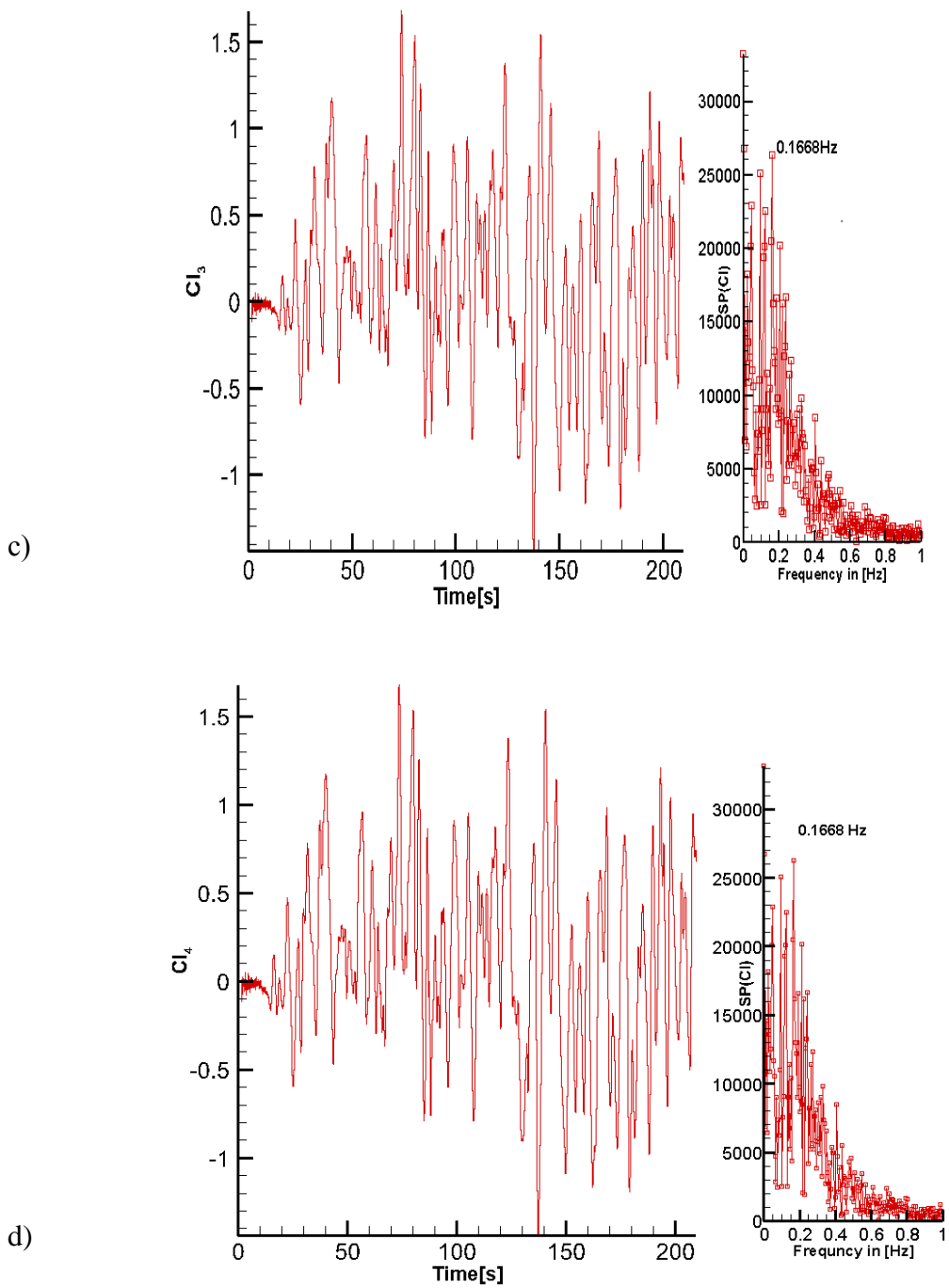
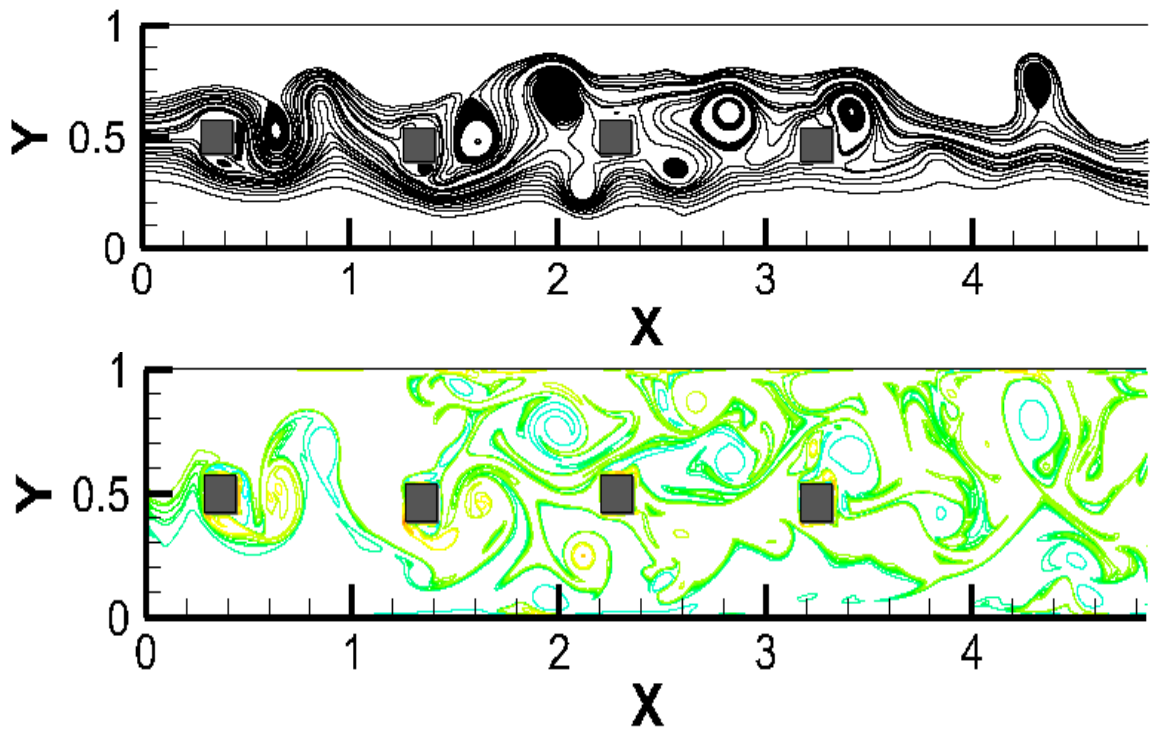
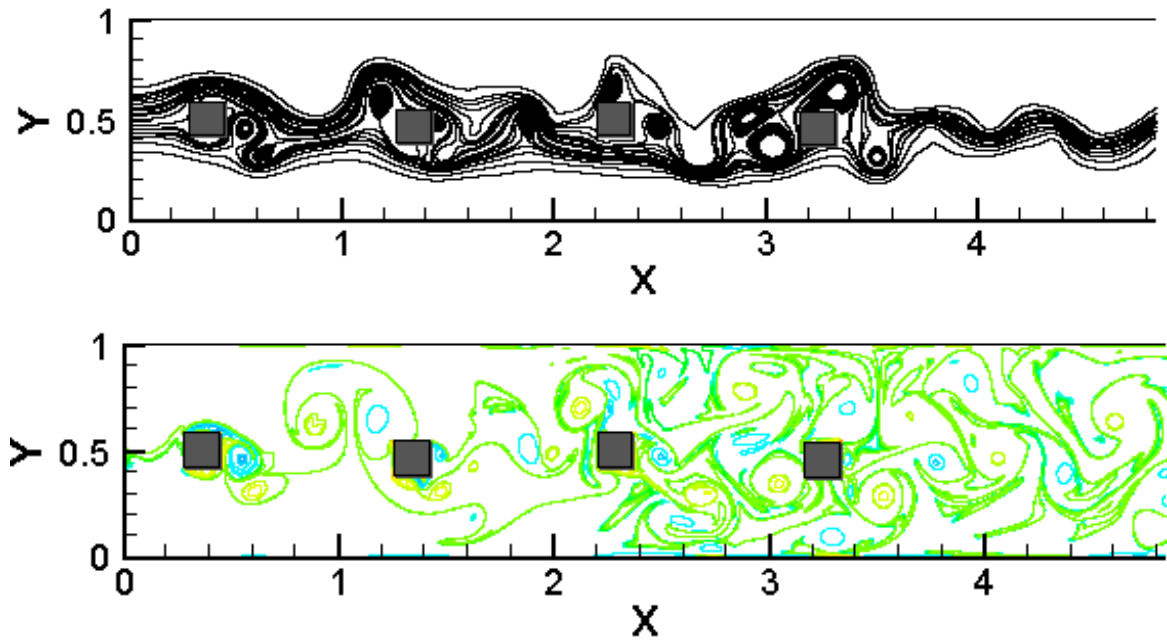


Figure 26. The lift coefficient vs time and the Fast Fourier Transform of the lift coefficient. The lift coefficient is calculated a) 1st cylinder, b) 3rd cylinder, c) 3rd cylinder, and d) 4th cylinder at $Re = 1000$.



a) $Re = 10000$



b) $Re = 20000$

Figure 27. Instantaneous streamlines and vorticity contours for flow past staggered cylinders at a) $Re = 10000$ and b) $Re = 20000$.

As mentioned above the vortex shedding frequency is determined from the lift coefficient by applying the Fast Fourier Transform. The Strouhal number is plotted as a function of the Reynolds number for the single cylinder geometry in Figure 28. The Strouhal number increases rapidly for low Reynolds number until it reaches its maximum value near the Reynolds number of 250. Beyond the Reynolds number of 1000 the Strouhal number decreases slowly. The frequency of the vortex shedding predicted by the lattice Boltzmann model is compared with the experimental results reported by R.W. Davis et al. [36]. Since the results match the experimental results very well, the present model is validated. Streamline and vorticity contours are depicted in Figures 13-27 for the inline and the staggered geometry. The streamlines in the inline geometry are very different to those in the single cylinder geometry. Turbulence eddies induced by the first cylinder effects the flow past the following cylinders. It is also noted that the influence of the boundary on the flow structure is enhanced in the inline geometry. These effects are more pronounced in the staggered geometry, as shown in Figures 21-27.

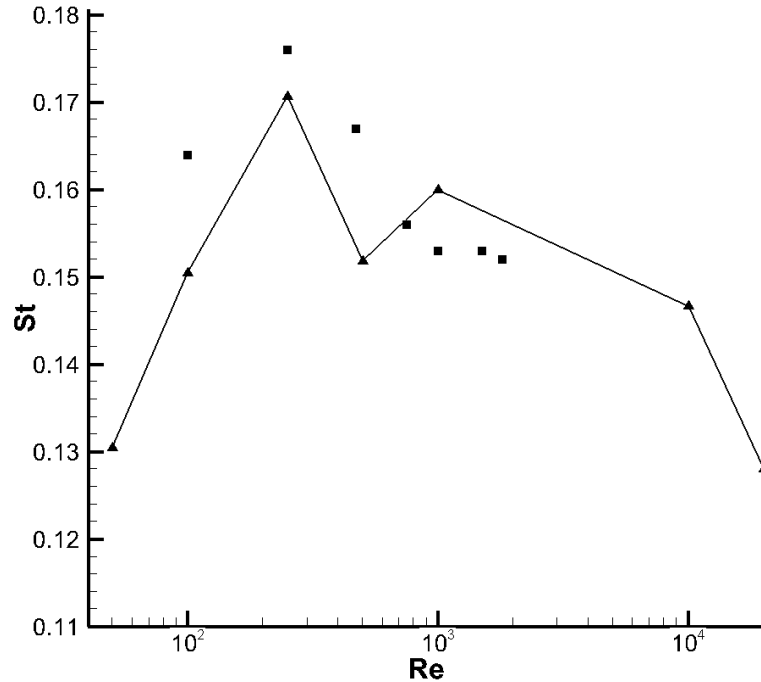


Figure 28. Strouhal number as a function of the Reynolds number for a single cylinder geometry. Line connecting triangles denotes prediction and the squares denote the experimental measurement by Davis et al. [36].

The power spectrum calculated for the first cylinder of the staggered array at $Re = 20000$. It is found that the frequency of the vortex shedding even from the first cylinder in both inline and staggered geometries shows several peak frequencies, as shown in Figure 29. This behavior is similar for the other cylinders in the array. This indicates that the vortex shedding phenomena occurring from arrays of cylinders at this high Reynolds number have a disrupted temporal nature.

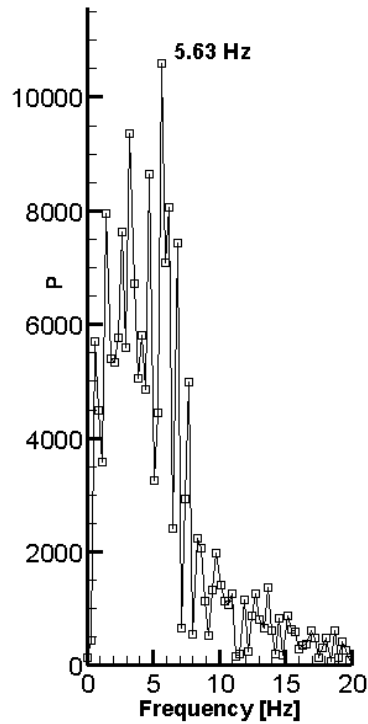
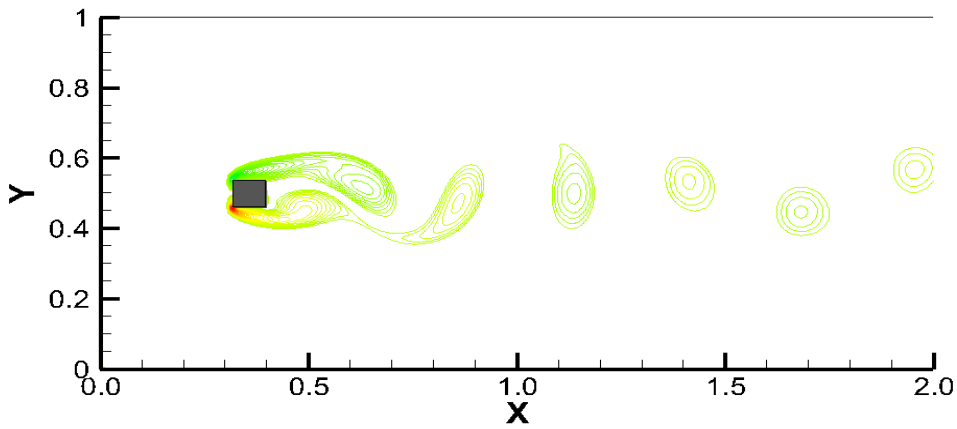
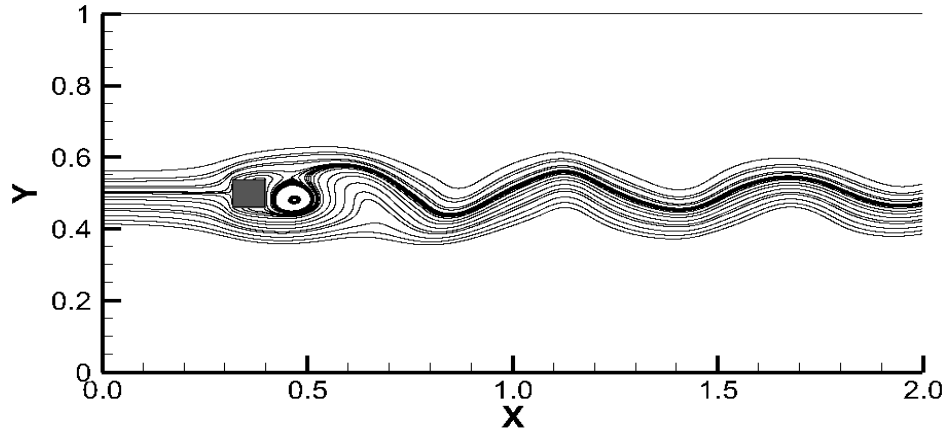


Figure 29. Power spectrum of the lift coefficient in the flow past an array of staggered cylinders.

Figure 30 shows the instantaneous streamlines, iso-vorticity lines and the power spectrum of the lift coefficient for the flow past a square cylinder with the blockage ratio of 1/14 at $Re = 21400$. Streamlines and vorticity field in the wake of the cylinder are very similar to those observed by Lyn et al. [37, 38] and those predicted by large eddy simulations and Reynolds-stress averaging [39-40]. The vortices shed by the upper corner of the cylinder shift slightly upward while the vortices shed by the lower corner shifts slightly downward from the centerline. For the computational domain selected here the vortices does not interact with the boundaries. This is unlike for flows past a cylinder with the blockage ratio of 1/6. As mentioned above the vortices interact strongly with the boundary away from the boundary when the blockage ratio is larger. This interaction occurs even for Re as low as 1000, as shown in Figure 10b.



a) Instantaneous streamlines and the vorticity contours.

b) Power spectrum of the lift coefficient at $Re = 21400$.

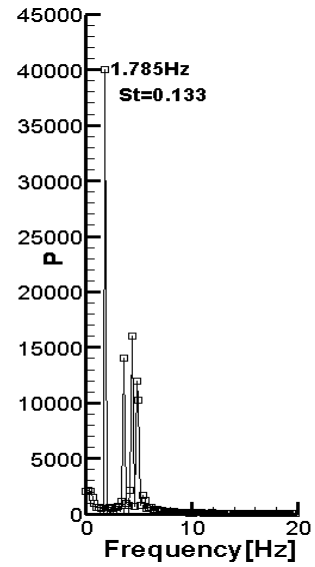


Figure 30. a) Instantaneous streamlines and the vorticity contours and b) power spectrum of the lift coefficient. Flow field is presented for the single cylinder geometry at $Re = 21400$ for $BR = 1/14$.

The frequency of the vortex shedding predicted here is $St = 0.133$ (see Figure 30b) which agrees well with those measured [36,39] and predicted by large eddy [39,41] and Reynolds-stress averaging (RSE) [40], as shown in the Table 1.6

PresentLBM [16]		Exps [36,42]	LES [41]	LES [39]	LES [38]	RSE[40]
St	0.133	0.132	0.132	0.134	0.139	0.136

Table 1.6. Comparison Between the present results and previous results.

In summary, a novel regularized multi relaxation lattice Boltzmann model has been proposed to extend the stability boundary of the lattice Boltzmann model for high speed turbulent flows. The new model has been successfully applied to turbulent flows past bluff bodies at high Reynolds number to resolve spatial and temporal characteristics of the flow in the wake. Unsteady turbulent flow around a square cylinder and arrays of square cylinders confined in a channel were studied computationally by employing regularized multi-relaxation lattice Boltzmann method. Spatial and temporal characteristics of the flow created by vortex shedding were examined for Re up to 21400. The frequency of the vortex shedding predicted here agrees well with the results measured and predicted by large eddy simulations for a wide range of Reynolds number. This study clearly demonstrates that the lattice Boltzmann method developed here improves the stability challenge of the lattice Boltzmann method for high Reynolds flows. One of the advantages of the method developed here is that computation time is an order of magnitude lower when it is compared with large eddy simulations or direct numerical simulations.

CHAPTER 4: RAYLEIGH BENARD CONVECTION

4.0. Objective

The aim of this study is to develop a stable thermal lattice Boltzmann model to study the buoyancy driven convection. The multi-relaxation thermal lattice Boltzmann model is introduced. The equilibrium equation in the collision term is derived to solve the energy equation. Thus, the thermal lattice Boltzmann model has been developed to study flows induced by the density stratifications by employing the Boussinesq approximation. Two geometries with different aspect ratios are considered using D2Q9 lattice arrangements. The results are compared against those obtained by R. Allen and T. Reis [43]. The results agree well with those obtained by the empirical correlation as well. It is shown here that the lattice Boltzmann method can be applied for flows with the presence of the temperature gradient by selecting the appropriate local equilibrium distribution function.

4.1. Introduction

Thermal lattice Boltzmann method has been developed. The method has been tested on two dimensional natural convection problem in a rectangular cavity. Two geometries with different aspect ratios and thermal boundary conditions are considered. One is a square box (aspect ratio of one) with top and bottom boundaries are insulated. The side boundaries are kept at different constant temperatures, as shown in Figure 31. The other geometry is a rectangular box with aspect ratio of 5, as shown in Figure 32. For the latter geometry the temperature of the bottom boundary is greater than the top boundary. When the Rayleigh number exceeds the critical value for the onset of convection, the fluid motion will onset. The fluid motion is a result of the density stratification. The buoyancy driven convection is well known as Rayleigh- Benard convection. The thermal lattice Boltzmann method is

tested by examining the flow pattern of the Rayleigh-Benard at various values of the Rayleigh number. The mathematical model for the thermal lattice Boltzmann method is summarized below.

4.2. A Mathematical Model

The lattice Boltzmann equation is

$$\frac{\partial f_k}{\partial t} + c_k \cdot \nabla f_k = \omega(f_k^{eq} - f_k) + \frac{W_1 C_k \cdot F_k}{C_s^2} \quad 86$$

The distribution function of the thermal model is defined as

$$\frac{\partial g_k}{\partial t} + c_k \cdot \nabla g_k = \omega(g_k^{eq} - g_k) \quad 87$$

where the local equilibrium distribution for temperature is

$$g_k^{eq} = w_k \theta \left\{ 1 + \left(3 \frac{\mathbf{e}_k \cdot \mathbf{u}}{c^2} + \frac{9}{2} \frac{(\mathbf{e}_k \cdot \mathbf{u})^2}{c^4} - \frac{3}{2} \frac{|\mathbf{u}|^2}{c^2} \right) \right\} \quad 88$$

The equation (87) satisfies the conservation of mass, the momentum and the energy with following constraints

$$\rho = \sum_{k=0}^Q f_k \quad 89$$

$$\theta = \sum_{k=0}^Q g_k \quad 90$$

$$\rho \mathbf{u} = \sum_{k=0}^Q f_k \cdot \mathbf{e}_k \quad 91$$

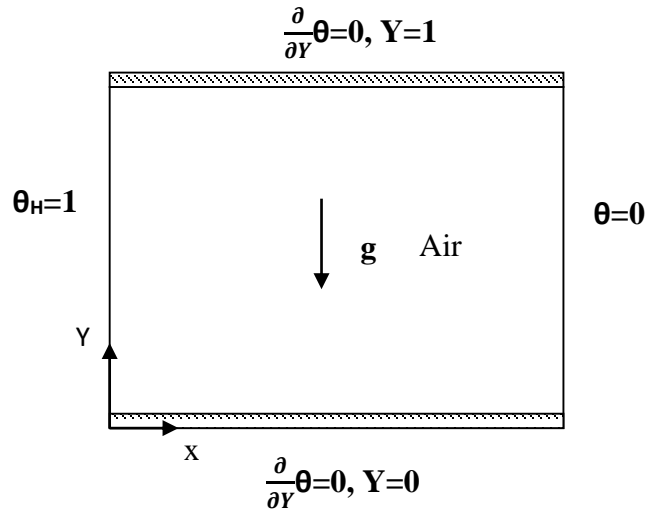


Figure 31. Schematic diagram of natural convection cavity for AR=1.

where F is the gravitational force or the body force and it can be evaluated from the Boussinesq approximation as

$$F_k = \rho g_y \beta (\theta - \theta_{ref}) \quad 92$$

where the normalized reference temperature is defined as

$$\theta_{ref} = \frac{\theta_H - \theta_c}{2} \quad 93$$

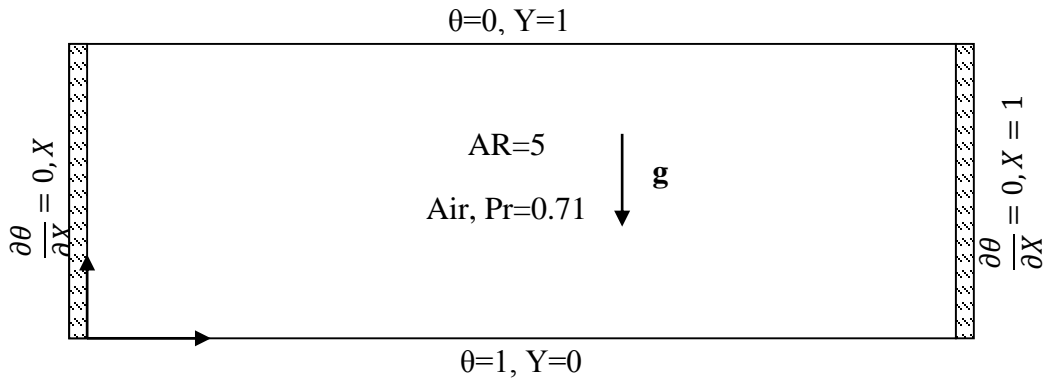


Figure 32. Schematic diagram of a Rayleigh Benard problem with AR=5.

The momentum and energy equations are coupled in these problems and solved simultaneously.

4.3. Results and Discussions

The MRT lattice Boltzmann model has been employed to study the natural convection in a square cavity. Simulations are conducted for various values of the Rayleigh number. The Nusselt number is calculated and compared with those reported in the open literature [43]. The results are well agreement with those obtained in literature, as shown in Table 1.6. The D2Q9 arrangements is used and the no-slip and no-penetration conditions are imposed on the velocity field. The boundary conditions are treated as described in section 2.10.

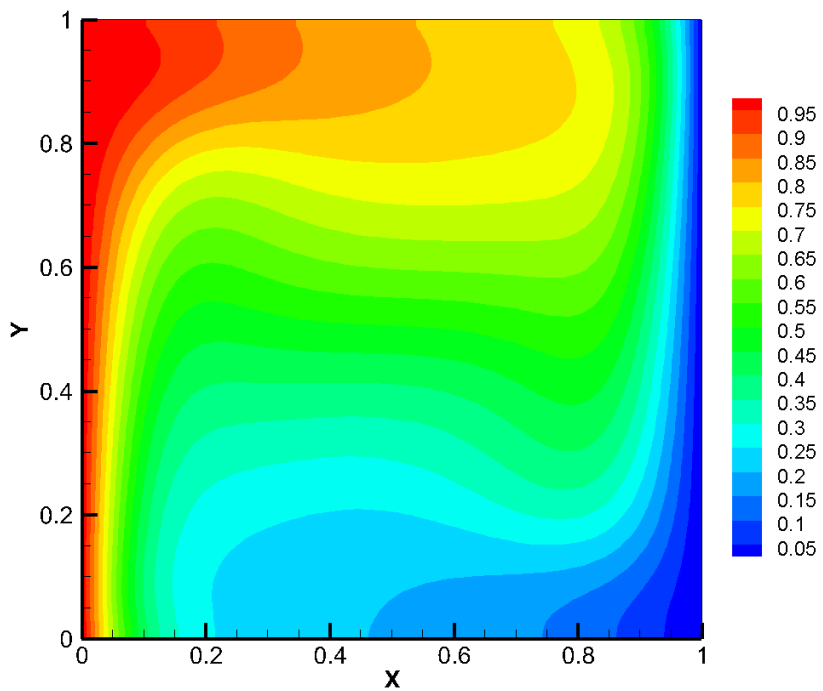


Figure 33. Isotherms at $Ra = 1 \times 10^5$ in a square cavity.

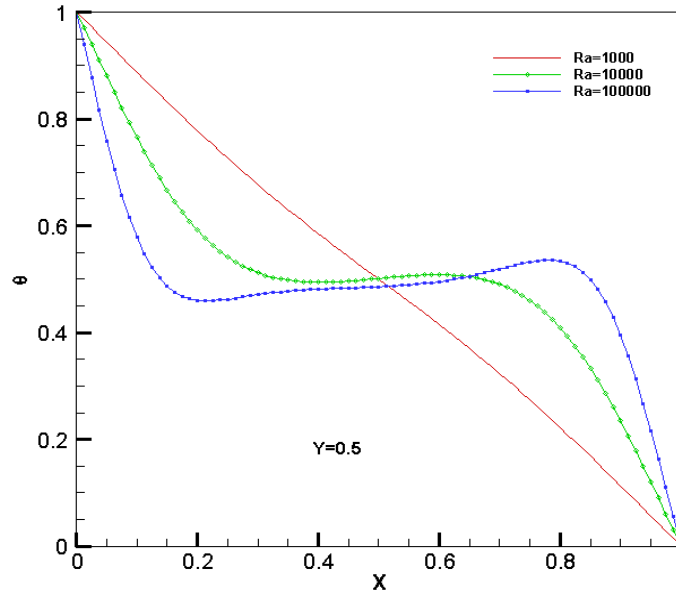


Figure 34. Temperature profiles at various values of the Rayleigh number in a square cavity.

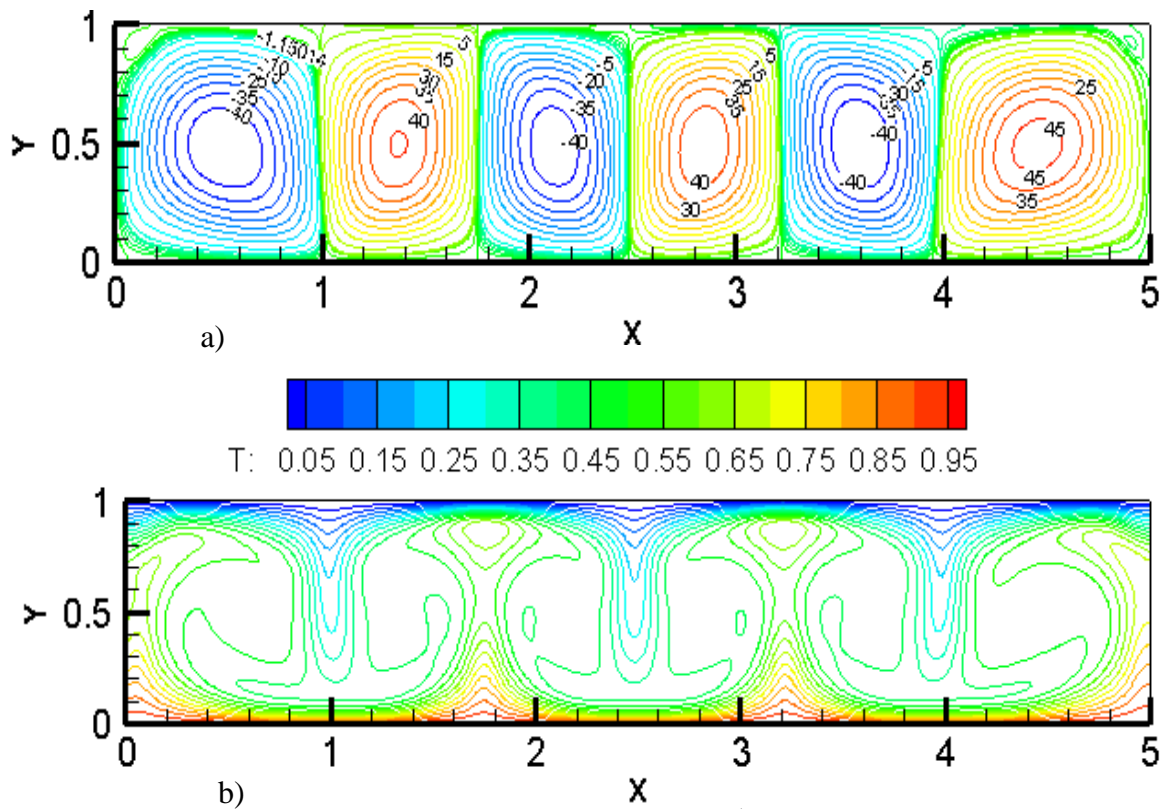


Figure 35. a) Streamlines and b) isotherms at $Ra = 1 \times 10^5$ in a cavity with $AR=5$.

When the warmer fluid (lighter fluid) is at the bottom and the cooler fluid (heavier fluid) is at the top, the density stratification is unstable. In such situation natural convection will be set when the Rayleigh number exceeds the critical value. The Rayleigh number is defined by

$$Ra = \frac{g\beta\Delta TH^3}{\nu\alpha} \quad 94$$

The critical value of the Rayleigh number for the onset of convection in the configuration shown in Figure 32 is 1708. For $Ra > Ra_{crit}$, the dominant heat transfer in the system becomes convection. At such regime, the buoyancy-driven force becomes greater than the viscous force. That results in a fluid motion. As the Rayleigh number is increased the intensity of the fluid motion becomes greater. For very large values of the Rayleigh number, the flow induced by the density stratification becomes turbulent.

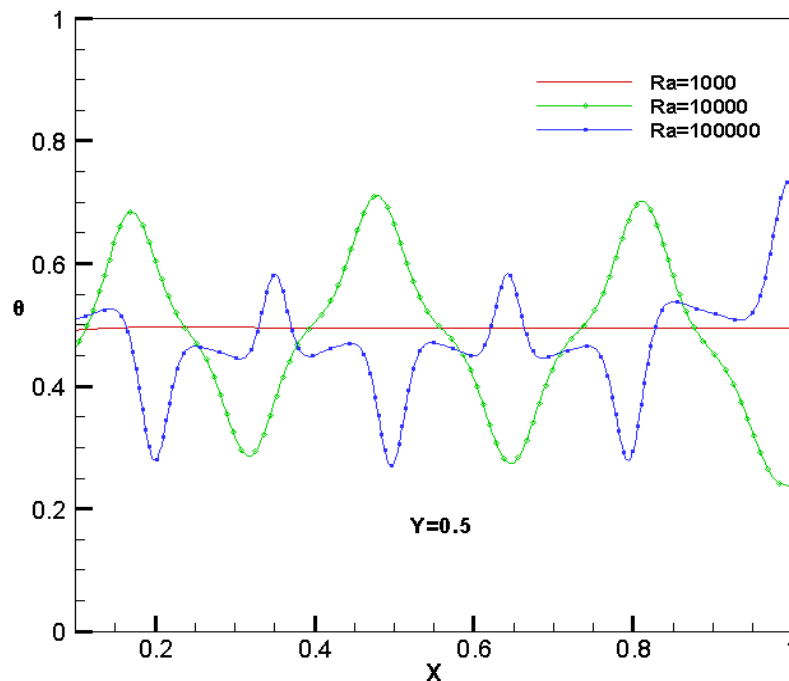


Figure 36. Temperature profiles plotted in the middle of the rectangular cavity for various values of the Rayleigh number.

In an unstable stratification, in which the lighter fluid is at the bottom, and the denser fluid is at the top, provided that the density gradient is sufficiently large, convection will start spontaneously and significant mixing of the fluid will occur. The temperature contour in Figure 35b illustrates the natural convection phenomena. If the temperature gradient is parallel to the direction of the gravitational acceleration in the absence of other effects, convection will be absent. Conduction is the only mode of heat transfer in this case. Uniformly spaced convection cells are seen in the streamlines as shown in Figure 33a for $Ra = 1 \times 10^5$. The convection cells are uniformly placed between the plates. They are nearly the same size. The cells adjacent to the wall are slightly distorted.

The temperature profiles in the middle of the rectangular cavity are plotted in Figure 36 for $Ra = 1000, 10000, \text{ and } 100000$. For $Ra < Ra_{crit}$ the temperature is uniform along the cavity. For $Ra > Ra_{crit}$ the temperature becomes periodic along the cavity. The periodic temperature profile is resulted from the buoyancy – driven convections.

Rayleigh Numbers	current study	pervious study [43]
$Ra=1 \times 10^3$	1.132107	1.11773
$Ra=1 \times 10^4$	2.271969	2.4466
$Ra=1 \times 10^5$	4.526193	4.52178

Table1.7. Comparison of the average Nusselt number for $Pr = 0.71$.

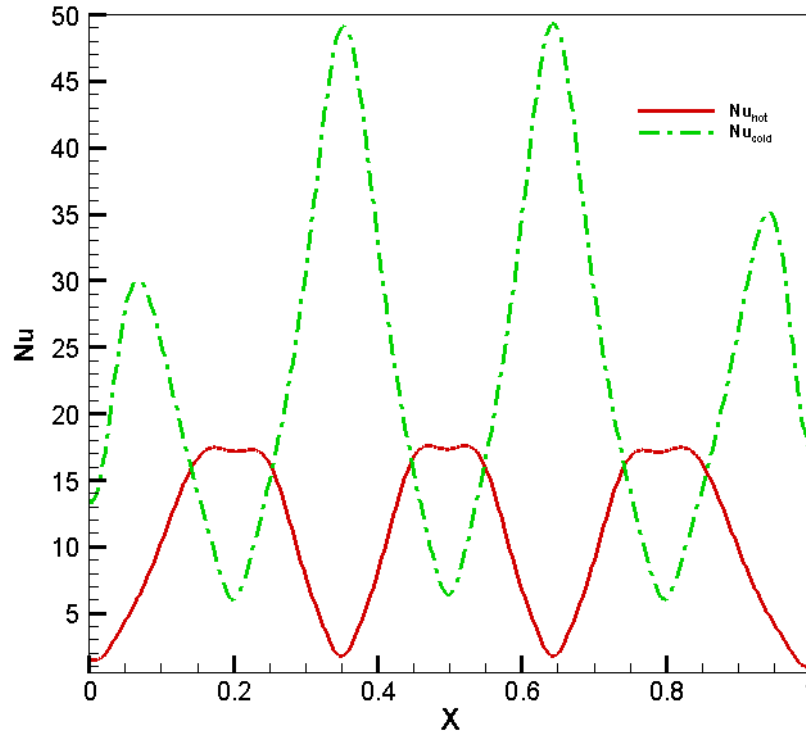


Figure 37. The Nusselt number at the top and the bottom wall at $Ra = 1 \times 10^5$ in the cavity with $AR=5$.

Figure 37 shows the average Nusselt numbers calculated by the thermal LBM. They agree with those obtained by the empirical correlation as

$$\overline{Nu} = 0.54 \times Ra^{0.25} \quad 95$$

Here $10^4 \leq Ra \leq 10^7$. For $Ra = 10^4$, the average \overline{Nu} is calculated to be 5.4 at the bottom wall.

For $Ra = 10^5$, the average \overline{Nu} is calculated to be 9.6 at the bottom wall. The average of Nusselt number for $Ra = 10^4$ and 10^5 predicted by the thermal lattice Boltzmann method is 5.6 and 9.78 at the bottom wall, respectively. If the Rayleigh number is less than 1708, the average Nusselt number equals 1 which means that no convection currents.

The Nusselt number is defined as

$$Nu_L = 2 \frac{(T_h - T_c) \partial \theta}{T_{ref} - T_c \partial Y} \quad 96$$

In summary, the multi-relaxation thermal lattice Boltzmann model has been developed to study a buoyancy-driven convections. Convection cells in a closure with a presence of no-slip surfaces were characterized. The results presented here agree well with those documented in the literature for flow patterns manifested by the Rayleigh-Benard instabilities.

CHAPTER 5: INTERFACIAL FLOWS

5.0. Objective

The objective of this study is to better understand the physical significance of the interaction forces proposed by Shan-Chen multi-phase flow model. Shan–Chen model has ability to simulate the multiple fluids by introducing non-local interactions between particles at each lattice site. The multi-relaxation time lattice Boltzmann collision operator with the Shan-Chen model was developed to obtain a better stability. Such level of stability is not achievable by using the original Shan-Chen model with a single relaxation time. The model can be utilized in cases where there is a need for the anisotropic dependency of the surface tension. It is believed that the surface tension has linked through the interactive strength. Such link is not established in the literature. One of the objective of the present study is to establish the relationship between the interactive force and the surface tension exerted at the interface between two immiscible fluids. The two and three Shan-Chen model dimensions with 9 and 19 directional velocities are applied. The droplet surface tension test is conducted to determine the strength of the surface tension in water and oil interface flows. The rising droplets dynamics and the Rayleigh Taylor instabilities in the bounded and the infinite domain are investigated. Our simulation results show that linear and nonlinear stages of the Rayleigh Taylor instability can be characterized successfully by using multi-phase lattice Boltzmann model. Further studies are needed to develop more stable multiphase lattice Boltzmann models to study the interfacial flows when larger density gradient is present.

5.1. Rising Droplets

5.1.1. Introduction

Several investigators studied droplet dynamics by using MRT–LBM for different configuration of droplets either in-line or staggered arrangements. Amit .G. and Kumar [44] studied the effect of the vortex shedding on the oscillatory motion of the bubbles and subsequent coalescence. Moreover, Amit and his co-workers recently studied the droplet breakup and they found that the droplets more viable for the case when the wall is non-wetting or neutral as compared to a wetting surface [45]. Droplet motions under electro-wetting control are investigated by using a finite volume method, with the focus on the effects of key control parameters on the induced droplet oscillation. They found that the electro-wetting enhanced the mixing within the droplet [46]. Droplets in the micro-fluidic has been studied as well by Hao [47]. Azwadi and Sidiket [48] employed a new variant of Shan-Chen multiphase model to compute the dynamics of droplet on non-permeable solid surface. Volume of fraction (VOF) was implemented to study the dynamics of drop impact and spreading on inclined surfaces. Different regimes of drop impact and spreading process were investigated by Siddhartha et al. [49]. Amaya and Lee determined the terminal shape and calculated the Reynolds number at different regimes and they found that the terminal shape and the Reynolds number are interactive quantities relying on the size of the bubble, the surface tension, the viscosity, and the density of the surrounding fluid [50]. Bozzano and Dente studied two aspects of the rising bubble. The first aspect is that the shape assumed by the rising bubble is the one minimizing the total energy associated with it. The second aspect is that is constituted by the approximated generalization of the drag coefficient [51].

In this section, our interest in these flows is to study temporal and spatial characteristics of the lighter fluid droplets as they rise through the heavier fluid. Nonlinear phenomena such as the effect of the boundary have been considered in the present study. The model utilized here to study liquid-liquid multiphase flow includes the interactive forces between fluids. The interactive force model proposed by Shan-Chen is related to the surface tension between two fluids considered here. Different arrangements of droplets have been studied for different boundary conditions. Both no-slip boundary conditions and periodic boundary conditions are considered. Simulation are conducted for a single droplet placed on the lower boundary, two droplets placed on top of each other's, two droplets placed side by side, and four droplets placed in the middle of the domain at the same distance from each other's, as shown in Figure 38.

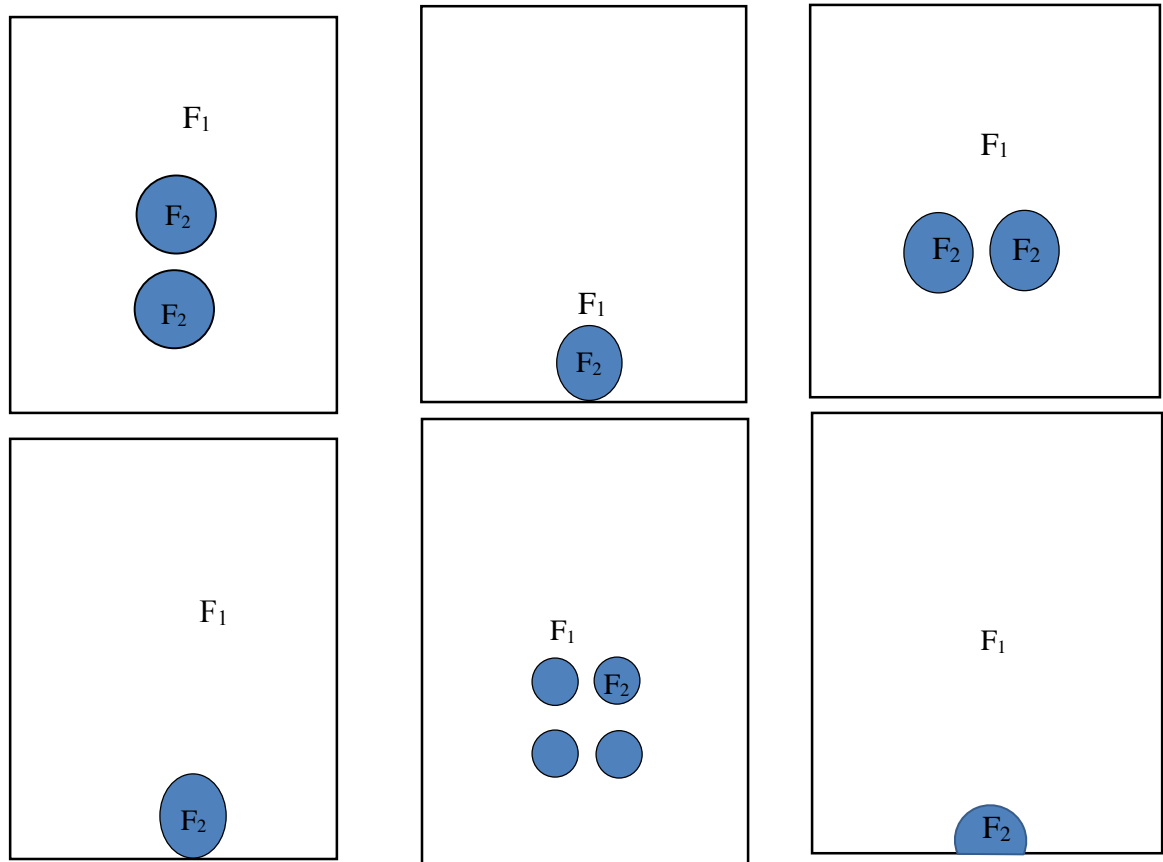


Figure 38. Various arrangements of droplets. F_2 denotes the droplet of lighter fluid while F_1 denotes heavier surrounding fluid.

5.1.2. Validation Test

The result of the spectral and temporal convergence test is illustrated in Figure 45. The density contour for the single droplet at $t = 0.6$ s is shown for various grid sizes. The terminal shape of the droplet obtained for 100×400 , 125×500 , and 150×600 are shown in Figure 39. The results for grid size of 125×500 and 150×600 overlaps; indicating that the spatial and the temporal convergence can be attained for the grid size 125×500 and higher.

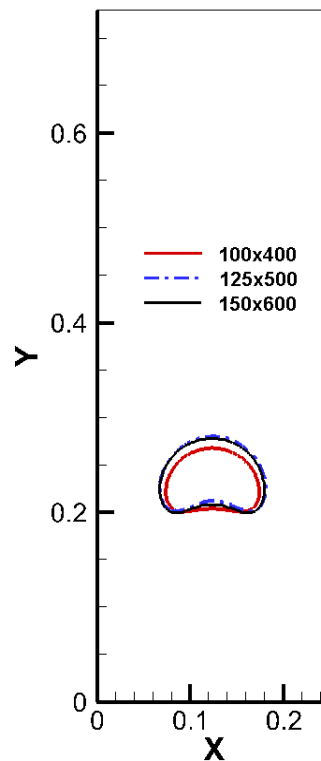


Figure 39. Grid optimization for the rising droplet. The shape of the droplet with different grid sizes is determined at $t = 0.60$ sec.

The surface tension can be estimated from Young-Laplace equation by simulating various size of the droplets and evaluate the slop of the pressure difference between inside and outside the droplet vs the inverse of the radius of the droplet, as shown in Figure 40.

$$\lambda = \Delta P \times r \quad [\text{Young} - \text{Laplace Equation}] \quad 97$$

$$\Delta P = \frac{\lambda}{r} = c_s^2 \Delta \rho - \frac{G}{6} (\Delta \psi(\rho))^2 \quad 98$$

where λ is the surface tension, r is the initial radius of the droplet, ΔP is the pressure difference between the inside and the outside of the droplet, and ψ is the potential density strength.

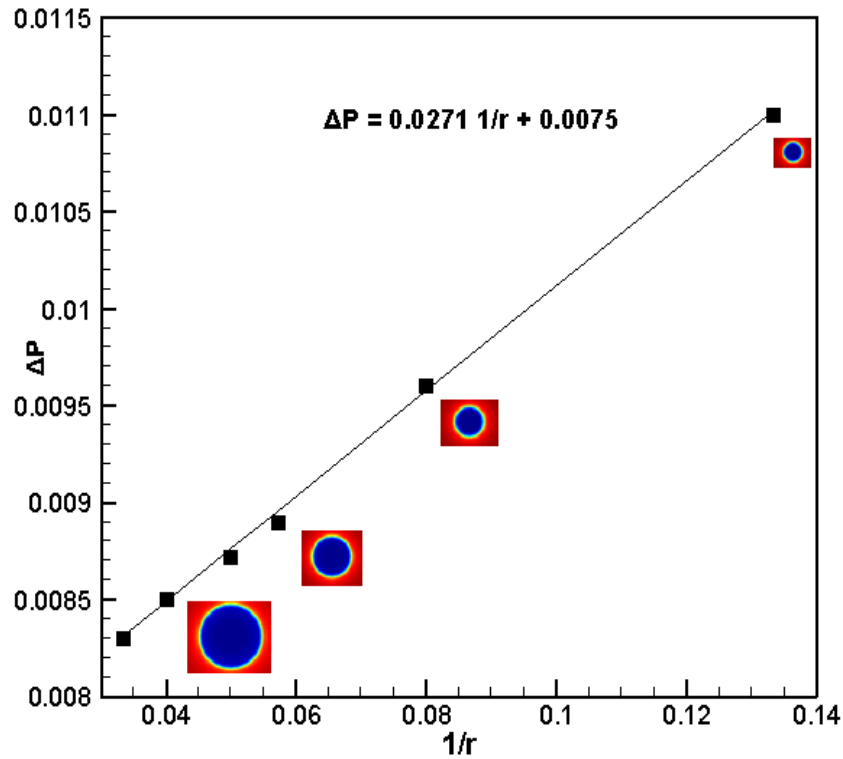


Figure 40. Pressure difference between the inside and the outside of the droplet vs $1/r$ for various droplet sizes for $G = 1.6$.

From the surface tension test, the surface tension is determined to be $\lambda = 0.0271$ by using Yang-Laplace equation. In the previous studies the surface tension is approximated as a function of the interactive strength [52]. The surface tension is an important to characterize the droplet dynamics. By using the value of the surface tension the Morton number, Weber

number, and Eötvös number can be calculated. These parameters will help characterizing the various droplets dynamics regimes.

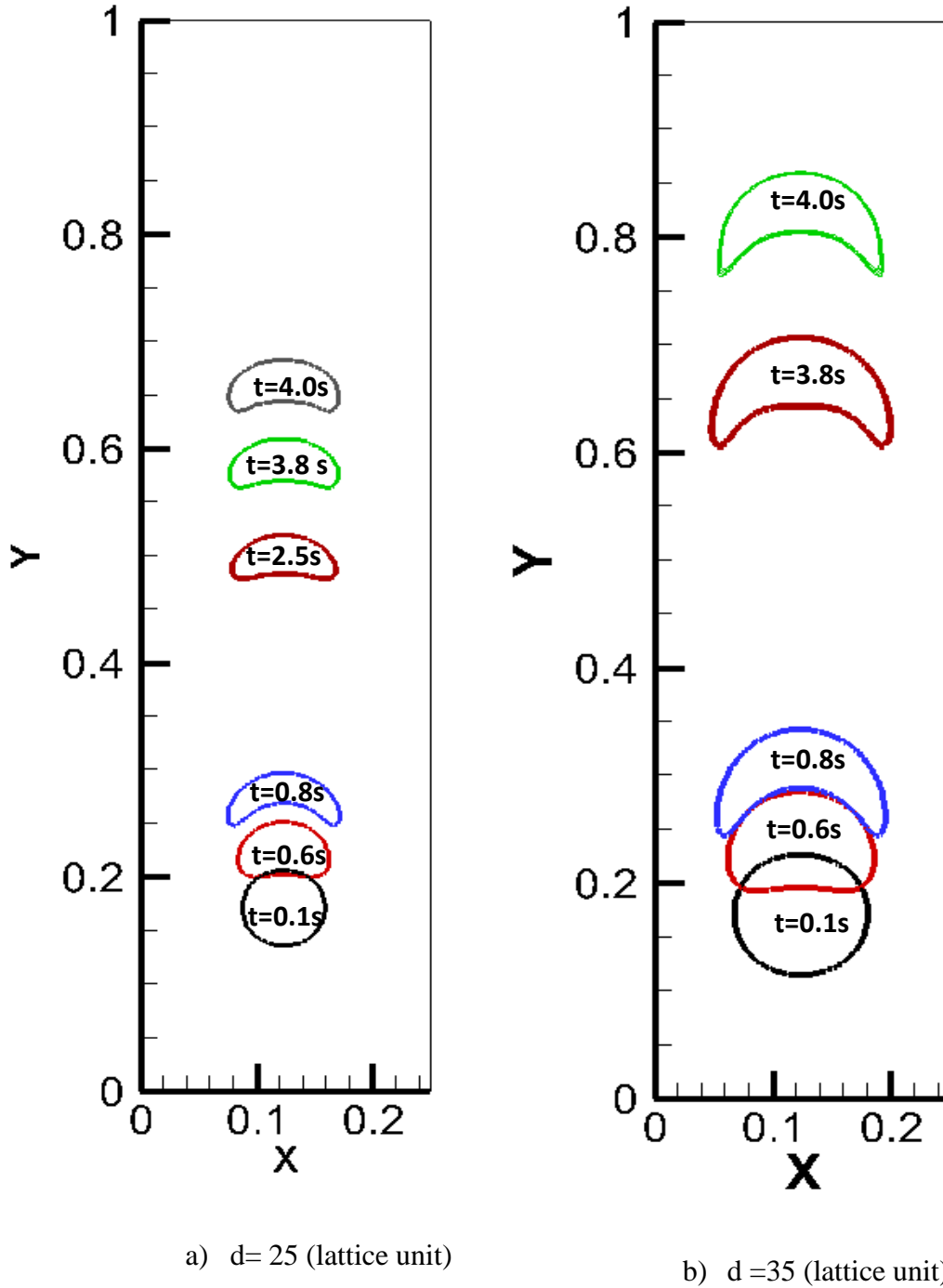


Figure 41. Density contours for different droplet sizes at various times for a single rising droplet in an infinite domain.

The droplet's dynamics is determined by the following dimensionless groups:

Reynolds number

$$Re = \frac{\rho U_t d}{\mu} \quad 99$$

Eötvös number

$$EO = \frac{\rho d^2 g}{\lambda} \quad 100$$

Morton number

$$MO = \frac{g \mu^4 \Delta \rho}{\rho^2 \lambda^5} \quad 101$$

Weber number

$$We = \rho U_t^2 d / \lambda \quad 102$$

Here U_t is the terminal speed of the droplet, which is determined as part of the solution, λ is the surface tension coefficients (determined to be 0.0271) and $\Delta \rho$ is the density difference between two fluids for oil droplets rising inside in the water $\Delta \rho = 0.2$. In order to validate the model employed by the present study, simulations for a single droplet rising in an infinite fluid are conducted for two different set cases. The Reynold number and Eötvös number are different for these two different cases. The evolution of the droplets of these two cases is shown in Figure 41. For the first case ($Re = 2.88$ and $EO = 17.8$) the oblate ellipsoid shape is attained as the terminal speed is reached. For the second case ($Re = 11.32$ and $EO = 54.4$) the spherical cap is predicted, as depicted in Figure 41. These two cases

are determined by the initial size of the droplet ($d = 25$ lattice unit for the first case and $d = 35$ lattice unit for the second case). The interactive forces are kept the same for both cases. The flow regime and the shape of the droplet agree well with those reported by Gupta et al. [44]. The terminal speed of the rising droplet will be attained as the drag force and the interactive forces exerted on the droplet are balanced [48]. Figure 42 shows the speed of the droplet for $Re = 11.32$ and $EO = 54.4$ as a function of the dimensionless time, $T = t(g/d)^{1/2}$. The terminal speed agrees very well with correlations documented earlier [53,54]. The rising velocity can be described by a theory proposed by Davis and Taylor [54]

$$U_t = \frac{2}{3} \sqrt{\frac{gd\Delta\rho}{2\rho_h}}, V = U_t \left[\frac{d^2 \rho_h^2}{\lambda \times v_h} \right]^{\frac{1}{3}} \quad 103$$

Where U_t is the terminal velocity and V is the velocity number. This simple correlation has been proposed by Rogdrigue [55] for the dynamic bubble rising in a pure viscous fluid. The terminal velocity is obtained as a function of density, surface tension, viscosity, and the geometry of a droplet. D. Roderigue calculated the analytical velocity number based on the shape of bubble [55] as

$$V = \frac{aF^b}{1 + cF^d}, a = \frac{1}{12}, b = 1, c = \frac{49}{1000}, d = \frac{3}{4} \quad 104$$

The flow number “FN” is defined as

$$FN = EO \left(\frac{Re}{C_a} \right)^{\frac{2}{3}} \quad 105$$

The hydrodynamic regimes for this correlation is covered for

$$1.9 \times 10^{-7} < Re < 1.9 \times 10^4, \quad 1.9 \times 10^{-11} < MO < 1 \times 10^7$$

Capillary number can be evaluated as

$$C_a = \frac{\mu U_t}{\lambda}$$

106

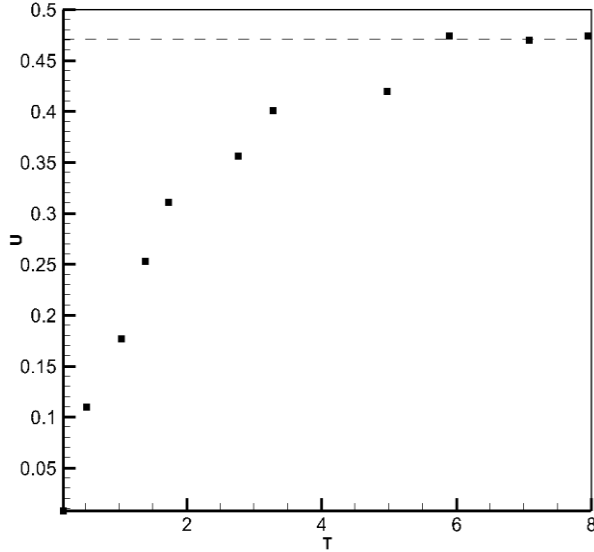


Figure 42. The droplet speed as a function of time. The terminal speed predicted by the LBM is compared against that obtain by Davis and Taylor. [54]

The droplet speed reaches the terminal velocity as the droplet speed doesn't change with time. As the terminal speed is reached the droplet shape is maintained. The terminal velocity plotted against those obtained by the correlation as [49, 50]

$$U_t = -\frac{8v}{3\sqrt{gD^3}} + \frac{\sqrt{2}}{3} \left[1 + \frac{32v^2}{gD^2} \right]^{\frac{1}{2}} \quad 107$$

U_t is dimensionless terminal velocity and the dimensionless time is $T = t \sqrt{\frac{g}{D}}$. Figure 42

shows the terminal speed predicted by the LBM agree well with that obtained by the correlation.

Cases	Reynolds Number	Eötvös Number (EO)
Oblate ellipsoid (d= 25 lattice unit)	2.88	17.18
Oblate ellipsoid Cap (d= 35 lattice unit)	11.3	54.43

Table1.8. The values of Re and EO calculated for a single droplet rising in a heavier fluid

As shown in Table1.8 after calculating the Re, and EO at steady motion of the droplet, the shape of the droplet is oblate ellipsoid cap which agrees very well with those obtained by Amit and Kumar. Amit and Kumar plotted the regime map for different bubble shapes [44]. This proves that the surface tension coefficient determined by the test described above is valid. It also proves that the multi-relaxation time multiphase lattice Boltzmann model developed here can accurately captures the flow induced by the rising droplets.

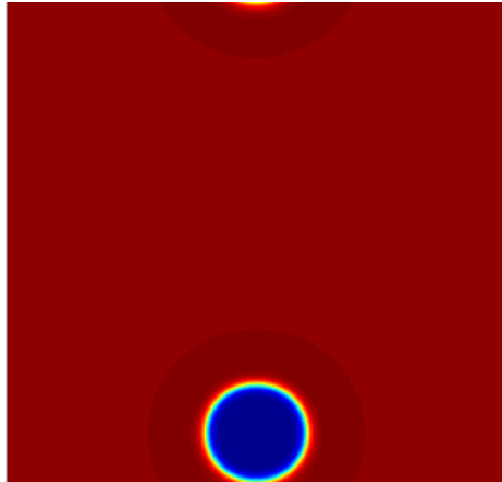
5.1.3. Single Droplet

In density contours, the red color denotes the higher density fluid while the blue color denotes the lower density fluid. A 300×300 node lattice is sufficient to provide the spatial convergence in all simulations presented here. Since the lattice spacing and the time steps are related in the lattice Boltzmann method through the lattice speed, c ; the corresponding time step of 0.00015 sec is sufficient to provide the temporal convergence.

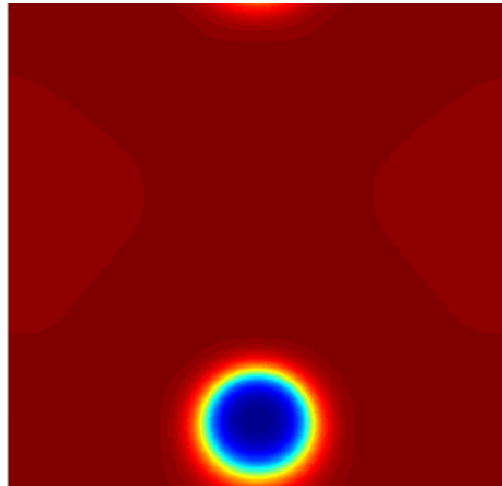
Both no-slip and periodic boundary conditions are imposed at the lower and the upper boundaries. For the time steps and the spacing between the lattices selected in the present simulations, the relaxation frequency, inverse of relaxation time, for lighter fluid is $\omega_1 = 0.5657$ and for the heavier fluid is $\omega_2 = 1.3815$. The density ratio of fluids is 1.2 and the Atwood number, $At \approx 0.1$ where ρ_h and ρ_l are densities of the heavier and the lighter

fluids, respectively. The Atwood number of this flow corresponds to the Reynolds number. Figures 49 and 50 show the density contours at various times for a single droplet placed at the bottom of the boundary at $t = 0$. The no-slip boundary condition is imposed on the velocity field at the bottom boundary. The initial shape of the droplet is circle. It is noted that the droplet is attached to the boundary at a single point. At time $t = 0.071$ sec the droplet is slightly elongated in the direction of gravity and it is still in contact with the boundary. At the later stages the droplet rises above the boundary and the tail of the droplet streaks of the lighter fluid extend to the surface. The back side of the droplet is nearly flat with a small dimple at the center region of the back side. At $t = 1.57$ sec the tail is completely broken and the droplet assumes the shape of the crescent, caused by the faster rise of the bottom compared to the front and side section of the droplet. The effect of the boundary on the dynamics of the droplet is obvious but not that strong. This is due to the fact that the droplet touches to the boundary at a single point. More pronounced effects of the no-slip boundary would have been studied. The D2Q9 Shan and Chen model multi-components has been employed to model the interactive forces. The density contours for no-slip and periodic boundary conditions on the side walls have been shown in Figures 43 and 44.

a) $t = 0.0356$ sec



b) $t = 0.3919$ sec



c) $t = 1.38$ sec

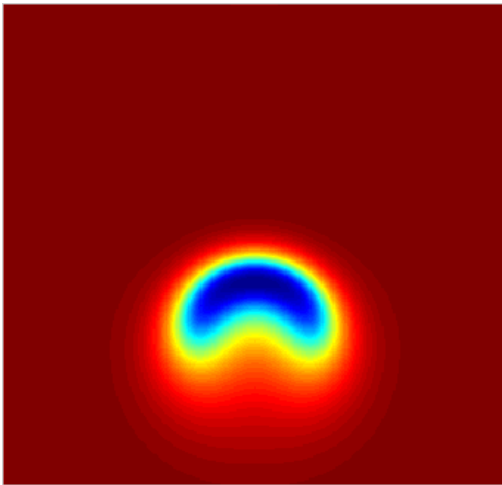
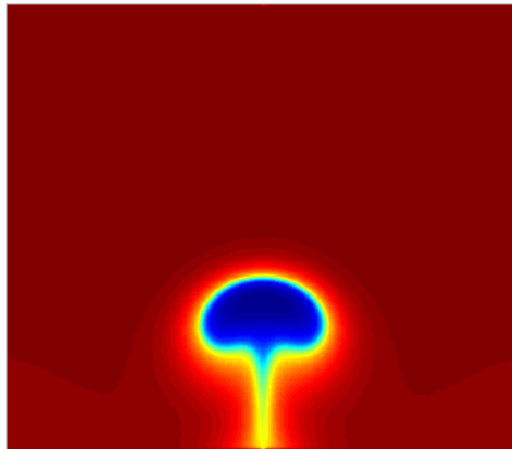
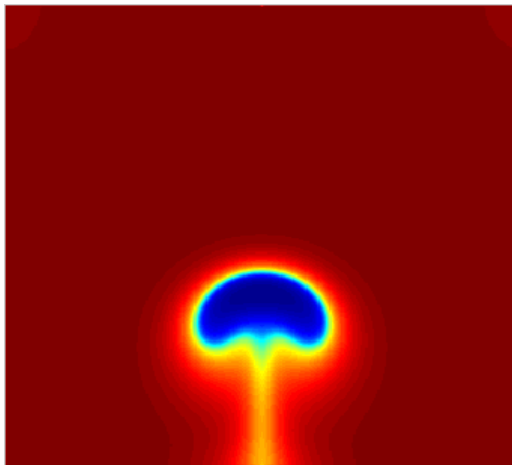


Figure 43. Density contours of a single rising droplet in an infinite domain. Images are calculated at various times.

a) $t = 1.351 \text{ sec}$



b) $t = 1.57 \text{ sec}$



c) $t = 2.031 \text{ sec}$

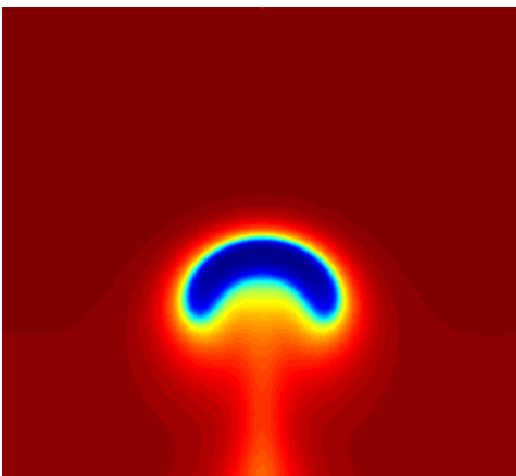
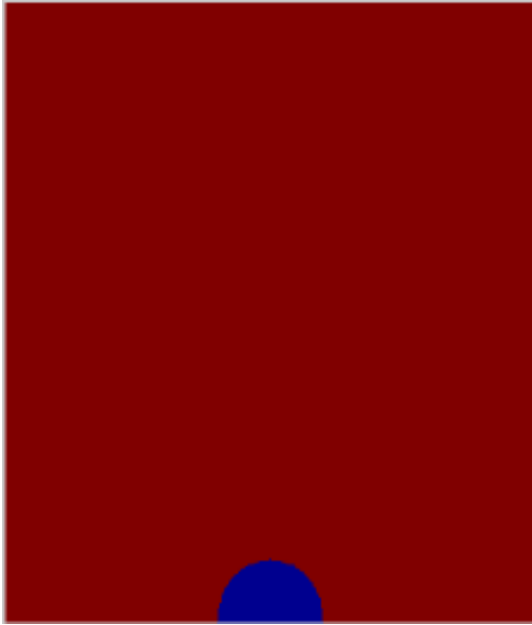
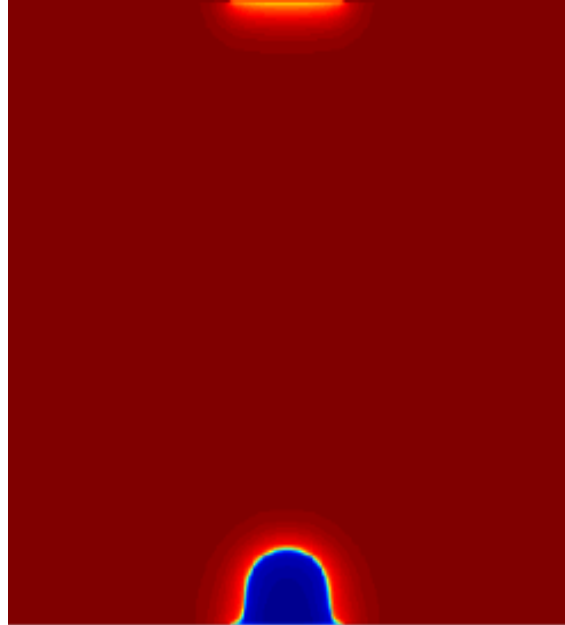


Figure 44. Density contours of a single rising droplet with no-slip boundary at the bottom and top walls. Images are calculated at various times.

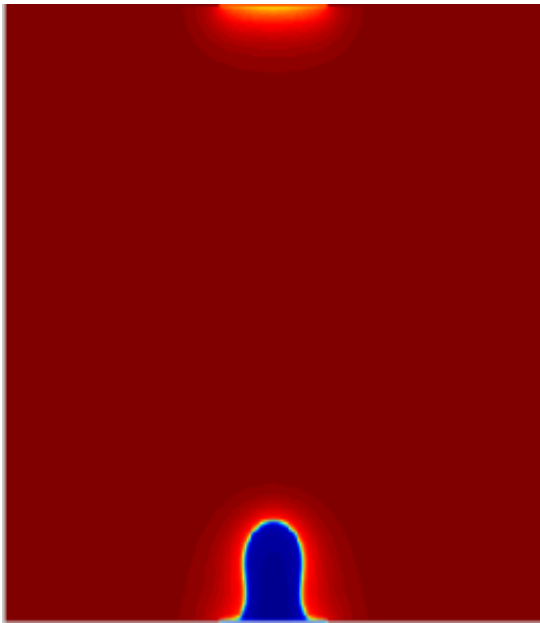
Initially, the semi-circled shaped droplet placed on the no-slip bottom boundary. The no-slip boundary is also applied at the top boundary while periodic conditions are applied at the side boundaries. Again the droplet is lighter than the fluid around it. The droplet starts rising and it is elongated in the direction of gravity. At the early stages it is still attached to the boundary, but as time progress it develops a filament connecting the droplet to the no-slip surface. This filament is stretched and eventually breaks up. As the unattached droplet rises in the heavier fluid the residue of the droplet sticks to the surface, as shown in Figure 45. The buoyancy force is not strong enough to lift the residue of the droplet away from the surface so the residue remains on the surface. The influence of the no-slip boundary on the evolution of the droplet is very strong, as shown in Figure 46. The instantaneous streamlines and the vorticity contours are depicted, as shown in Figure 46a and c, for a single semi-circled droplet that is initially placed on the no-slip boundary at time, $t = 0$ sec. The interface separating the droplet from the heavier fluid is also shown on the contours of the stream function. Two counter rotating vortices cover both the droplet and the heavier fluid. Another pair of weaker counter rotating vortices at each side of the droplet is also present. The intensity of the flow is much stronger near the droplet as the flow is induced by the rising droplet, as shown in Figure 46c. The fluid away from the droplet is undisturbed as shown both by flow and the vorticity field. The pressure gradient is induced by the rising droplet, as shown in Figure 46d.



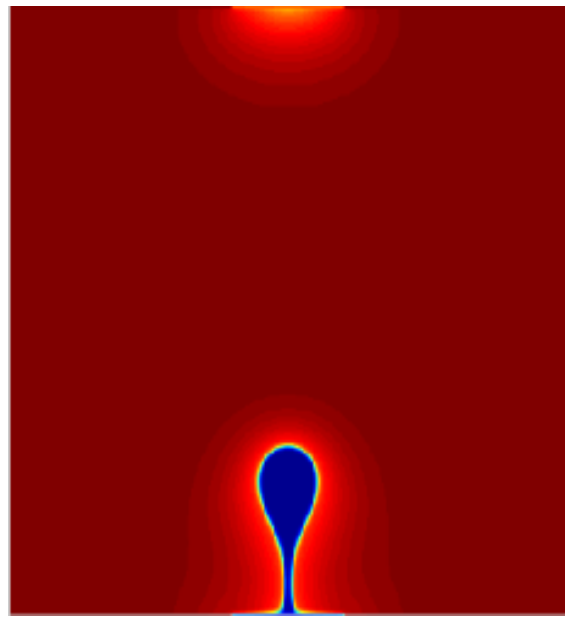
a) $t = 0.0$ sec



b) $t = 0.340$ sec



c) $t = 0.660$ sec



d) $t = 1.88$ sec

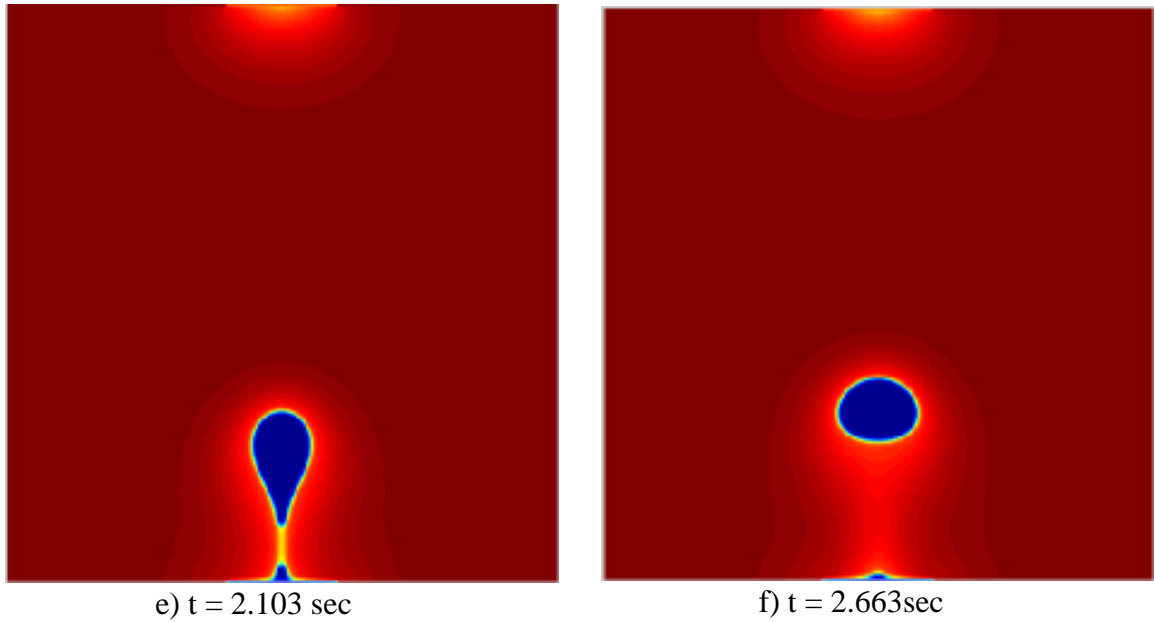
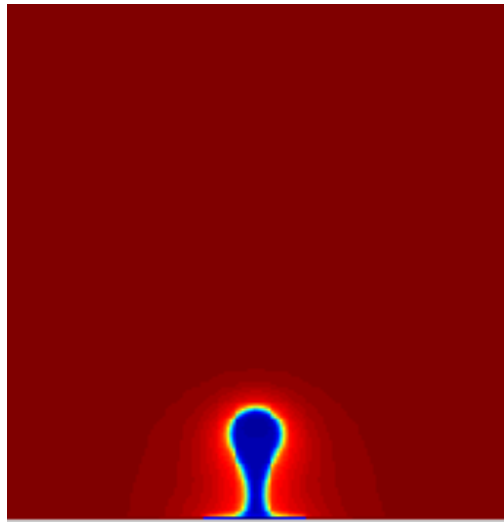
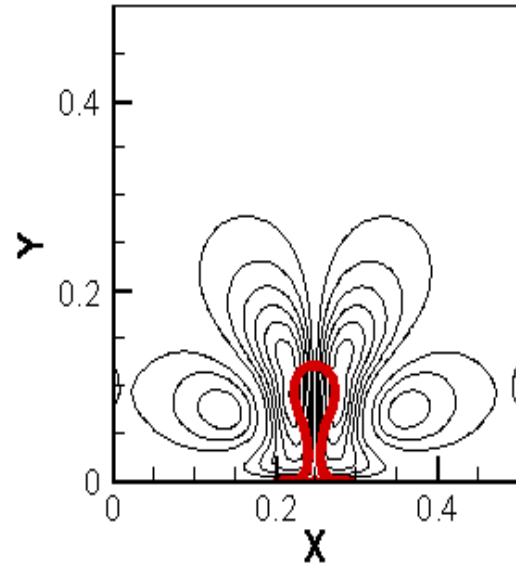


Figure 45. Density contours for the single semi-circled droplet at various times.

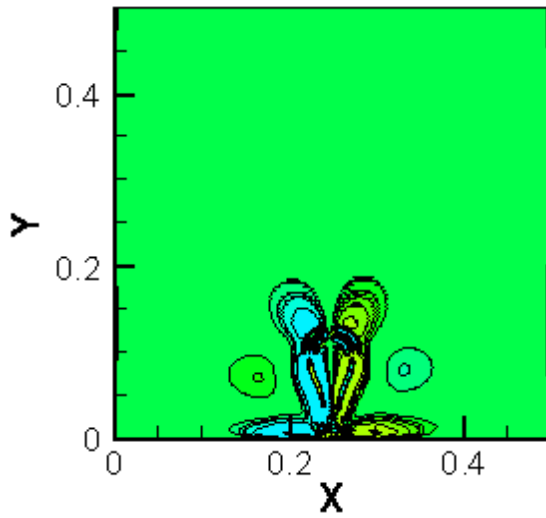
The contact area of the droplet is $2R$, where R is the radius of the droplet. The amplitude of the interaction strength is $G = 1.6$. The rising droplet creates small neck and breaks up. It moves in the opposite of the direction of the gravity and creates awake region behind the rear surface of the droplet. The residue of the droplet stays on the surface since there is not enough buoyancy force to remove the residue of the droplet from the surface. In the late stage, the rising droplet move inside the heavier fluid and reaches to the equilibrium state and its shape becomes constant, as shown in Figure 47a.



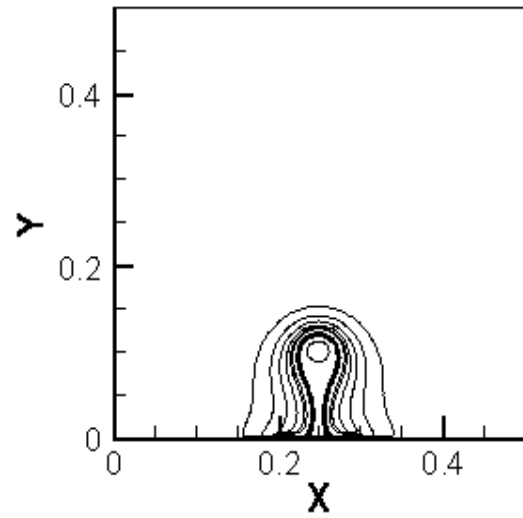
a)



b)

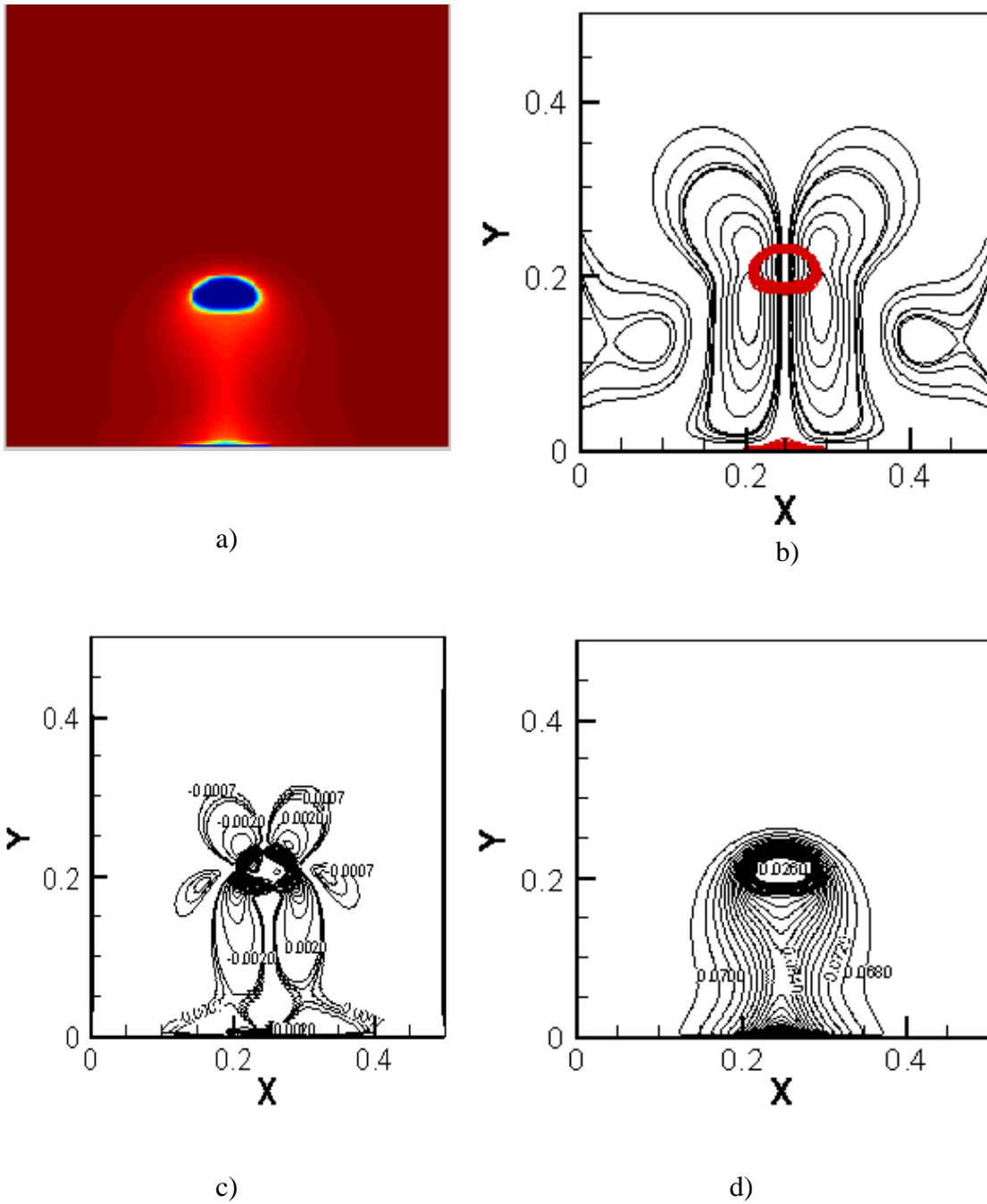


c)



d)

Figure 46. a) Density contours, b) streamlines contours, c) vorticity contours, and d) pressure contours of a single semi-circled droplet placed on the lower boundary at $t=1.17$ sec.



Pressure: 0.0260 – 0.102 mu/lu^2

Figure 47. a) Density contours, b) streamlines contours, c) vorticity contours, and d) pressure contours of a single semi-circled droplet placed on the lower boundary at $t = 2.27$ sec.

5.1.4. Flow Structures and Flow Regimes

In this section different arrangements of the droplet and the effect of the boundary on the terminal shape of the droplet have been investigated. A single droplet arrangement is placed inside the domain with different side wall boundaries.

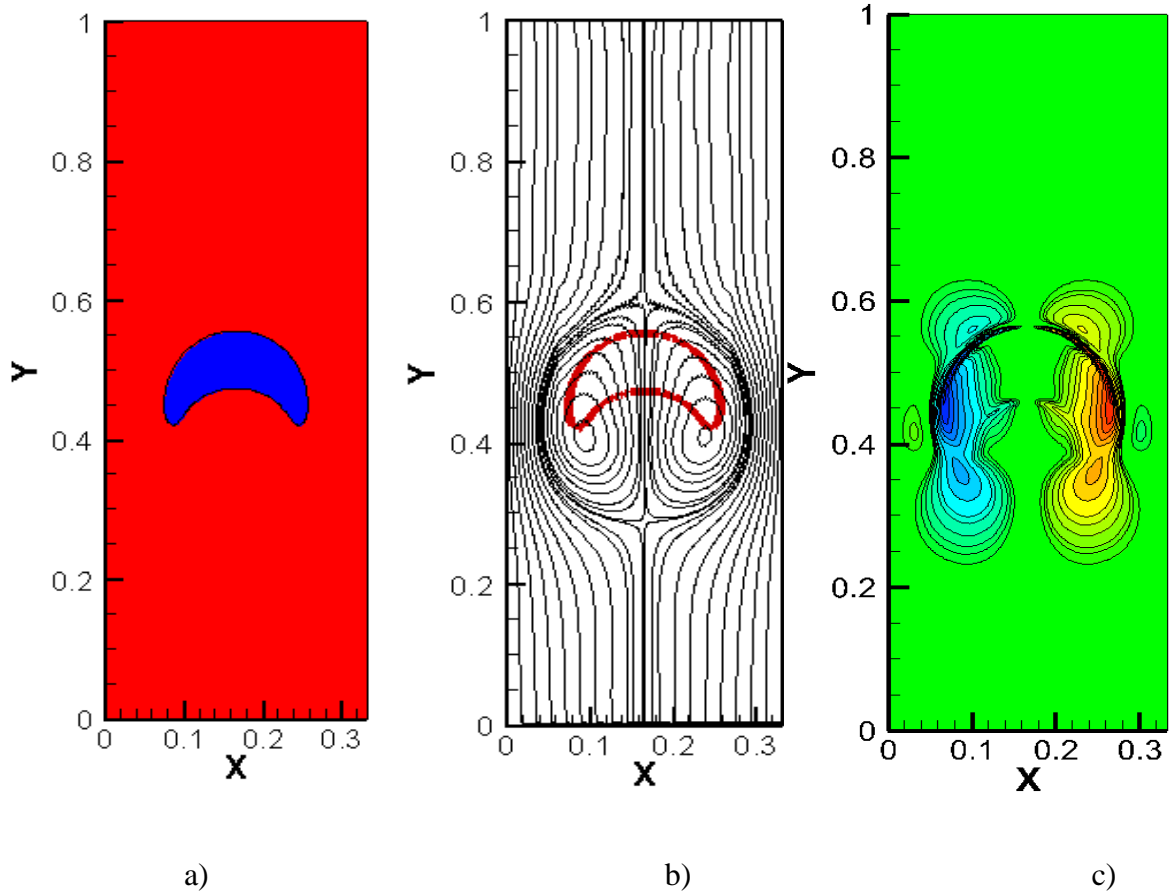
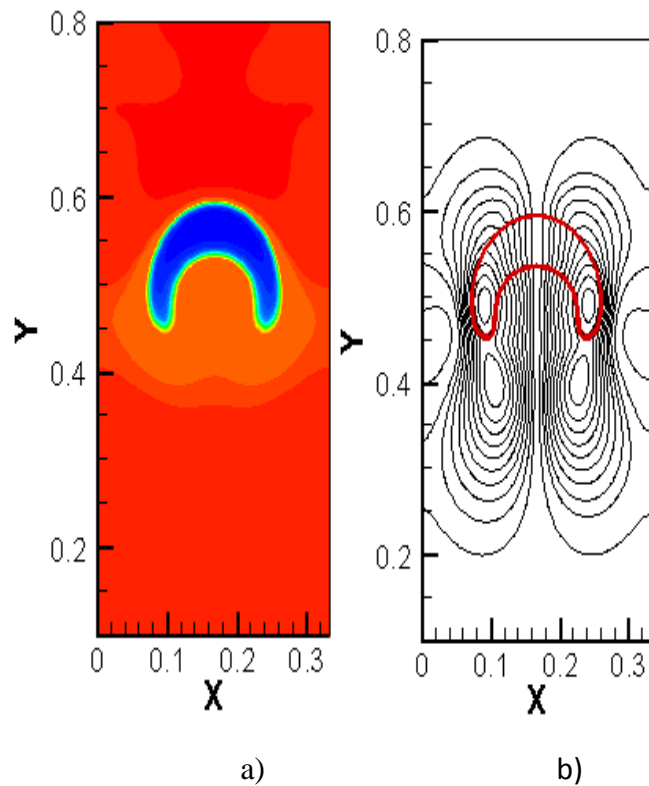


Figure 48. a) Density contours, b) streamlines contours, and c) vorticity contours of a single rising droplet. No-slip boundary condition is applied at side walls and periodic boundary condition at the top and the bottom walls.

The lighter fluid droplet rises in a heavier fluid with periodic top and bottom boundary conditions and no-slip boundary in the side walls. In the early stage the shape of the rising droplet changes. The back side of the droplet rises faster compared to the front side leading the shape predicted at later stage, as seen in Figure 48. The terminal shape of the droplet

and the flow field around the droplet is shown in Figure 49 for fully periodic boundaries. The rising droplet induces a flow in both fluids, as shown in Figure 49a and b. The location of the droplet is imposed on the contour of the stream function to better illustrate how the flow field is induced by the rise of the droplet. The complex flow field is present in the vicinity of the droplet with the presence of small and large scale recirculating vortices. They dissipate quickly away from the droplet. Larger pressure gradient is present at the front side of the droplet, as shown in Figure 49d.



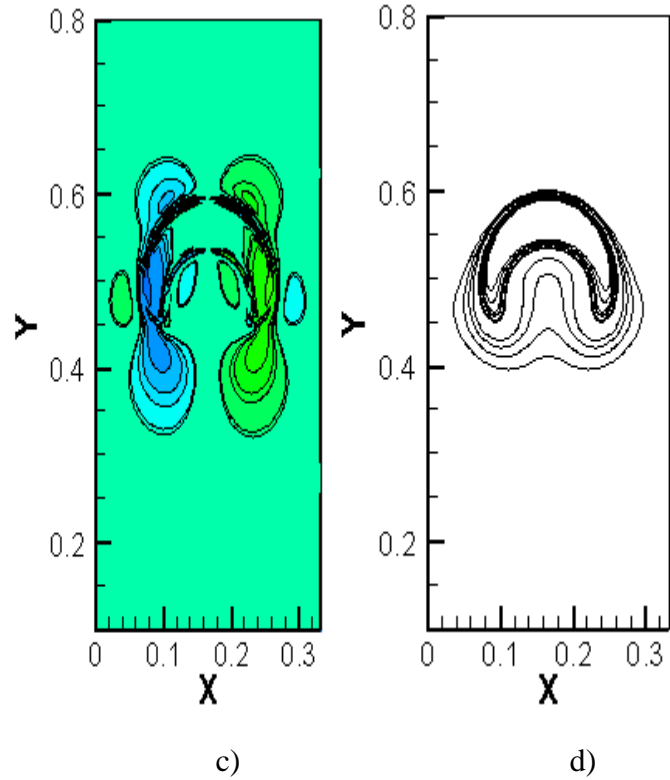
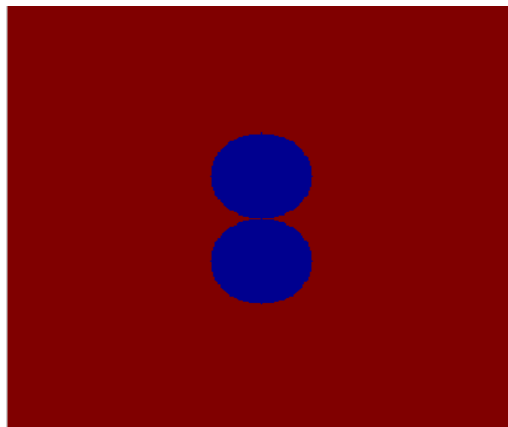


Figure 49. a) Density contours, b) streamlines contours, c) vorticity contours and d) pressure contours for a single droplet rising in an infinite fluid. Images are shown at $t = 1.16$ sec.

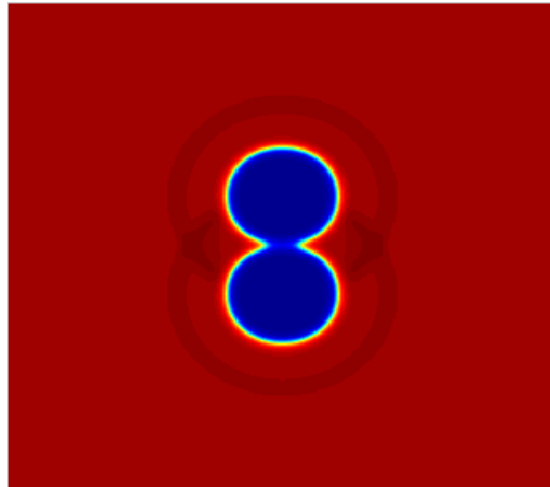
5.1.5. Two and Four Droplets

The two droplets are placed on the infinite domain. Initially, the two droplets are placed close to each other's. At the early stage the droplets merge in a point. At the late stage the two droplets completely merge together and create a crescent structure as shown in Figure 50.

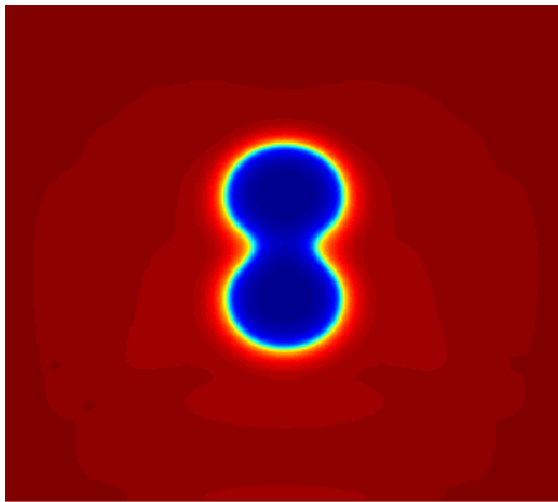
a) $t = 0$ sec



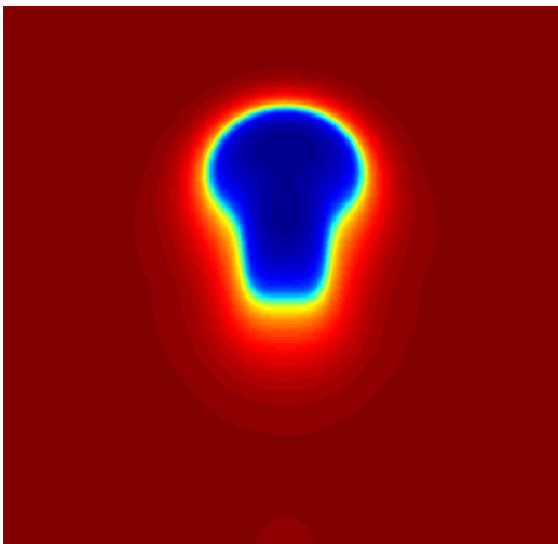
b) $t = 0.0356 \text{ sec}$



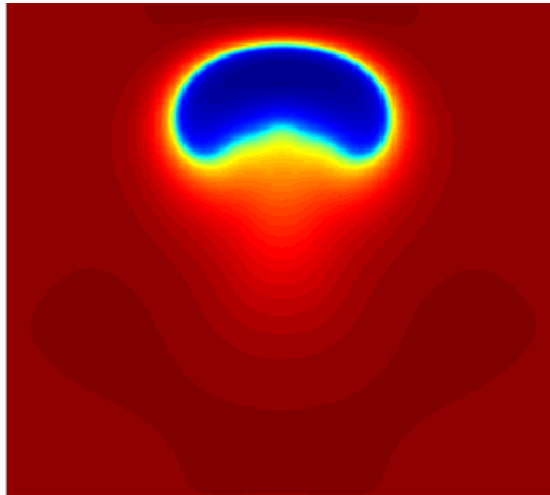
c) $t = 0.213 \text{ sec}$



d) $t = 0.816 \text{ sec}$



e) $t = 1.425$ sec



f) $t = 1.532$ sec

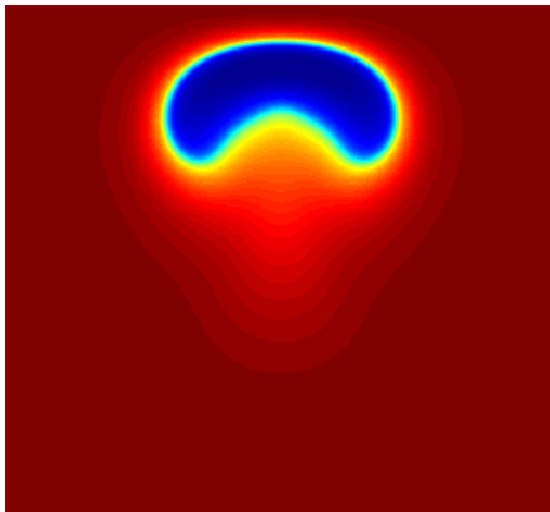
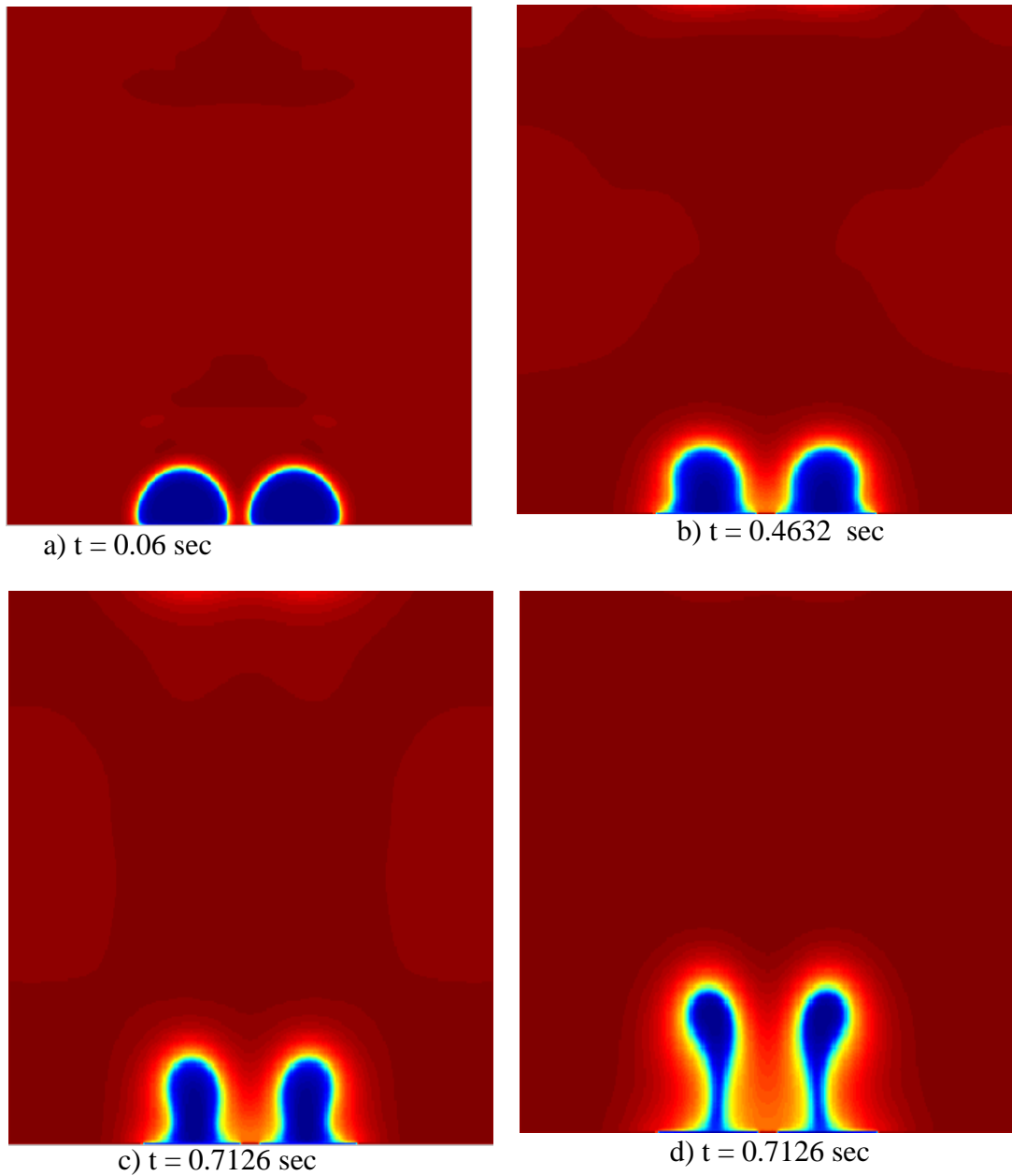


Figure 50. Density contours of the two vertical adjacent droplets at various times.

The two semi-circled droplet is initially placed on the lower boundary, as shown in Figure 51. The contact area of the droplet is $2R$ and the amplitude of the interaction strength is $G = 1.6$. In the early stage the two droplets elongate in the direction of the gravity. In the late stage, each droplet creates small neck and breaks up. They move in the opposite direction

of the gravity. Part of droplets stay in the lower boundary since there is not enough buoyancy force to remove the residue of each droplets from the surface. The rising droplets move inside the heavier fluid and reach to the equilibrium state. As they reach the equilibrium state their shape become constant, as shown in Figure 52a.



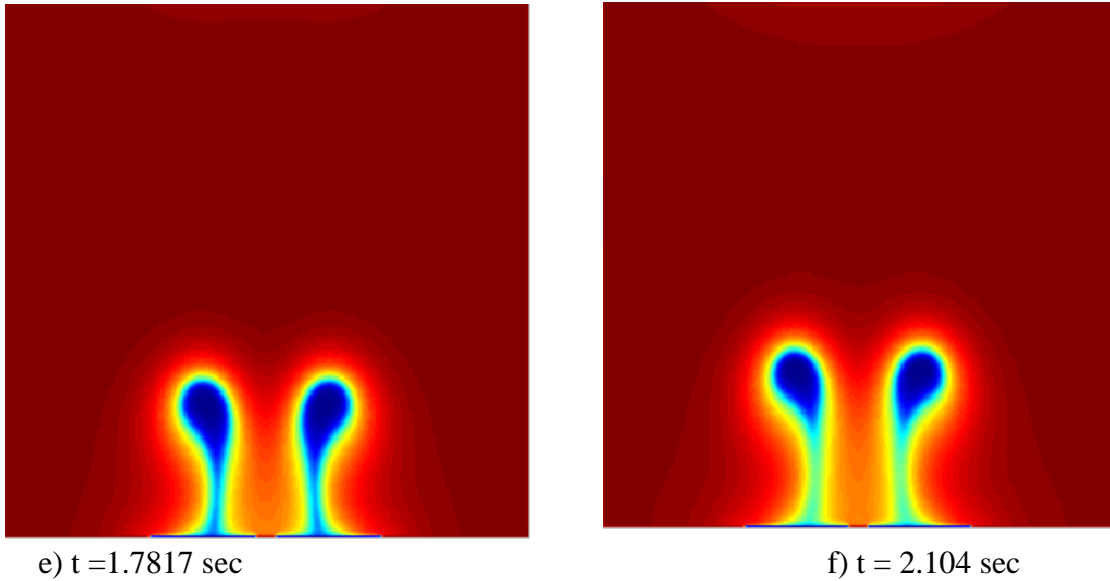


Figure.51. Density contours of two semi-circled droplet placed on the lower boundary at various times.

Figure 51 shows the density contours of two semi-circled droplets at various times. The effect of the no-slip boundary on the shape of the semi-circled droplet is clear and the droplet elongates in the direction of the gravity. The residues of the droplets remain on the boundary and stretch horizontally on the boundary as shown in Figure 51e and f. Finally, the droplet takes spherical cap shape and their shape keep constant because the droplet reaches to the equilibrium state. The pressure gradient and the vorticity is induced by the rising droplet are shown in Figure 52c and d for the late stage. The small and large scale vortices can be seen clearly near the droplets.

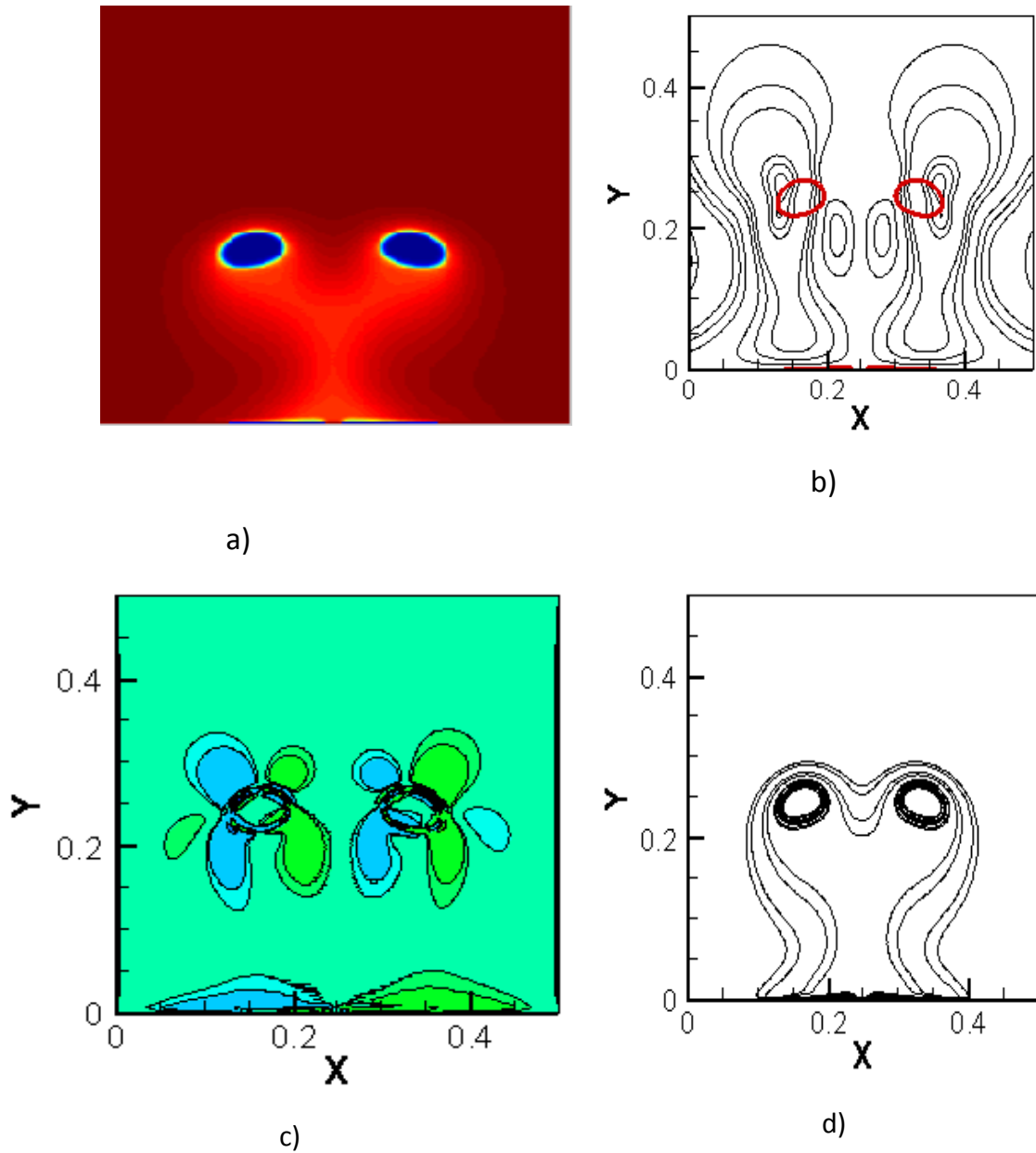
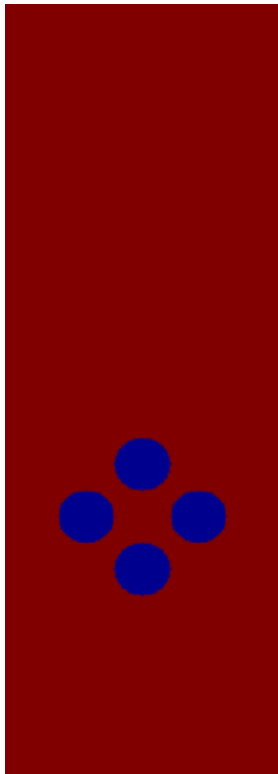


Figure 52. a). Density contours, b) streamlines contours ,c) vorticity contours, and d) pressure contours of two semi-spherical droplets placed side by side at $t = 4.12$ sec

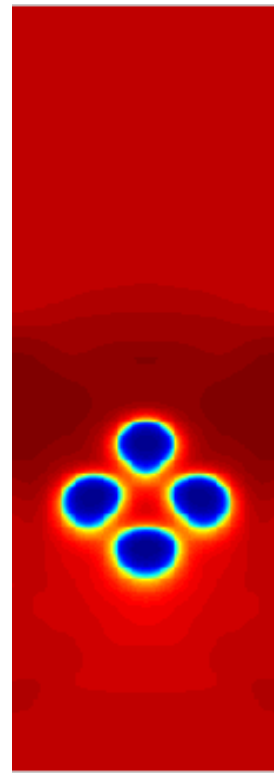
Periodic boundary conditions are imposed at the side boundaries and the top boundary is a no-slip and no-penetration surface. The droplets move away from each other's as they rise. This is due that fact that the heavy fluid flowing between two droplets exert a drag force on each fluid. Each droplet is tilted slightly and the drag force acting on each droplet pushes them apart from each other. At time, $t = 2.1$ sec, the droplets are attached to the surface by

a thin filament, as seen in Figures 52a. At later stages of the flow, both droplets are unattached from the surface and still move away from each other. Even later stage of the flow, the residue remains on the no-slip surface and spreads over the surface while the unattached droplets rise further into the heavier fluid as seen in Figure 52a. Again the no-slip surface strongly influences the development of the droplets and the flow induced by the rising droplets. Instantaneous streamlines and the vorticity contours are shown in Figure 52a and c for the two semi droplets case discussed above at the time, $t = 4.12$ sec. The location of the droplets is imbedded on the contours of the stream function; helping to relate the induced flow field to the rising droplets. The presence of several counter rotating vortex pairs and their interaction with the no-slip boundaries are creating a very complicated flow field around the rising droplets [56].

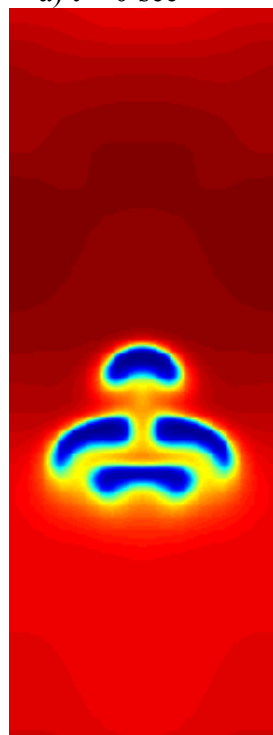
Figure 53 depicts the evolution of four droplets in bounded medium. The shape and the dynamics of each droplet are influenced significantly by the presence of the other droplets in the field. The initial shape and the configuration of the droplets are illustrated in Figure 53a. The top droplet assumes nearly the shape of the oblate ellipsoid and remains unattached from the other droplets at all times, as shown in Figure 53a. However, its shape is still influenced by the other droplets. The droplets in the middle show a quite complicated evolution. Their leading edge gets closer to each other and merges at the later stages of the flow. Their trailing edge separates and coalescences with the droplet which was located at the bottom initially, as shown in Figure 53c and 53d.



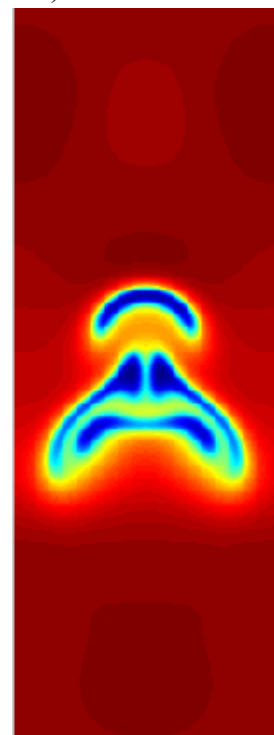
a) $t = 0$ sec



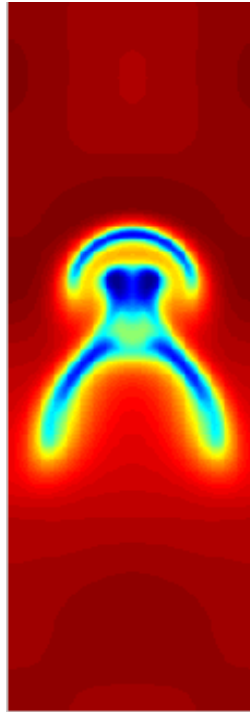
b) $t = 0.313$ sec



c) $t = 0.835$ sec



d) $t = 1.47$ sec



e) $t = 1.77$ sec

Figure 53. Density contours of four droplets at various times.

Figure 54 shows the flow field near the four rising droplets in an infinite fluid at $t = 1.47$ sec. The density and the streamlines contour are shown together in Figure 54. The complex flow field around the droplets is obvious from these images. Both the intensity of the vortices and the pressure gradient induced by the rising droplets decay rapidly away from the droplet. The pressure field is determined by the density field. Hence the pressure contour is similar to the density contour.

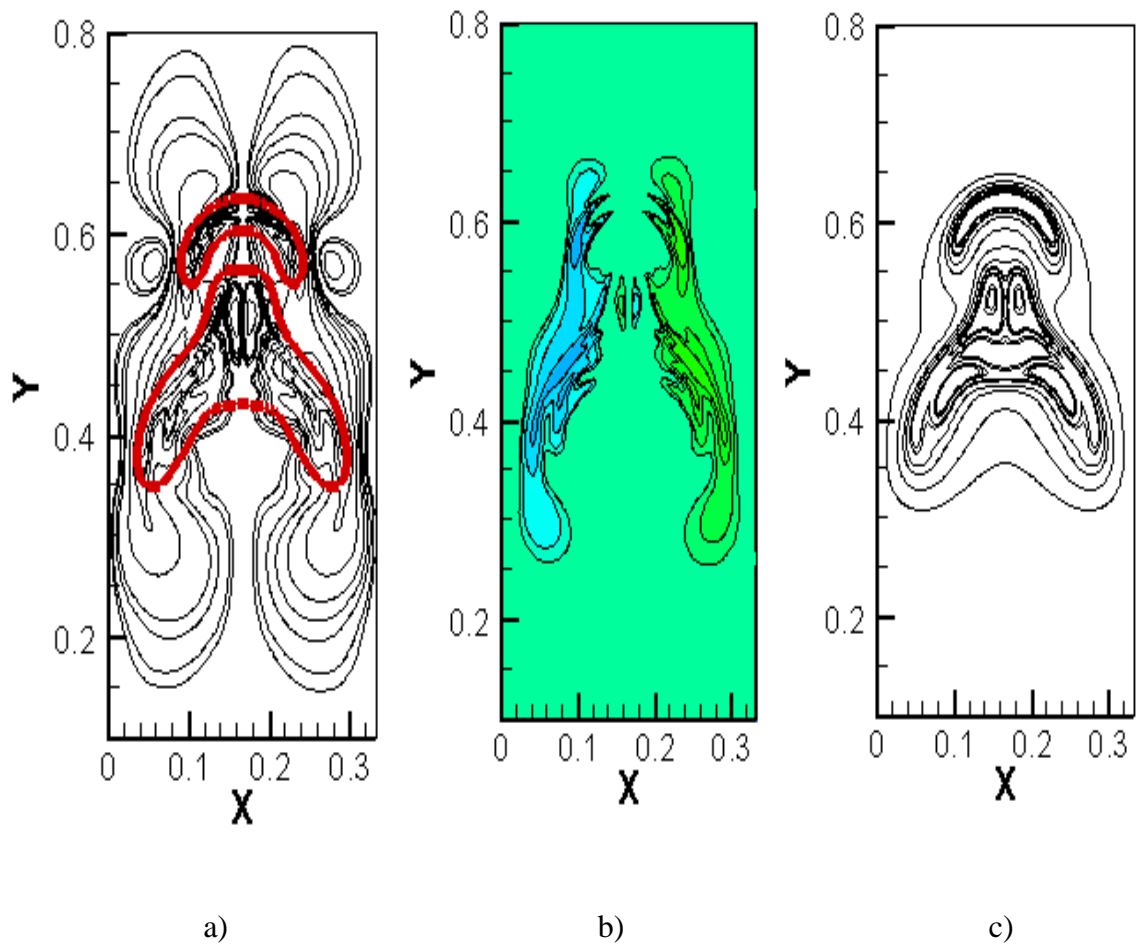


Figure 54. a) Streamlines contours, b) vorticity contours and c) pressure contours for four droplets rising in an infinite domain at $t = 1.47$ sec.

The wall effects can be seen clearly on the flow structure around the droplets. Mainly, the initial condition is that a lighter density droplet is suspended in a heavier fluid. The droplet is determined to be in equilibrium when the shape changes are insignificant. Figure 55 demonstrates the density and pressure profiles along the center line of the droplet when equilibrium state is reached. The size of the computational domain is 300×300 . The initial diameter of the droplet is 35 lattices (spherical droplet). The center of the spherical droplet is located at the center of the computational domain. The pressure inside is constant up to the interface and is constant outside the droplet. The difference between the two constant

values of pressure can be used to evaluate the surface tension for different droplet size as it is discussed earlier.

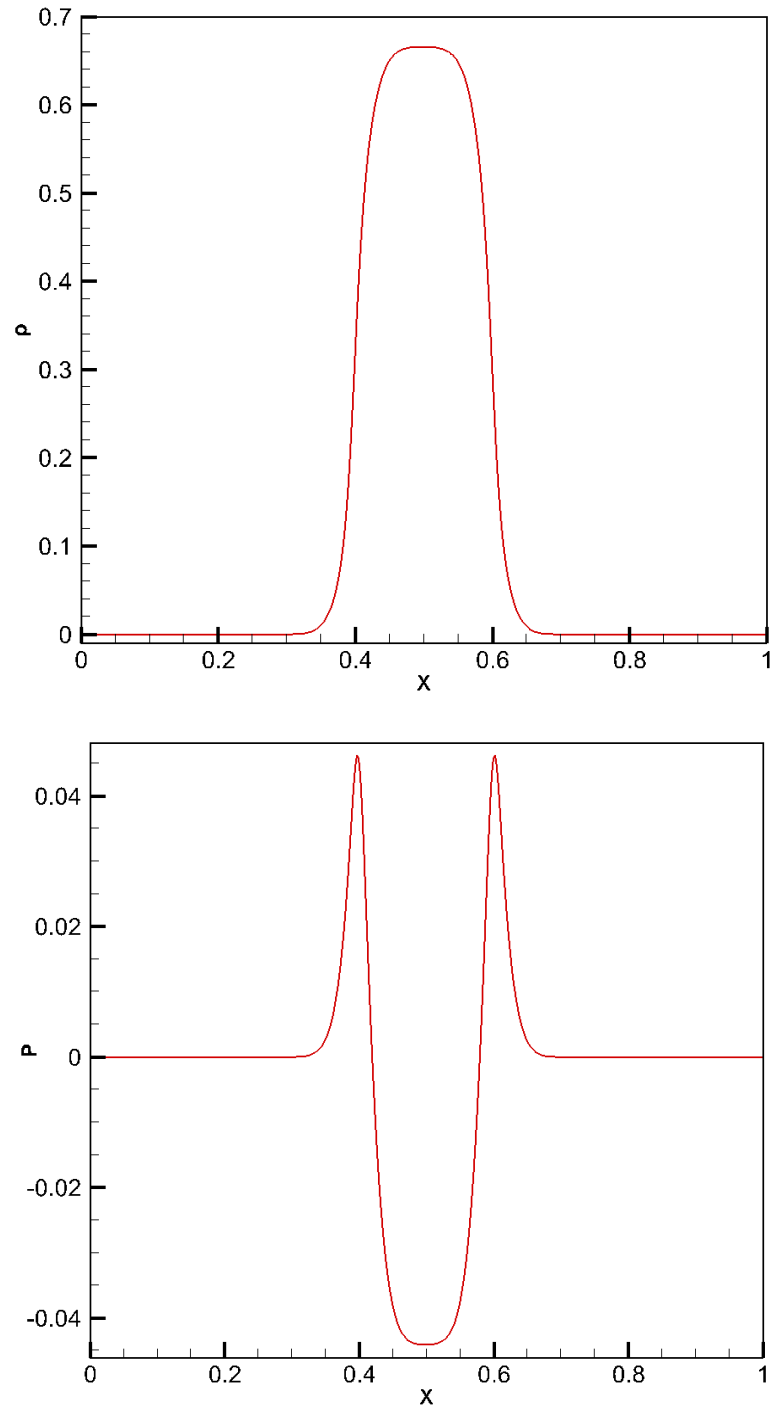


Figure 55. The equilibrium pressure and the density profiles along the center line of a droplet.

5.2. Rayleigh Taylor Instabilities

5.2.0. Objective

The Lattice Boltzmann Method (LBM) is employed to study a number of complex interfacial flows induced by the Rayleigh Taylor (RT) instabilities [57, 58]. Previous studies have shown the LBM can be an effective tool for studying multiphase flows [59]. Andrea Parmigiani (2010) applied LBM to study multi-phase flows [60]. A stagnant heavier fluid is placed above a stagnant lighter fluid in this study. This is an unstable equilibrium so any disturbance in the system will grow and create a flow. In general the RT instability occurs when a body force is present in the direction opposite to a steep density gradient [60-63]. Here, the method that was developed in the past research was used to study more interesting RT instabilities. The first two cases being studied show the RT instability initiated from periodic disturbances. Our interests in these flows lie in LBM's ability to model the nonlinear stage of the RT instabilities. The pulling of the initially flat interface is also considered a form of disturbance the system.

5.2.1. Introduction

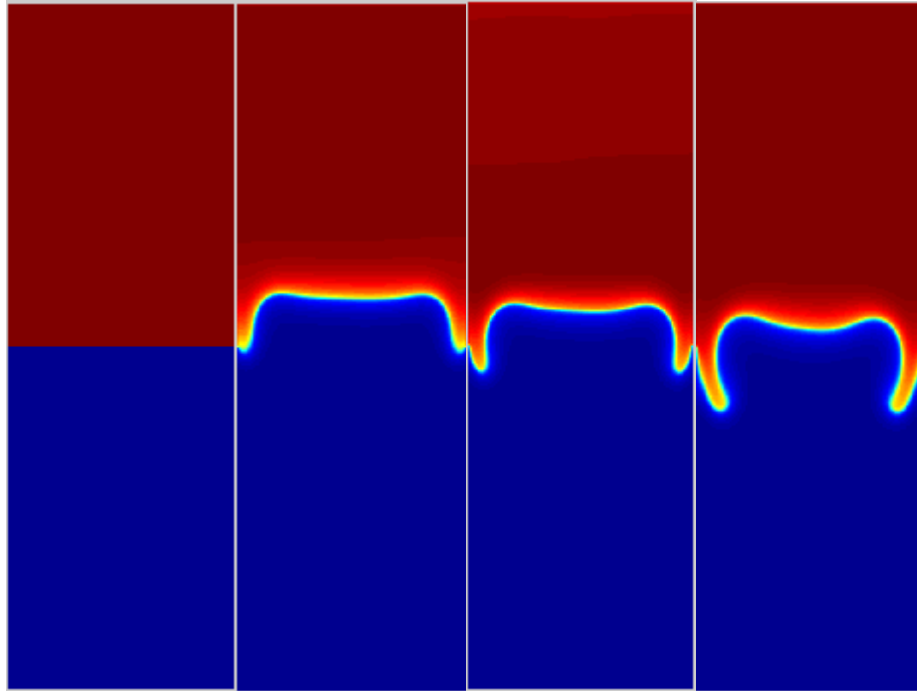
Evolution of RT instabilities are presented for various cases. The multi components Shan and Chen model (1993) has been employed here to study Rayleigh Taylor Instability of oil and water. The density ratio of fluids is 1.2. The thermo-physical properties of oil and water are shown in Table 1.8. Various type of boundary conditions are considered to study the wall effect. Different fluid arrangement in a two-dimensional geometry is considered at various values of aspect ratios [57, 58].

Working Fluid	ρ ($\frac{\text{kg}}{\text{m}^3}$)	ν ($\frac{\text{m}^2}{\text{s}}$)	λ (kg/s ²)
Water	1000	1×10^{-6}	0.072
Oil	825.1	10.6×10^{-6}	0.036

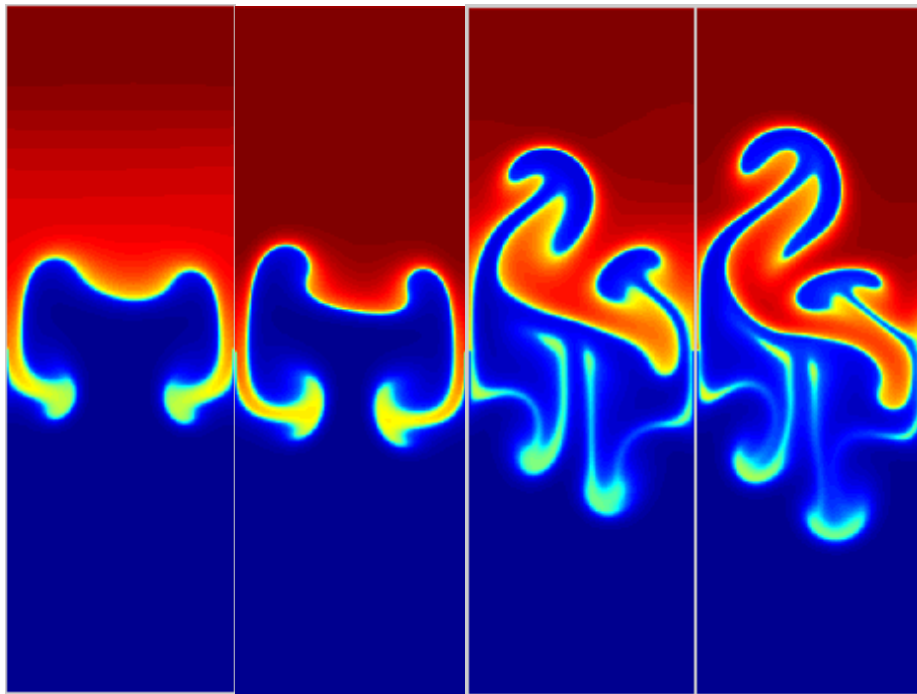
Table 1.9. Thermo-physical properties of water and oil.

5.2.2. Two Layers with AR=1/3

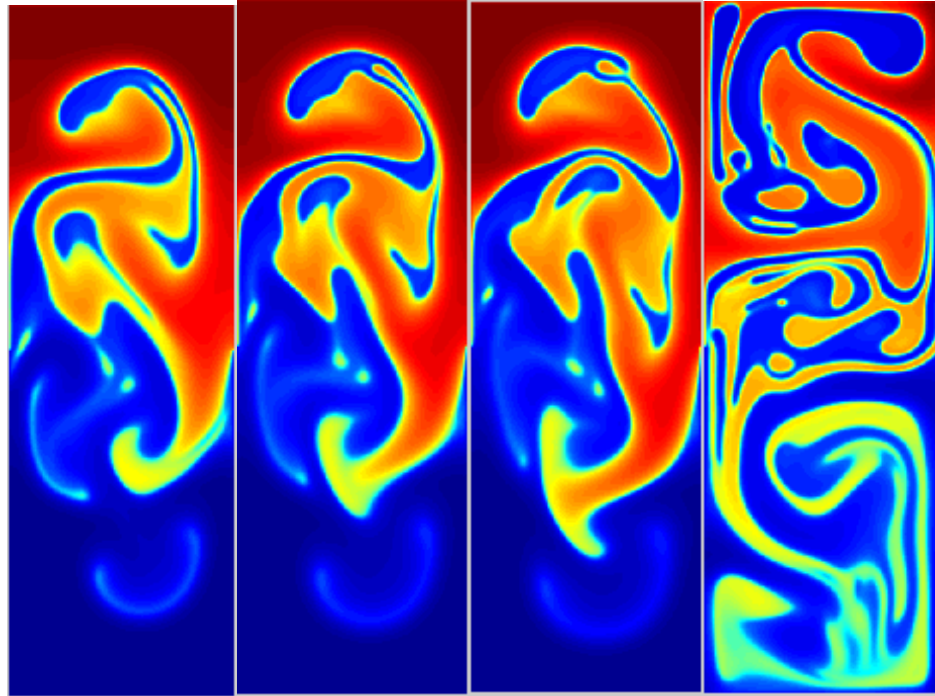
The water is placed at the top and the oil is placed at the bottom. The simulation is carried out for 300×600 lattices and with time step of 1.0×10^{-3} . Shan and Chen multi-phase model has been employed in MRT lattice Boltzmann method. The aspect ratio is $AR = L/H = 1/3$, where L is the length and H is the height of the cavity. Both side walls are treated as no-slip surfaces. At the early stage of the instability the influence of side walls on the evolving interface and the flow structure is very significant. The classical mushroom structures manifested by RT instabilities are distorted by the no-slip walls. At even later stages, the top and the bottom walls influence the flow, as shown in Figure 56.



a) $t = 0$ sec b) $t = 1.53$ sec c) $t = 1.84$ sec d) $t = 2.385$ sec



e) $t = 3.60$ sec f) $t = 4.23$ sec g) $t = 6.165$ sec h) $t = 6.75$ sec



i) $t = 8.41 \text{ sec}$ j) $t = 9.10 \text{ sec}$ k) $t = 10.25 \text{ sec}$ l) $t = 14.65 \text{ sec}$

Figure 56. Density contours of two immiscible fluids (oil and water) at various times.

5.2.3. Two Layers with AR=1 and 2

The evolution of RT instabilities are studied here in a cavity with aspect ratio of 1 and 2. The oil and water are considered as fluids, as shown in Figure 57. The length of each fluid column is L and the height of light and heavy fluid is H_1 and H_2 , respectively. The aspect ratio is defined by L/H .

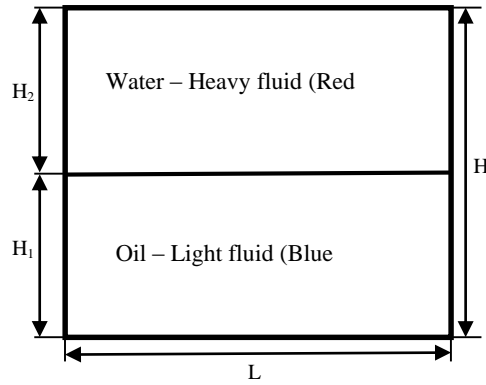


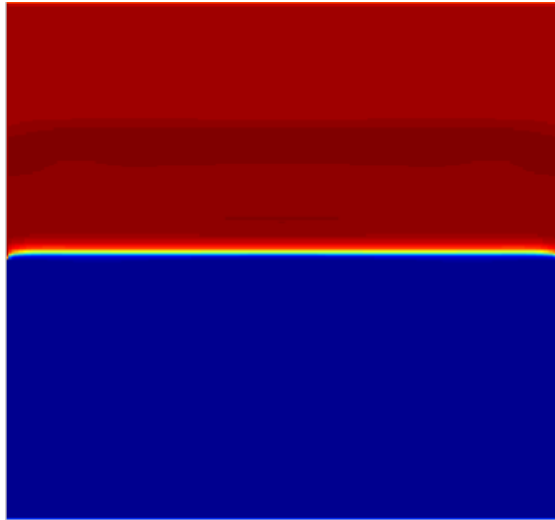
Figure 57. Schematic diagram of the two layers.

Three different types of disturbances are considered. Two different cases of the periodic disturbances with a wavelength of $3L$ and $5L$ and with normalized amplitude of 0.001 are studied. The third case of disturbance considered is the bump at the interface caused by pulling the interface [58]. The evolution of the unstable interfaces is investigated for aspect ratios of one and two. The effect of wall on the Rayleigh-Taylor instability is studied. 300×300 lattice grid is used, for aspect ratio of 1 and 600×300 lattice grid is used, for aspect ratio of 2. These lattice nodes in the D2Q9 orientation are selected to ensure the spatial convergence. Simulation is conducted using a time step of 2.5×10^{-4} s to ensure the temporal convergence. The Rayleigh number for each fluid is calculated to be $Ra_1 = 6.69 \times 10^7$ (lighter fluid) and $Ra_2 = 7.53 \times 10^9$ (denser density). For the selected time step and the lattice spacing the relaxation frequencies are calculated for water as $\omega_1 = 0.5657$ and for oil as $\omega_2 = 1.3815$. The contours of coloring function are shown in Figure 58 at various time. Flow manifested by the RT instabilities in this case is initiated by the periodic disturbance with wavelength of $3L$ and amplitude of 0.001 . The aspect ratio of the tank (L/H) is 1 for the images illustrated in Figure 58. The dark blue color denotes oil ($\kappa \rightarrow -1$) while the dark red color

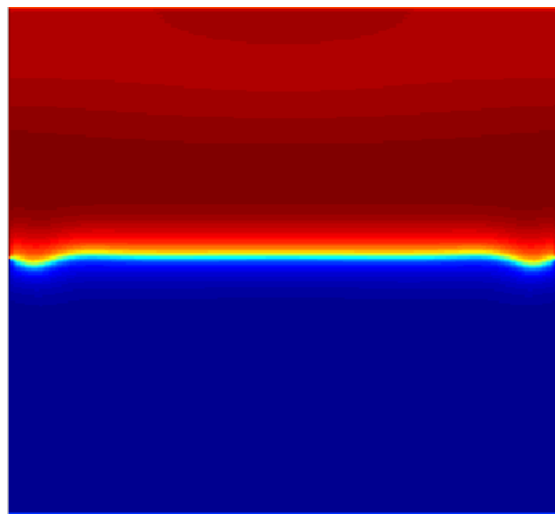
denotes water ($\kappa \rightarrow +1$). The system is unconditionally unstable to these disturbances so they will grow in time.

The red fluid pushed down initially is heavier than the fluid surrounding it and it will be pushed further down while the lighter fluid pushed up will move further up. This process will accelerate as the amplitude of the disturbance becomes larger. Growth of disturbance and the evolution of the Rayleigh-Taylor instability is strongly influenced by the presence of side walls. The instability grows much faster near the wall as shown even in the very early stage of the instability (see Figures 58a and b). The section of the interface near the middle is not disturbed as much as the parts near the side walls.

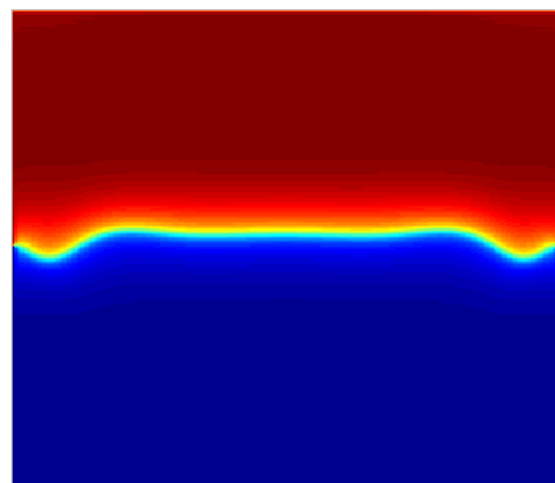
As the denser fluid sinks and the light density fluid (oil) rises the classical mushroom-like structure is formed. The mushroom-like structure in the water is being distorted by the presence of the boundary as shown in Figure 58 (e,f). At the later stage of the instability the influence of both side walls and the bottom and the top wall influence the dynamics of the interface separating two immiscible fluids, as shown in Figure 58f. The evolution of the interface and the growth of the instabilities can be seen clearly in the images shown in Figure 58 at various times.



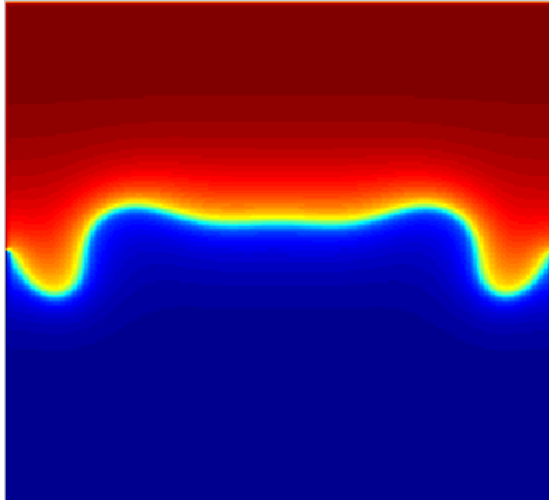
a) $t = 0.102$ sec



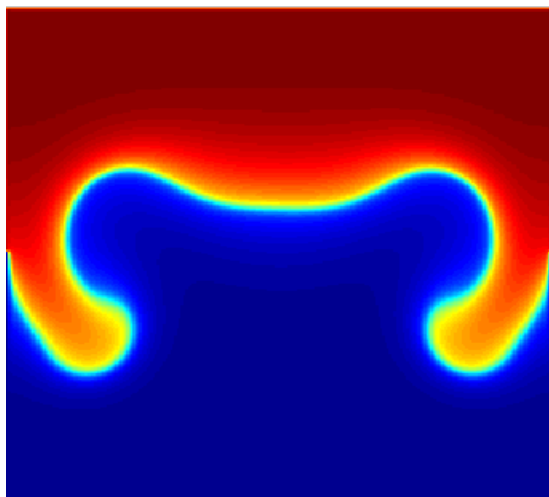
b) $t = 0.8$ sec



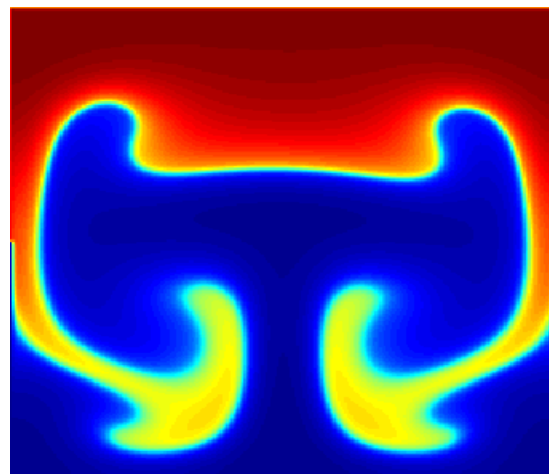
c) $t = 1.88$ sec



d) $t = 2.92$ sec

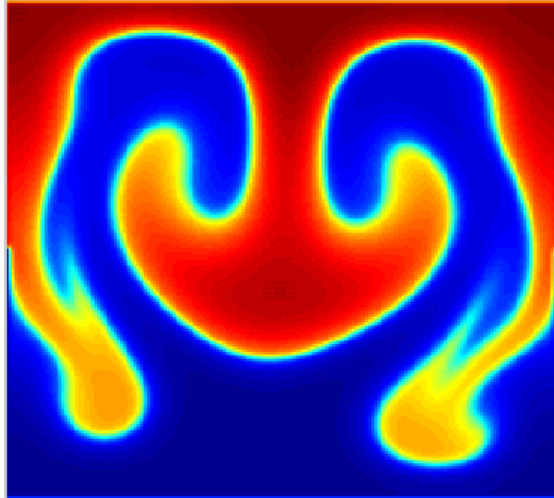


e) $t = 4.0$ sec

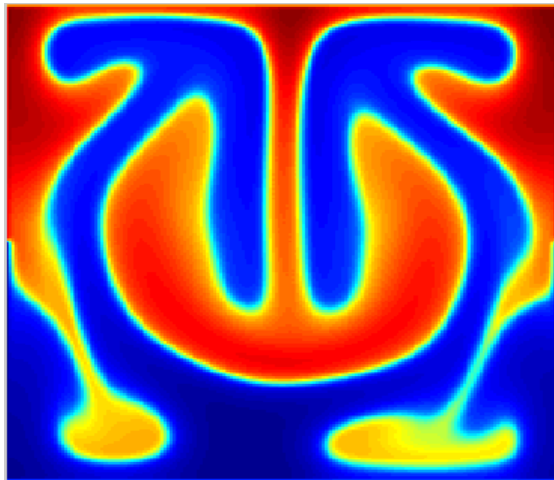


f) $t = 5.54$ sec

g) $t = 6.25$ sec



h) $t = 7.36$ sec



i) $t = 9.577$ sec

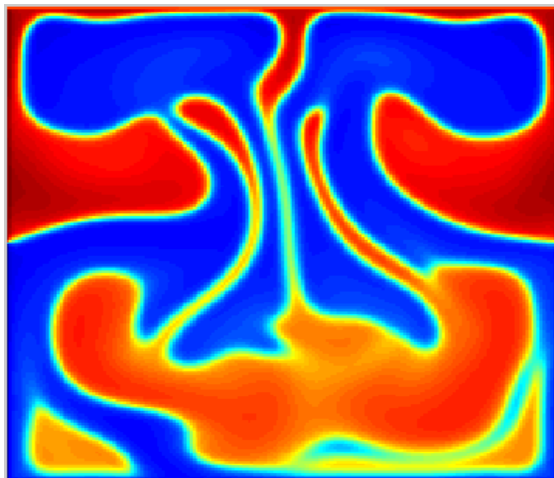


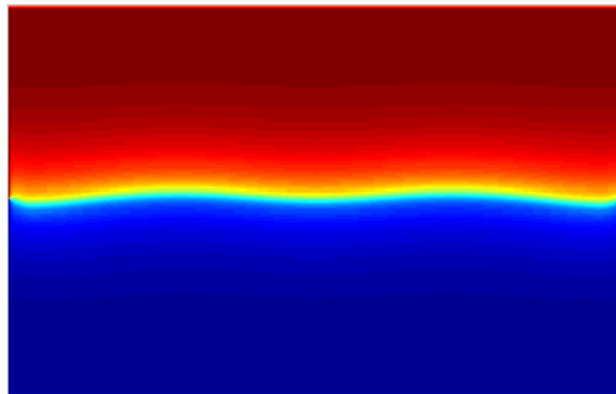
Figure 58. Density contours at various times. The blue color denotes oil while the red color denotes water. The initial disturbance is periodic with the wavelength of 3π and the amplitude of 0.001.

The contours of coloring function for the bounded case is shown in Figure 59 at various times for the initial periodic disturbance. The wavelength of the disturbance is $5L$ and the amplitude is 0.001 . At the early stages shown in Figure 59 (a,b,c), the Rayleigh-Taylor instability manifests itself with the wavy structure of the interfaces. The effects of the boundaries becomes obvious at the late stages of the instability as seen in Figure 59 (d,e,f). The interface is influenced by both side walls and the upper and the lower boundary as well. That makes the periodic interface being distorted. Instead it is seen that the water is being forced push to the center from each side by the rising oil pockets forming on the sides. These are the wall effects manifesting themselves at the later/non-linear stage of the instability, as depicted in Figure 59 (e,f).

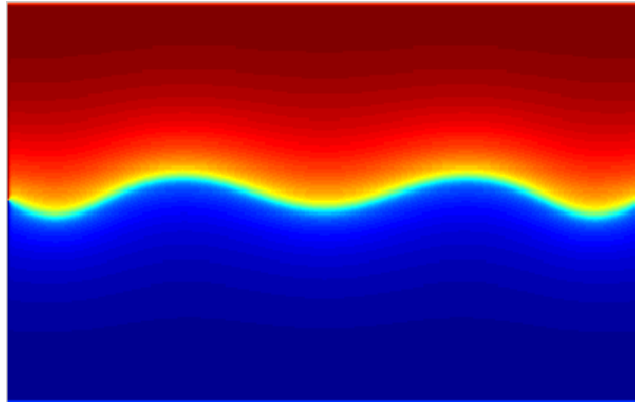
a) $t = 0.05\text{sec}$



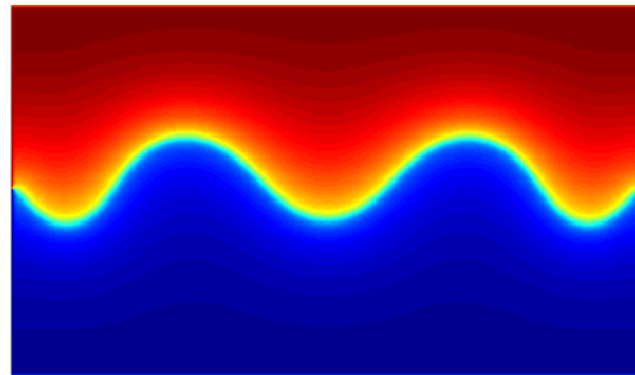
b) $t = 2.27\text{ sec}$



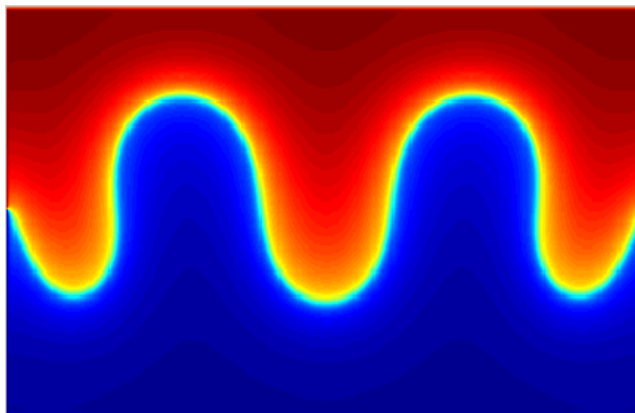
c) $t = 3.97 \text{ sec}$

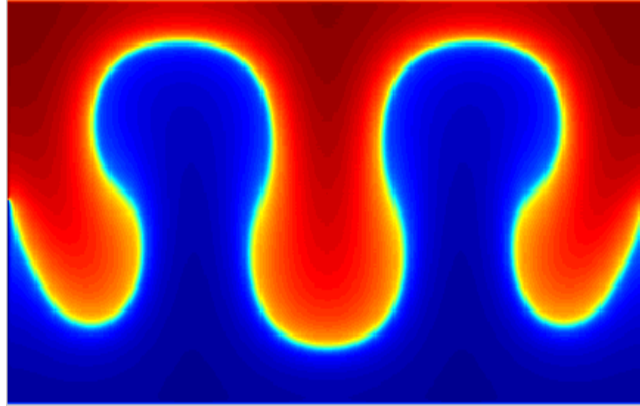


d) $t = 4.17 \text{ sec}$



e) $t = 5.760 \text{ sec}$



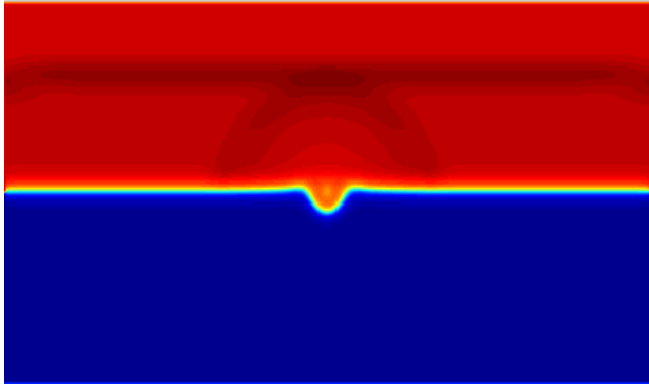


f) $t = 6.61$ sec

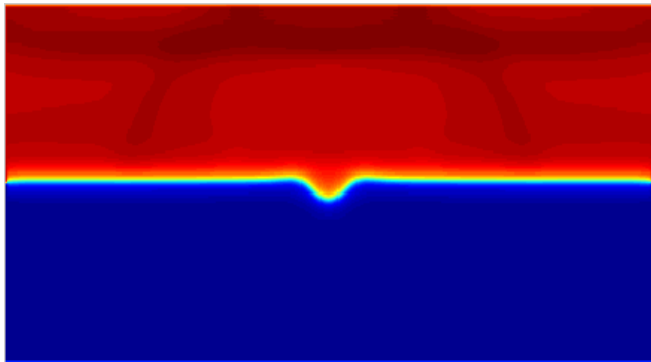
Figure 59. Density contours at various times. The blue color denotes oil while the red color denotes water. The initial disturbance is periodic with the wavelength 5π and the amplitude of 0.001.

The contours of coloring function for the disturbance created by the pull of the interface is shown in the Figure 60 at various times for the aspect ratio of 2. The interface is flat everywhere except near the center at the early stages of the Rayleigh-Taylor instability. The ripple spreads toward the side boundary at later stage. Oil comes from the center region and near the walls. The high density fluid goes down while light density fluid (oil) goes up forming the mushroom-like structure in oil near the center. The mushroom-like structure in the water is being distorted by the presence of the lower boundary, as shown in Figure 60f.

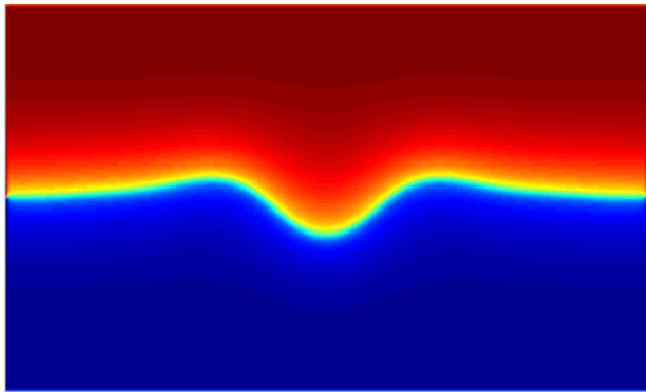
a) $t = 0.05 \text{ sec}$

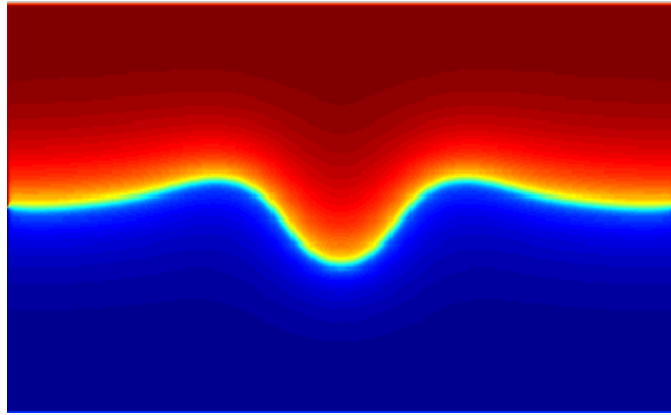


b) $t = 0.112 \text{ sec}$

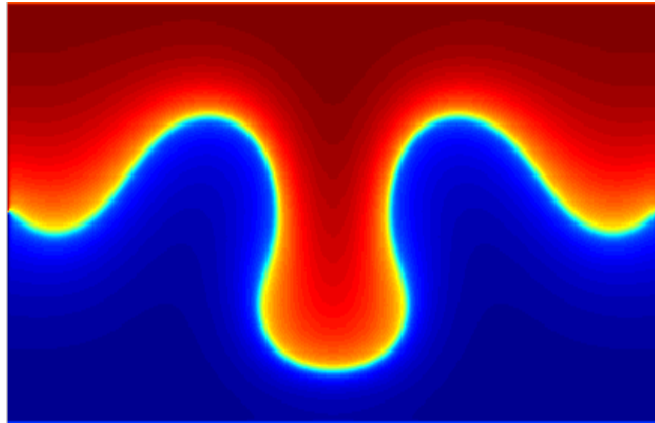


c) $t = 1.84 \text{ sec}$

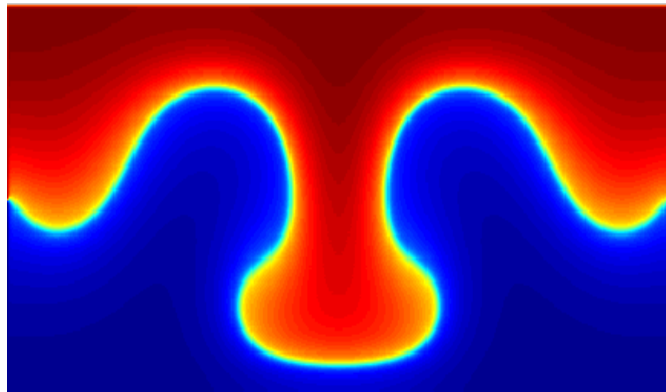




d) $t = 2.27$ sec



e) $t = 3.80$ sec

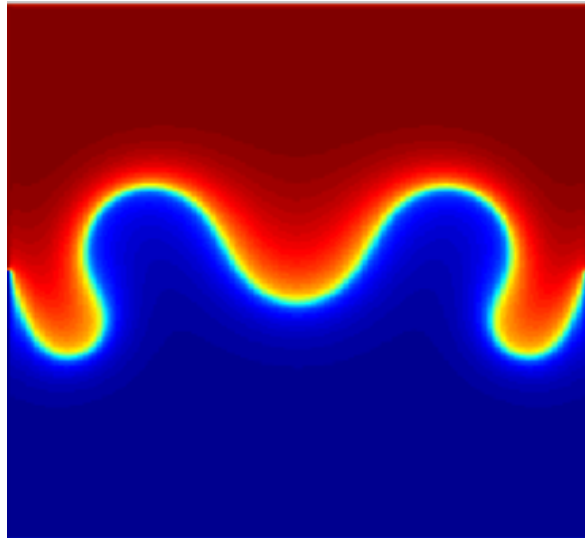


f) $t = 4.23$ sec

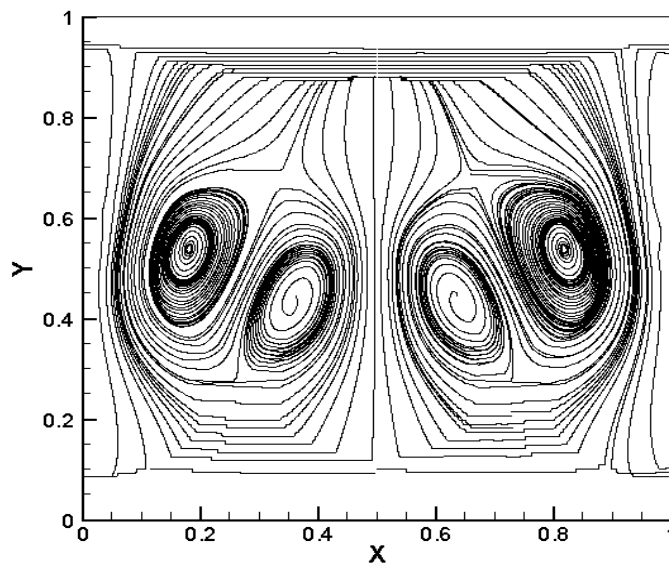
Figure 60. Density contours at various time. The dark blue color denotes oil while the dark red color denotes water. The initial disturbance is introduced by pulling of the interface.

The contours of coloring function and the streamlines at $t = 4.35$ sec and 5.3 sec are shown

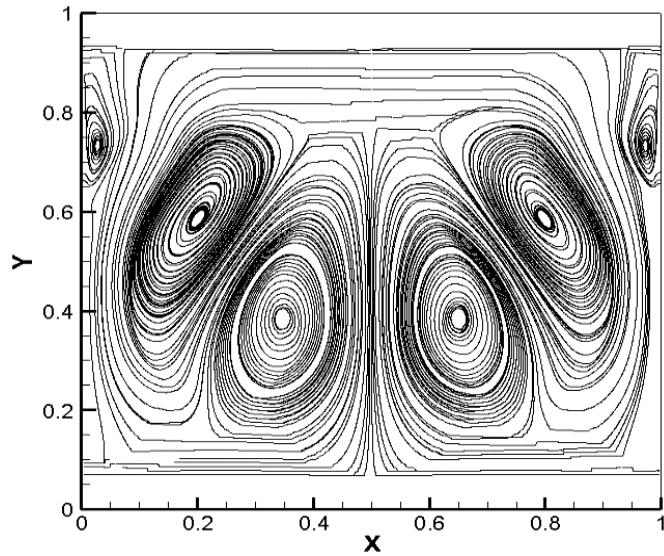
for aspect ratio of 1 in Figure 61. The flow created by the Taylor-Rayleigh instability is initiated near the interface by the sine wave with wavelength of $5L$. Images are obtained at very late stages of the instability. There are two pairs of counter-rotating vortices resulted from the Taylor-Rayleigh instability becomes larger and stronger as the instability grows. The vortices become larger as the time progress as shown in the Figure 61.



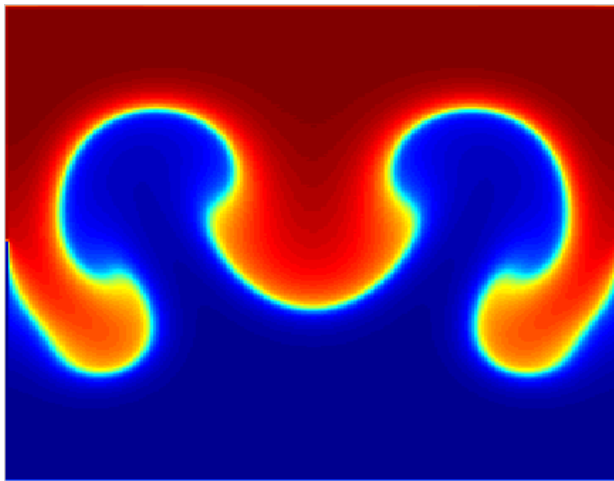
a) Density contour at $t = 4.35$ sec



b) Streamlines contour at $t = 4.35$ sec



c) Streamlines at $t = 5.3$ sec



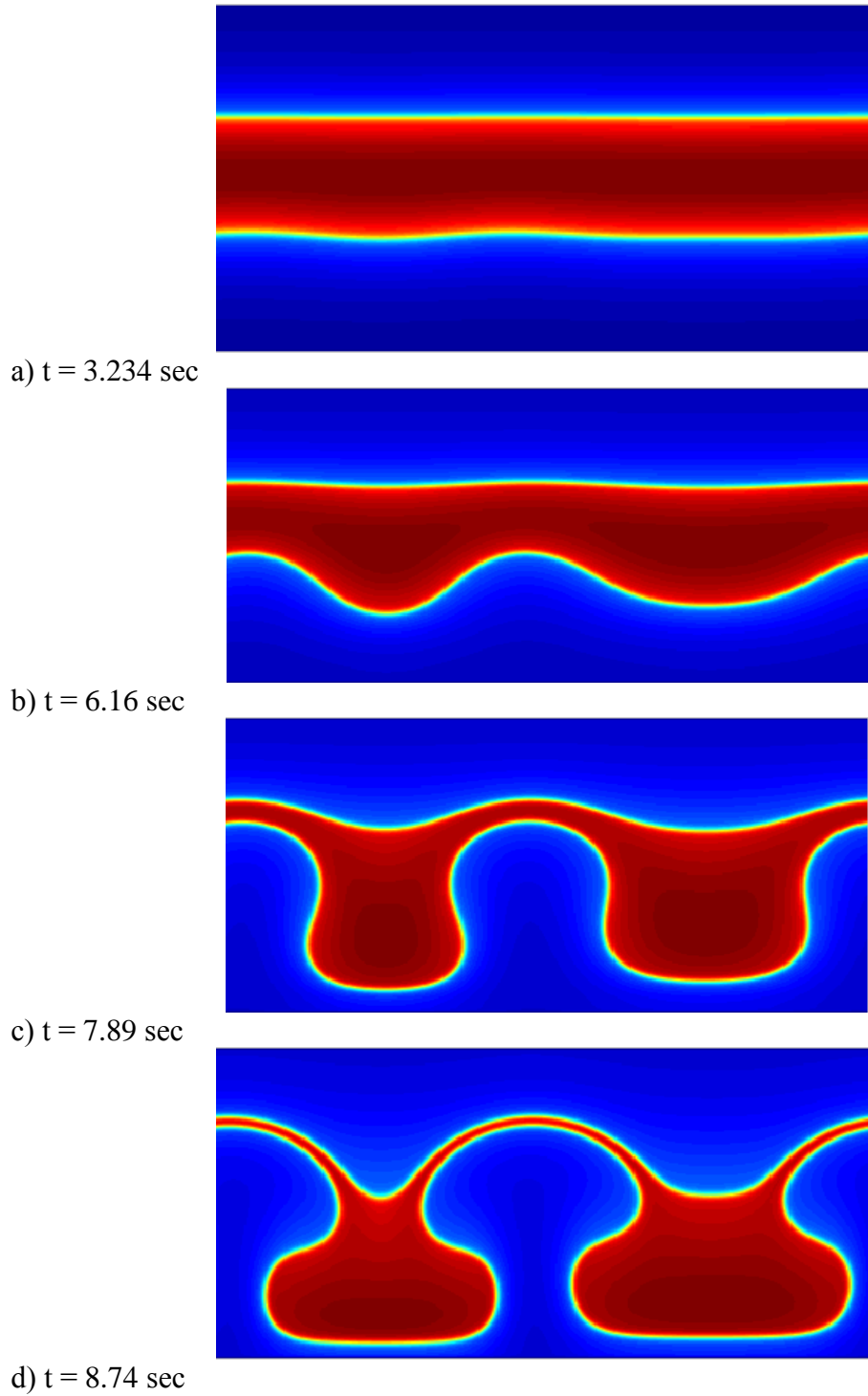
d) Density contour at $t = 5.3$ sec

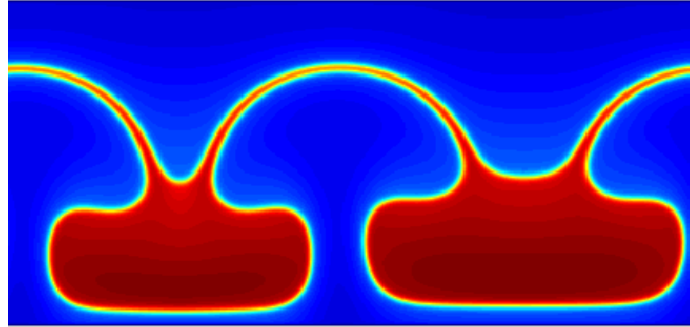
Figure 61. Density and streamlines contours at $t = 4.35$ sec and $t = 5.3$ sec. The dark blue color denotes oil (while the dark red color denotes water). The initial disturbance is periodic with the wavelength 5π and the amplitude of 0.001.

5.2.4. Three Layers with AR=2

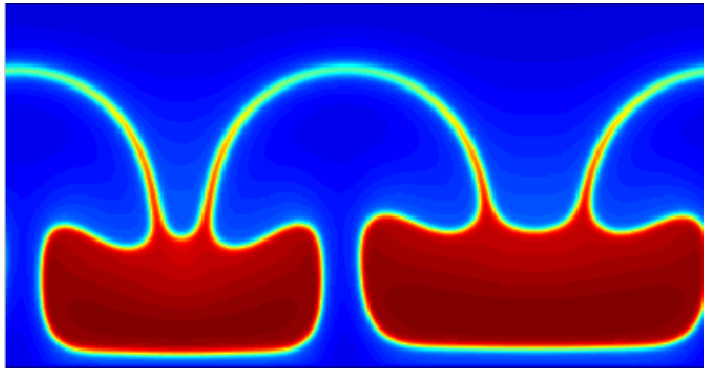
The three fluids are arranged in the certain way, the heavy fluid is placed in the middle and other two partitions are filled with the lighter fluid. The single mode disturbance is applied in the lower interface of the heavy fluid, as shown in Figure 62a [57]. The periodic

conditions are applied at the side walls. No effects of the sided wall boundaries are on the flow structures, as shown in Figure 62d.



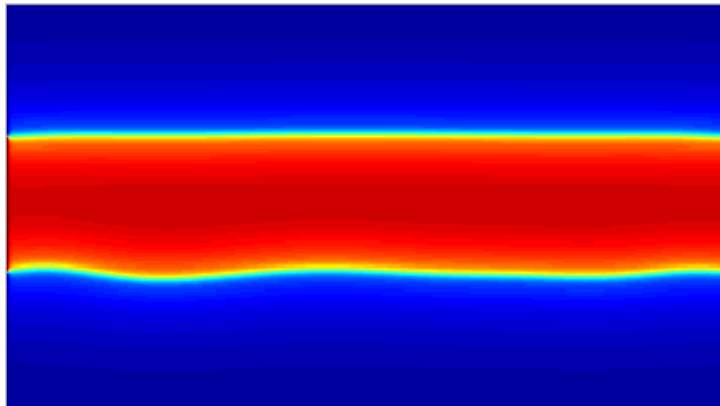


e) t = 9.11 sec

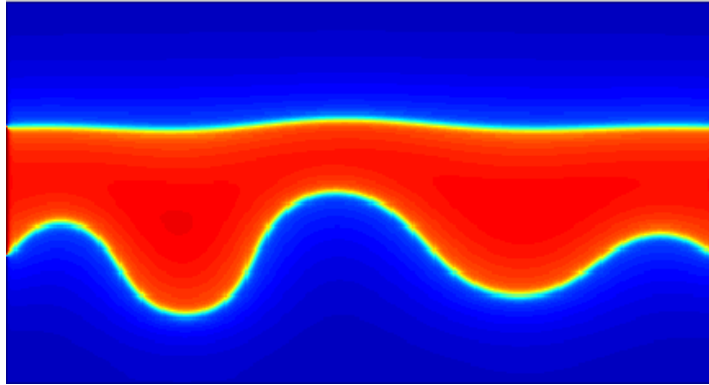


f) t = 9.45 sec

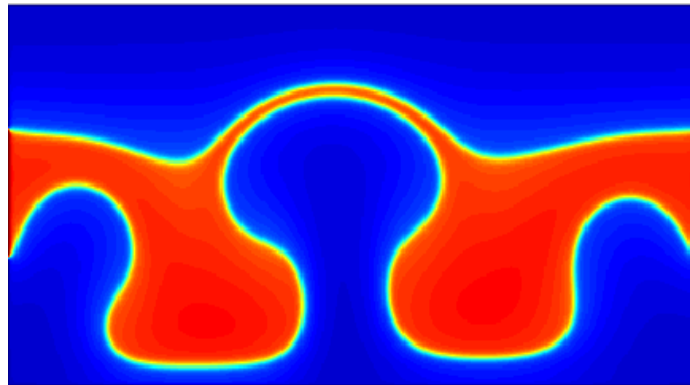
Figure 62. Density contours in three layers at various times. The lower interface is disturbed by the periodic disturbances of π wavelength and 0.001 amplitude. Periodic sided walls.



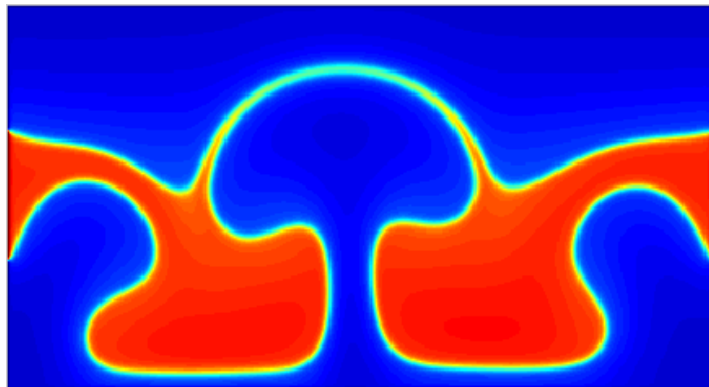
a) t = 3.00 sec



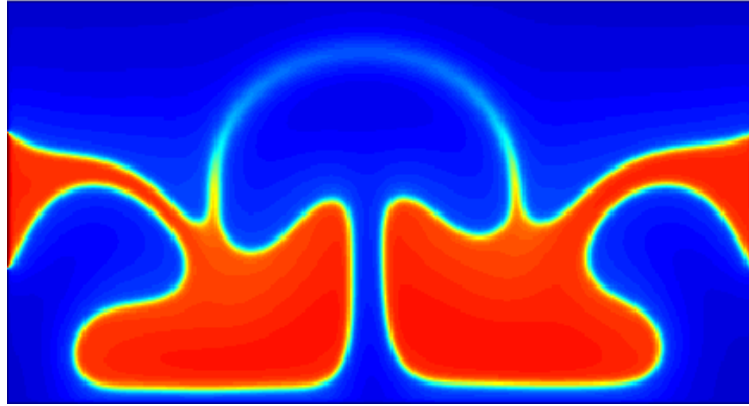
b) $t = 6.27$ sec



c) $t = 8.14$ sec



d) $t = 8.77$ sec



e) $t = 9.28$ sec

Figure 63. Density contours in three layers at various times. The lower interface is disturbed by the periodic disturbances of π wavelength and 0.001 amplitude. Periodic side walls.

The fluid structure behavior is completely different due to the effects of the boundary conditions in both sides, as shown in Figures 62 and 63. The lower interface is unstable; however, the upper interface is stable. At the late stage the upper interface becomes unstable as well. The wall boundary effects can be observed, as shown in Figure 62c and 63d. At the early stage the flow structure is dominated by the no-slip boundary effect. The mushroom structure appears due to the difference in thermo-physical properties of the two fluids. These results prove that LBM can trace the interface between the two fluids effectively.

5.3. Three Dimensional Interfacial Flows Using D3Q19- Multi-Components –Shan and Chen Model

5.3.1. Introduction

A three dimensional nineteen velocity, D3Q19, lattice Boltzmann model has been developed to study the evolution of the three-dimensional Rayleigh–Taylor instability. The geometry considered is $H \times H \times 6H$ cavity. The gravitational acceleration is acting in the direction of z . The heavier fluid, water, is placed above the lighter fluid, oil; creating unstable equilibrium. By introducing periodic disturbance the Rayleigh-Taylor instability onsets. The flows induced by the flow transition at the early and the late stage of the instability is characterized.

5.3.2. A Mathematical Model

There are several cubic lattice arrangements to study three dimensional flows. Fifteen velocity; D3Q15, and nineteen velocity; D3Q19 are the two of them [64-66]. These lattice arrangements are illustrated earlier in Table 1.3. At each physical location x , the D3Q19 models have a rest particle with zero velocity in the discretized velocity set $\{e_k\}$. The discretized lattice velocity is given by

$$e_k = \begin{cases} (0,0,0) & k = 0 \\ (\mp c, 0,0), (0, \pm c, 0), (0, \pm c, 0) & k = 1: 6 \\ (\pm c, \pm c, 0), (\pm c, 0, \pm c), (0, \pm c, \pm c) & k = 7: 18 \end{cases} \quad 108$$

Shan and Chen model has been employed to model a non–ideal interaction between particles at neighboring lattice nodes. A force at each site is employed to approximate the effects of the molecular interaction. This large–range force acting on the particle cause modification of the momentum calculation at each time step as

$$\rho^\sigma \mathbf{u}^\sigma = \sum_{\mathbf{k}} f_{\mathbf{k}}^\sigma(\mathbf{r}, t) \mathbf{e}_{\mathbf{k}} + \tau \sum_{\mathbf{k}} F_{\mathbf{k}}^\sigma(\mathbf{r}, t) \quad 109$$

where $F_{\mathbf{k}}$ is the interaction potential acting on the particles at site \mathbf{r} . It is modeled as

$$F_{\mathbf{k}}^\sigma(\mathbf{r}, t) = -G \overline{\psi^\sigma}(\mathbf{r}, t) \sum_{\mathbf{k}} \psi^\sigma(\mathbf{r} + \Delta \mathbf{r}, t + \delta t) w_{\mathbf{k}} \mathbf{e}_{\mathbf{k}} \quad 110$$

Here the potential strength $\psi(\mathbf{r}, t)$ is a function of fluid density and it plays a role of the effective density. G measures the strength of the interactions between particles on the nearest-neighbor grid site, $f(\mathbf{r}, t)$ is the single-particle distribution function or probability of σ component. The macroscopic velocity of σ is \mathbf{u}^σ , the relaxation time is τ and δt is the time step. The \mathbf{r} represents the three dimensional spatial coordinates $\mathbf{r} = (x, y, z)$ and \mathbf{u} denotes the velocity vector $\mathbf{u} = (u, v, w)$.

Although the total momentum is conserved over the entire domain, the momentum is not conserved locally within grid cells. By introducing an additional forcing term explicitly to the velocity field, the intermolecular interactions can effectively be modeled.

The diagonal matrix of MRT for D3Q19 lattice arrangement is written as

$$D = \text{diag}(0, S_1, S_2, 0, S_4, 0, S_4, S_9, S_2, S_1, S_9, S_9, S_{16}, S_{16}, S_{16}, S_9, S_9, S_9, S_9) \quad 111$$

The equilibria of the moments, m^{eq} , are the functions of the conserved moments, which are the mass density.

$$\begin{bmatrix} m_1^{eq} \\ m_2^{eq} \\ m_3^{eq} \\ m_4^{eq} \\ m_5^{eq} \\ m_6^{eq} \\ m_7^{eq} \\ m_8^{eq} \\ m_9^{eq} \\ m_{10}^{eq} \\ m_{11}^{eq} \\ m_{12}^{eq} \\ m_{13}^{eq} \\ m_{14}^{eq} \\ m_{15}^{eq} \\ m_{16}^{eq} \\ m_{17}^{eq} \\ m_{18}^{eq} \\ m_{19}^{eq} \end{bmatrix} = \begin{bmatrix} -11\Delta\rho + 19J_x J_x \\ \varphi_\epsilon \nabla \rho + \frac{\varphi_{\epsilon j}}{\rho_o} J_x J_x \\ 0 \\ -\frac{2}{3} J_{x,y,z} \\ 0 \\ -\frac{2}{3} J_{x,y,z} \\ m_6^{eq} \\ 0 \\ -\frac{2}{3} J_{x,y,z} \\ 1/\rho_o (3J_x^2 - J_x J_x) \\ \varphi_{xx} 1/\rho_o (3J_x^2 - J_x J_x) \\ 1/\rho_o (J_y^2 - J_z^2) \\ \varphi_{xx} 1/\rho_o (J_y^2 - J_z^2) \\ 1/\rho_o (J_x \cdot J_y) \\ 1/\rho_o (J_y \cdot J_z) \\ 1/\rho_o (J_z \cdot J_x) \\ 0 \\ 0 \\ 0 \\ 0 \end{bmatrix} \quad J=(J_x, J_y, J_z)=\rho_o \mathbf{u} \quad 112$$

The numerical stability of the model can be achieved by selecting $\varphi_\epsilon = \varphi_{xx} = 0$ and $\varphi_{\epsilon j} = -\frac{475}{63}$ [67]. The density fluctuation $\Delta\rho$ is utilized instead of the total density ρ in order to reduce the numerical instabilities due to the round-off error [67]. The viscosity per unit lattice for D3Q19 is defined as in equation (1).

The weighting functions of D3Q19 are:

$$w_k = \begin{cases} \frac{1}{3} & k = 0 \\ \frac{1}{18} & k = 1:6 \\ \frac{1}{36} & k = 7:18 \end{cases} \quad 113$$

The summation of the weighting function should be unity.

$$\sum_0^{18} w_k = 1 \quad 114$$

In our simulation, the values of the relaxation rates inside the diagonal matrix was chosen to be

$$S_1 = 1.19, S_2 = S_{10} = 1.4, S_4 = 1.2 \text{ and } S_{16} = 1.98, S_6 \text{ and } S_9 = \frac{1}{\tau} \quad 115$$

The momentum matrix M is

$$M = \begin{bmatrix} 1 & 1 & 1 & 1 & 1 & 1 & 1 & 1 & 1 & 1 & 1 & 1 & 1 & 1 & 1 \\ -30 & -11 & -11 & -11 & -11 & -11 & 8 & 8 & 8 & 8 & 8 & 8 & 8 & 8 & 8 \\ 12 & -4 & -4 & -4 & -4 & -4 & 1 & 1 & 1 & 1 & 1 & 1 & 1 & 1 & 1 \\ 0 & 1 & -1 & 0 & 0 & 0 & 1 & 1 & -1 & 1 & -1 & 1 & -1 & 0 & 0 \\ 0 & -4 & 4 & 0 & 0 & 0 & 1 & 1 & -1 & 1 & -1 & 1 & -1 & 0 & 0 \\ 0 & 0 & 0 & 1 & 0 & 0 & 1 & 1 & 1 & -1 & -1 & 0 & 0 & 1 & -1 \\ 0 & 0 & 0 & -4 & 0 & 0 & 1 & 1 & 1 & -1 & 0 & 0 & 0 & 1 & -1 \\ 0 & 0 & 0 & 0 & 1 & -1 & 0 & 0 & 0 & 0 & 1 & 1 & -1 & 1 & -1 \\ 0 & 0 & 0 & 0 & -4 & 4 & 0 & 0 & 0 & 0 & 1 & 1 & -1 & 1 & -1 \\ 0 & 2 & 2 & -1 & -1 & -1 & 1 & 1 & 1 & 1 & 1 & 1 & -2 & -2 & -2 \\ 0 & -4 & -4 & 2 & 2 & 2 & 1 & 1 & 1 & 1 & 1 & 1 & -2 & -2 & -2 \\ 0 & 0 & 0 & 1 & -1 & -1 & 1 & 1 & 1 & 1 & -1 & -1 & -1 & 0 & 0 \\ 0 & 0 & 0 & -2 & -2 & 2 & 1 & 1 & 1 & 1 & -1 & -1 & -1 & 0 & 0 \\ 0 & 0 & 0 & 0 & 0 & 0 & 1 & 1 & -1 & -1 & 1 & 0 & 0 & 0 & 0 \\ 0 & 0 & 0 & 0 & 0 & 0 & 0 & 0 & 0 & 0 & 0 & 0 & 0 & 1 & -1 \\ 0 & 0 & 0 & 0 & 0 & 0 & 0 & 0 & 0 & 0 & 0 & 0 & 0 & 1 & -1 \\ 0 & 0 & 0 & 0 & 0 & 0 & 0 & 0 & 0 & 0 & 0 & 0 & 0 & 0 & 0 \\ 0 & 0 & 0 & 0 & 0 & 0 & 1 & 1 & -1 & -1 & -1 & 1 & -1 & 0 & 0 \\ 0 & 0 & 0 & 0 & 0 & 0 & -1 & -1 & -1 & -1 & 1 & 0 & 0 & 1 & -1 \\ 0 & 0 & 0 & 0 & 0 & 0 & 0 & 0 & 0 & 0 & 0 & 1 & -1 & -1 & 1 \end{bmatrix} \quad 116$$

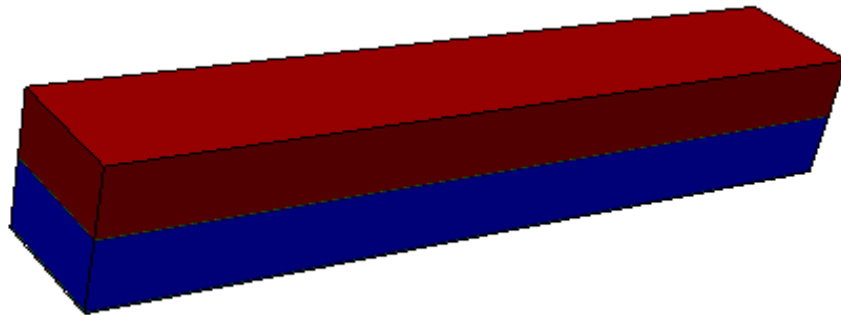
The resulting discretized lattice Boltzmann equation is

$$f_{\mathbf{k}}^{\sigma}(\mathbf{r} + \mathbf{e}_{\mathbf{k}}\delta_t, t + \delta_t) - f_{\mathbf{k}}^{\sigma}(\mathbf{r}, t) = -M^{-1\sigma}D^{\sigma}[m_{\mathbf{k}}^{\sigma}(\mathbf{r}, t) - m_{\mathbf{k}}^{\sigma\text{eq}}(\mathbf{r}, t)] \quad 117$$

5.4.3. Results and Discussions

Three dimensional flows created by the Rayleigh –Taylor instability is presented for various types of boundary conditions. The heavier fluid is placed at the top while the lighter fluid at the bottom. The simulation is carried out for the time step of 1.0×10^{-3} sec. Shan and Chen model has been employed to treat the interactive forces between the phases. The aspect ratio is $AR = L/H = 6$, where L is the length and H is the height of the rectangular cavity. The width of the three dimensional cavity is $W=H$. In an infinite medium (periodic

boundary conditions) flow patterns are nearly periodic in x-direction, as shown in Figures 64 and 65 for $Ra = 1 \times 10^5$. Slight distortion in the flow patterns is due to the nature of the initial periodic disturbance (sine wave disturbance). At the late stage of the instability the mushroom-like structure are formed. These mushrooms like structure are distorted significantly by the presence of the top and the bottom slip surface. Slices of the three dimensional flow patterns in the x-z plane are depicted in Figure 65 at various stages of the Rayleigh –Taylor instabilities. Figures 66 illustrates the velocity vectors of the x-z plane at $t = 1.1$ sec and $t = 2.1$ sec. Flow induced by the Rayleigh-Taylor instability becomes stronger at the later stage of the flow transition, as seen in Figure 67a and 67b. Figure 68 depicts the density contours for $Ra = 1 \times 10^5$ at various times of a narrow channel. The no-slip walls influence the flow patterns at both early and late stages of the flow instabilities. The interface starts deforming near the side walls and stay nearly flat away from the side walls at the early stage. The flow patterns becomes very complicated by the influence of side and the top and the bottom walls at the later stage of the instabilities. The intensity of flow increases and spatial flow structures become significantly more complicated at later stage of the instability, as shown in Figure 69a and b.



a)

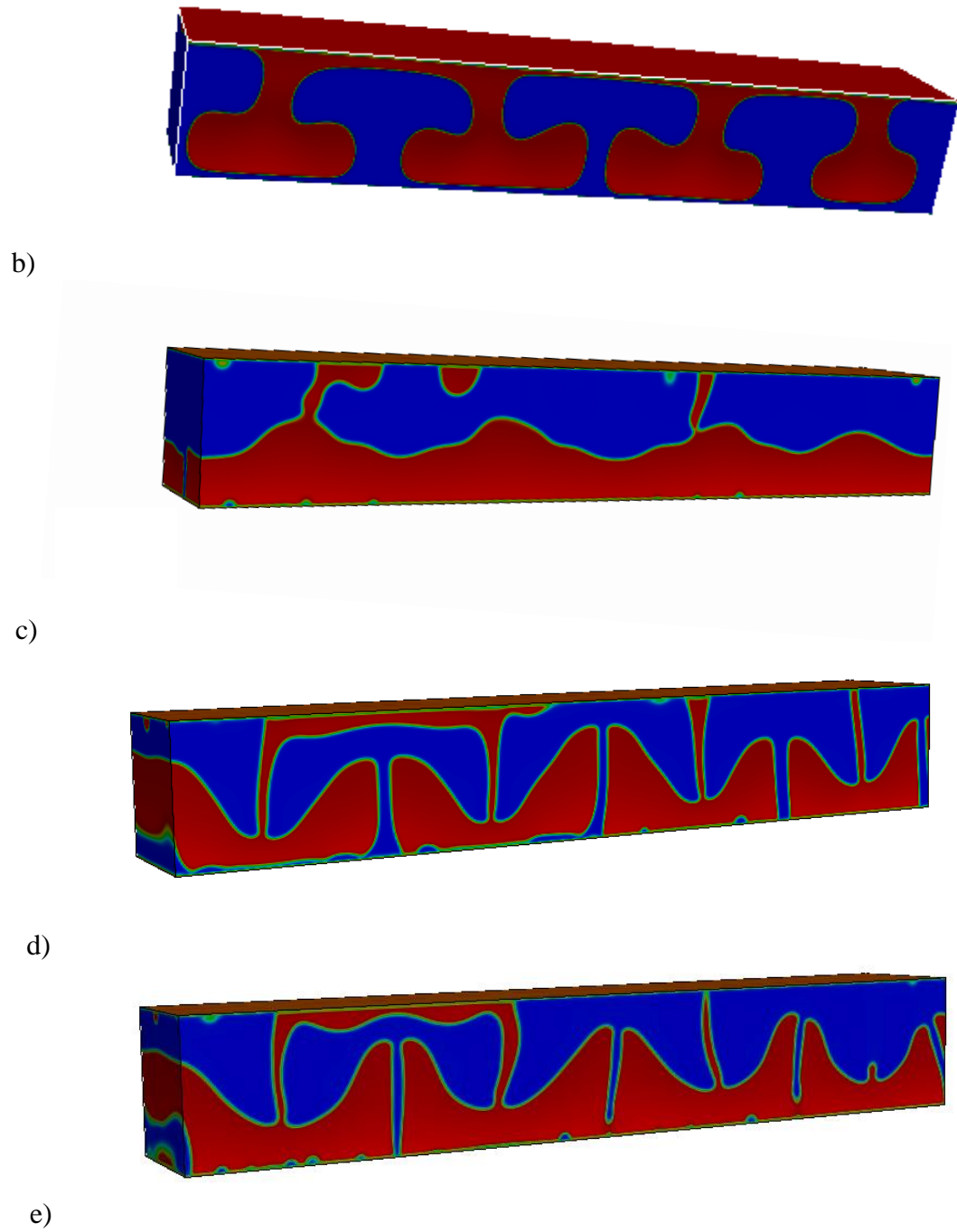
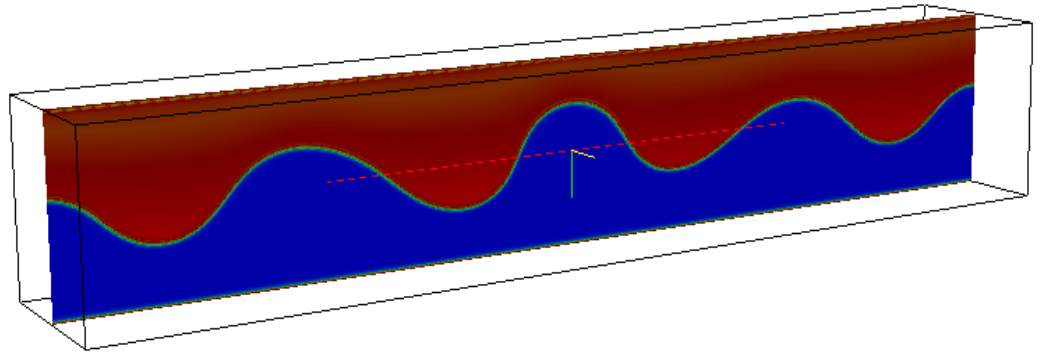
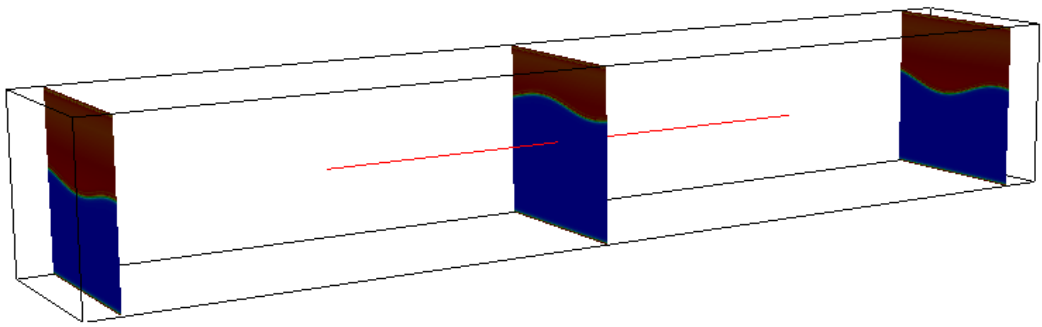


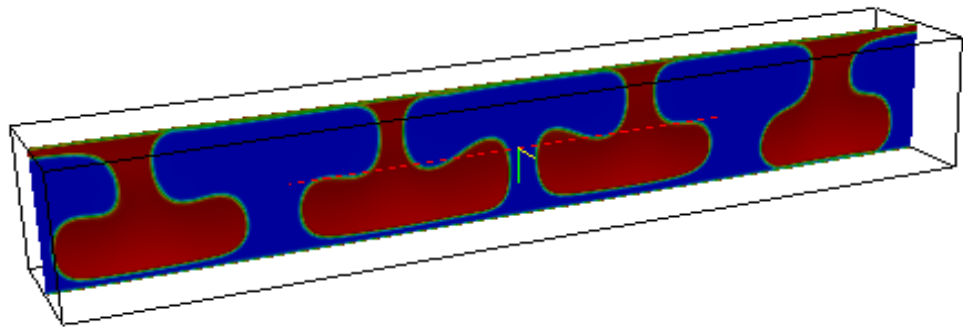
Figure 64. Three Dimensional density iso surfaces at a) $t = 0$ sec, b) $t = 1.2$ sec. c) $t = 1.85$ sec d) $t = 2.13$ sec, and f) $t = 2.41$ sec. Simulations are conducted for $AR=5$ with periodic boundary conditions.



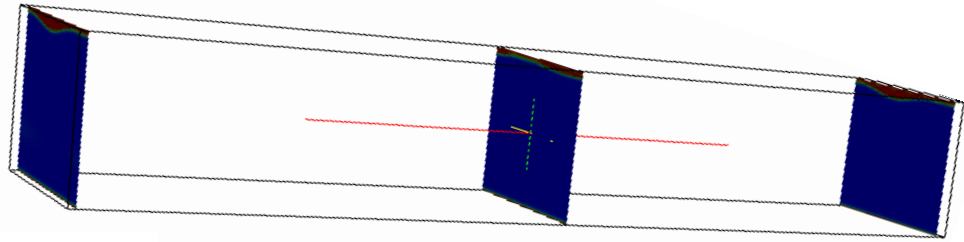
a)



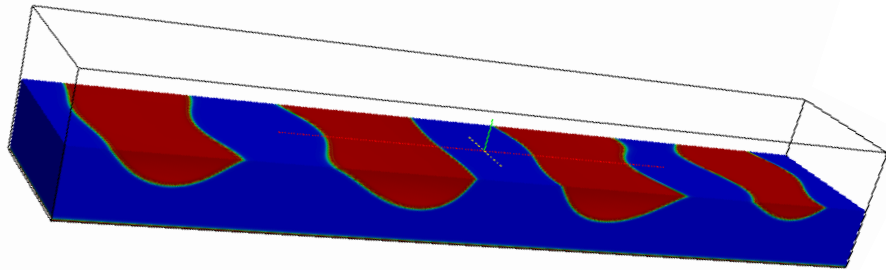
b)



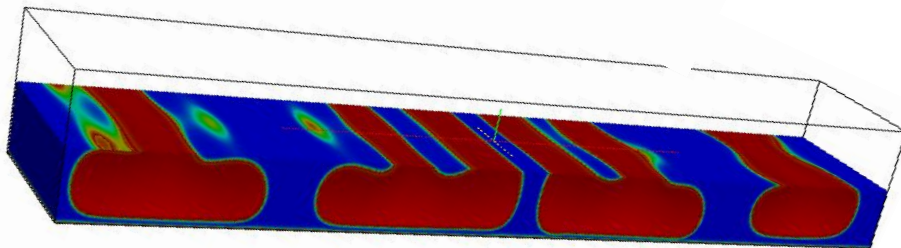
c)



d)

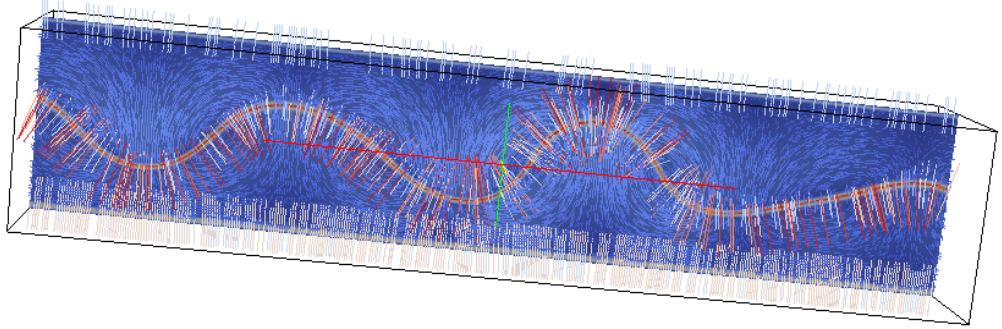


e)

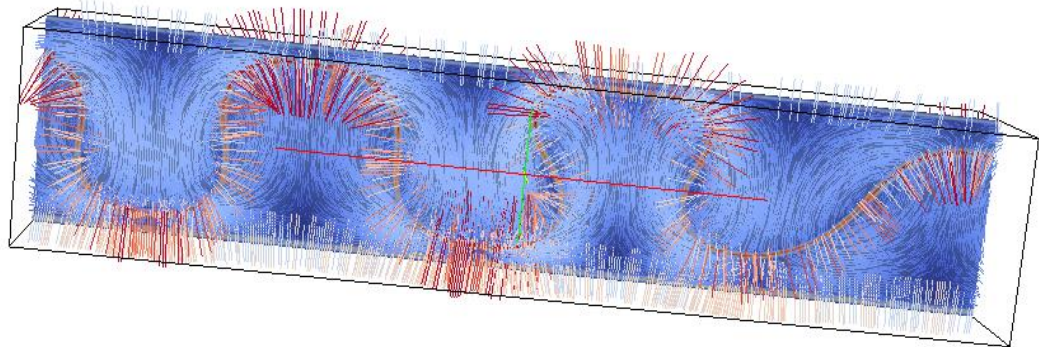


f)

Figure 65. Three dimensional density iso surfaces: a) The slice in the y-z plane at $t = 0.98$ sec, b) the slice in the x-z plane at $t = 0.98$ sec, c) the slice in the y-z plane at $t = 1.20$ sec, d) the slice in the x-z plane at $t = 1.20$ sec, e) and f) the half of the domain in the x-y plane at $t = 0.98$ sec and 1.20 sec, respectively.

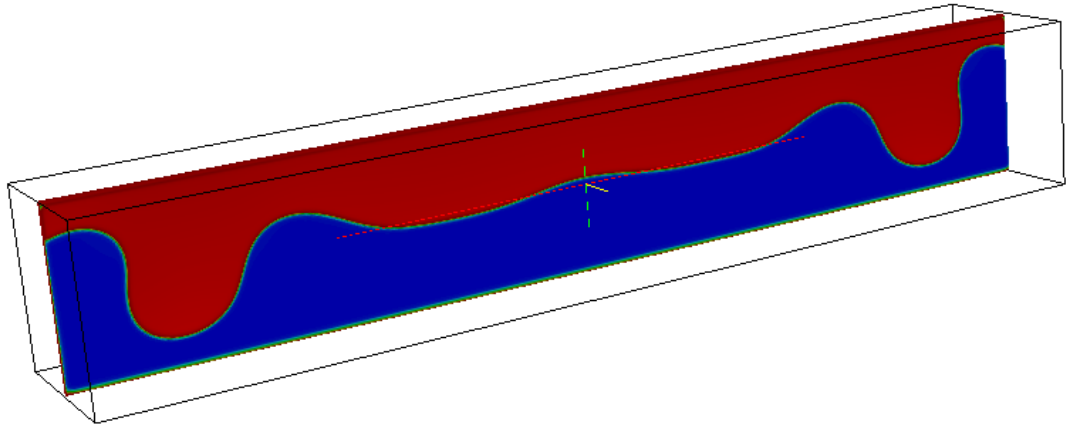


a)

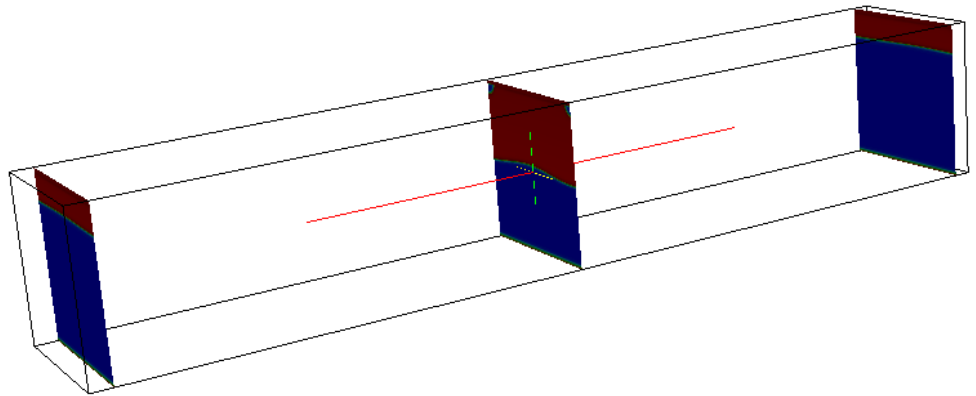


b)

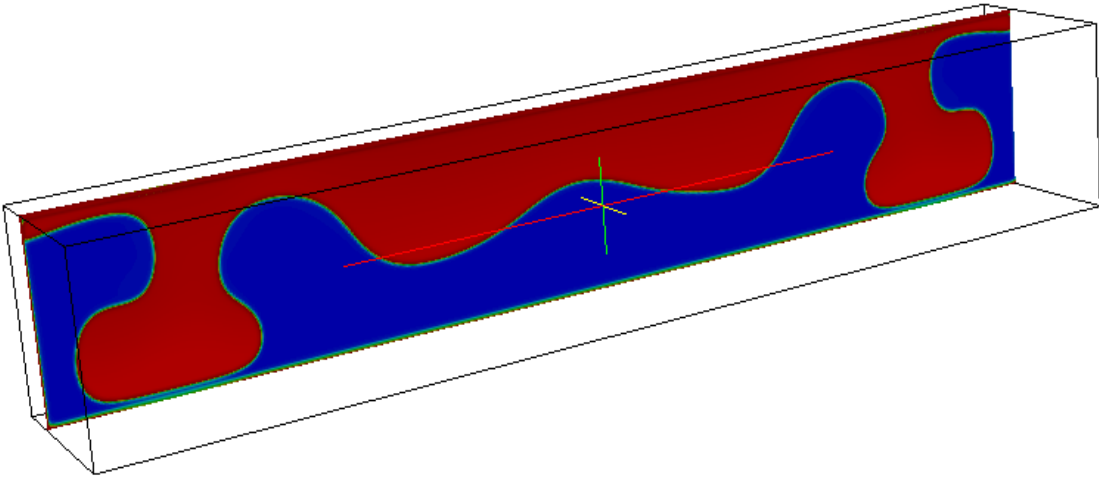
Figure 66. Velocity vectors in the x-z plane at a) $t = 1.1$ sec and b) $t = 2.1$ sec. Periodic boundary conditions are applied at the side walls.



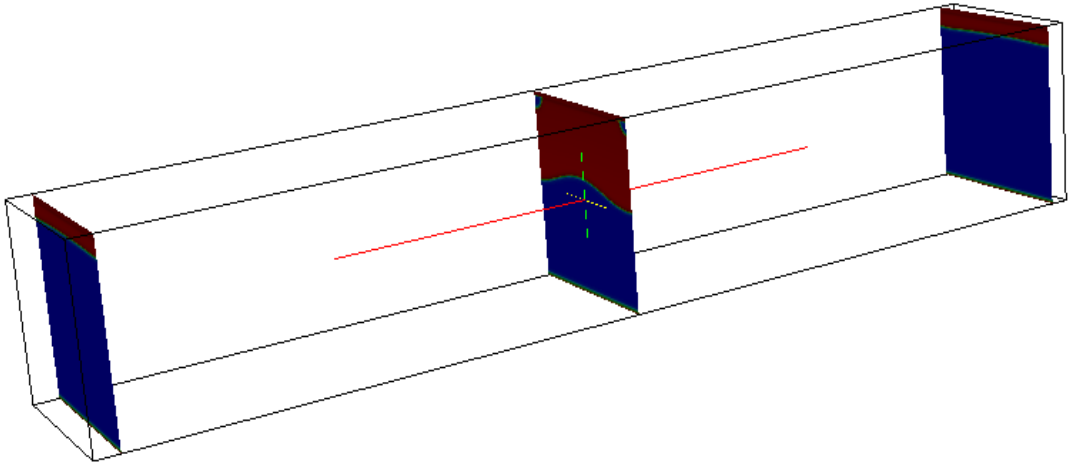
a)



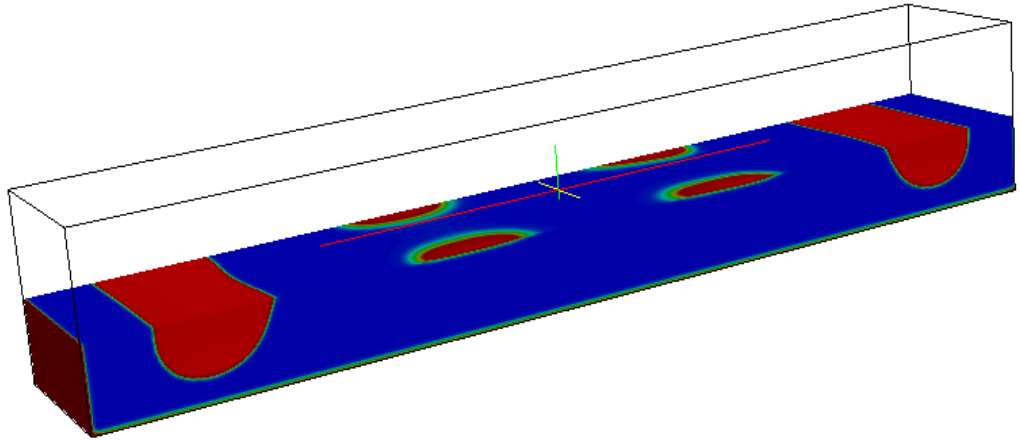
b)



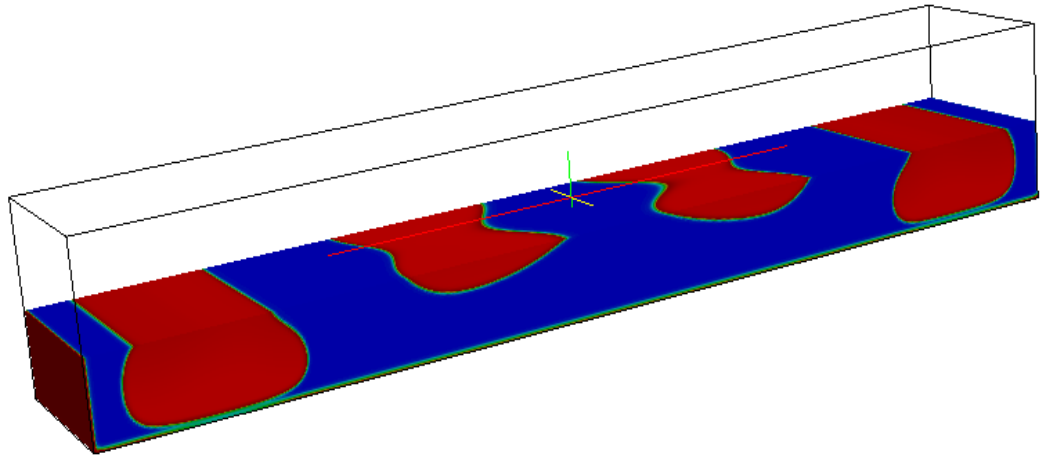
c)



d)



e)



f)

Figure 67. The density iso surfaces: a) The slice in the y- z-plane at $t = 0.98$ sec, b) the slice in the x-z plane at $t = 0.98$ sec, c) the slice in the y-z plane at $t = 1.20$ sec, and d) the slice in x-z plane at $t = 1.20$ sec. e) and f) The density iso surfaces in the half of the domain in z-plane at $t = 0.98$ sec and $t = 1.20$ sec, respectively. The no-slip boundary conditions are applied at the side walls.

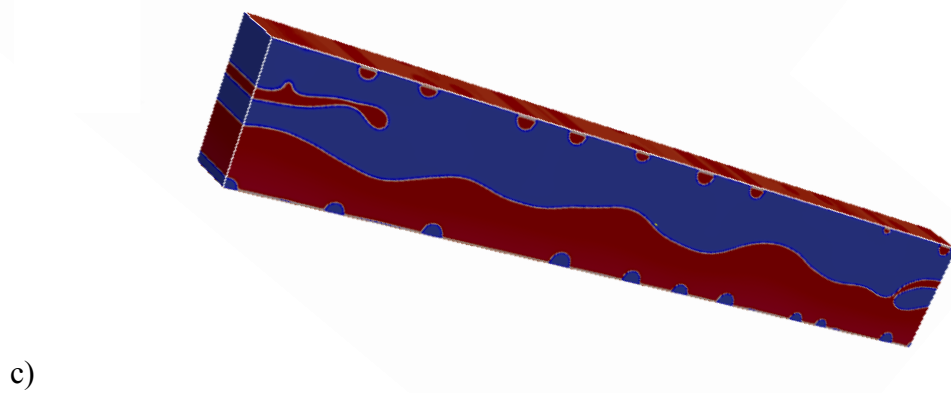
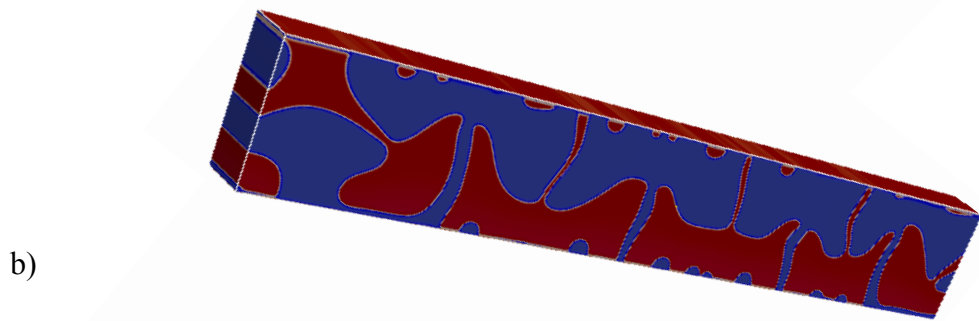
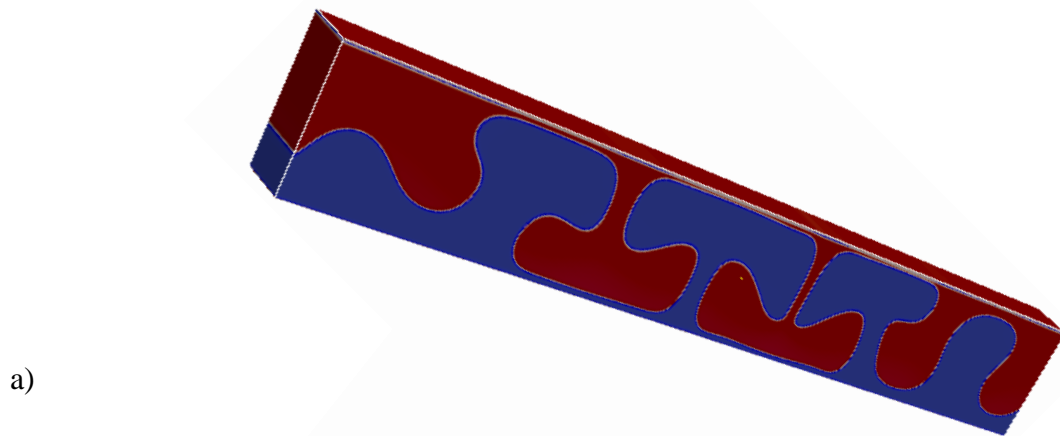
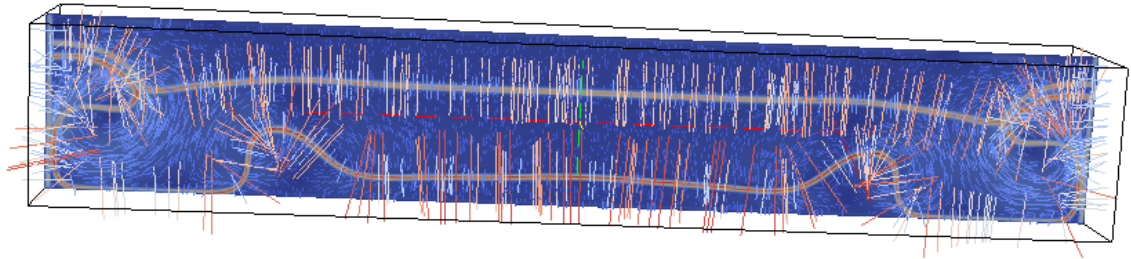
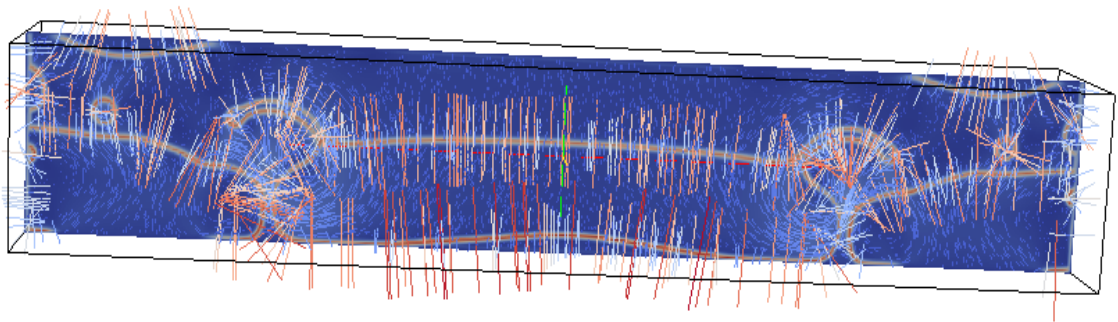


Figure 68. The density iso surfaces at a) at $t = 0$, b) $t = 1.85$ sec, c) $t = 2.13$ sec and d) $t = 2.41$ sec. Simulations are conducted for $AR=5$ with periodic boundary conditions at the side walls of a narrow channel.



a)



b)

Figure 69. Velocity vectors in the x-z plane at a) $t = 1.1$ sec and b) $t = 2.1$ sec. No-slip boundary conditions are applied at the side walls.

5.4. The effect of the Interactive Strength “G” and Limitations of Shan & Chen Model

Note that the surface tension and the equation of state depend on the same parameter G , which is clearly a limitation of the Shan-Chen model [68]. Therefore, by taking a larger parameter G the liquid-liquid density ratio is not only increased, as shown in Figure 70, but also the interface width is decreased because of the larger surface tension. This is one reason for the stability failure with the large G parameter. As the interface is narrowed the scheme fails due to large density gradients. Sbragaglia et al. (2007) introduced the multirange potential to separate the equation of state and the surface tension [69]. However, it is not compliant with the Navier-Stokes surface tension term. One can see the difference between the profiles as G increases. However, the equation of state makes the density value to be almost the same as in the original Shan-Chen model.

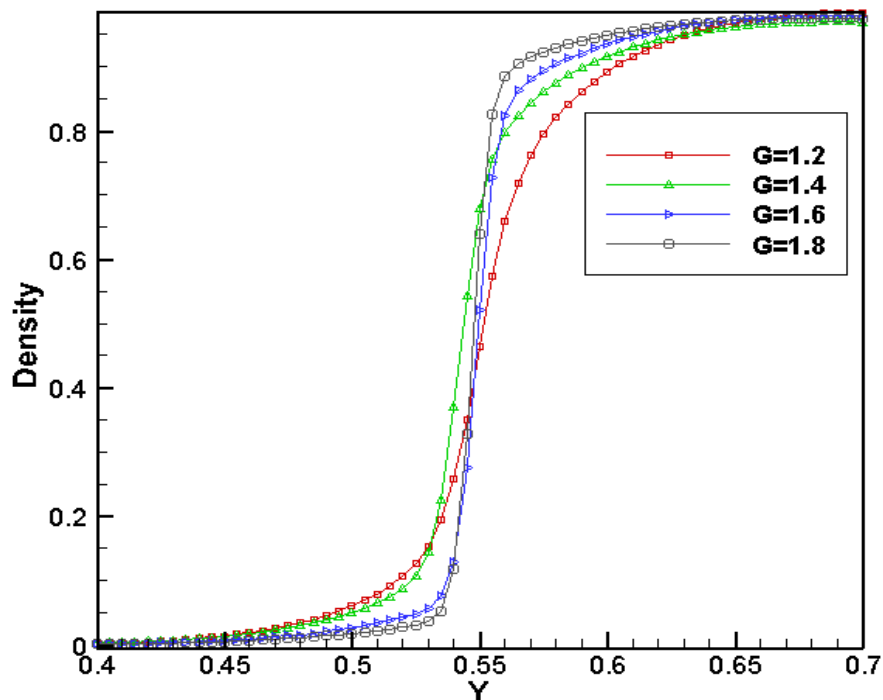


Figure 70. Density profiles for various values of “G” at the interface at $t = 0.46$ sec.

The interface width decreases with increase of the liquid-liquid density as G increases.

Figure 71 illustrates the pressure profiles at the interface and shows that if G increases the pressure at the interface decreases. Relationship between the pressure field and G is expressed as follows

$$P = c^2_s \rho - \frac{G}{6} (\psi(\rho))^2 \quad 118$$

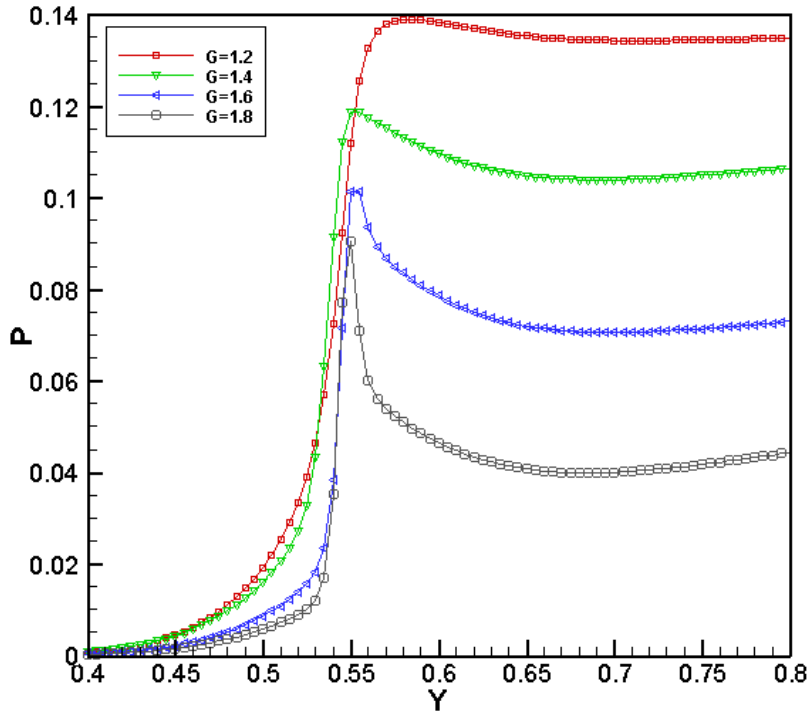


Figure 71. Pressure profiles across the interface for various values of “G” at t = 0.46 sec.

The relaxation frequency has strong effect on the density gradient across the interface. Selecting appropriate relaxation frequency is an important factor to keep the code stable. When the relaxation frequency $0.5 \leq \omega \leq 1.1$, the present simulations provide stable results. As the relaxation frequency increases, the density gradient across the interface increases, as shown in Figure72. Stif density distribution across the interface leads to the instability.

Figure 73 shows the Mach number (Ma) for various values of G. For stable and accurate simulations Ma should be small. As G increases Ma increases, as shown in Figure 73.

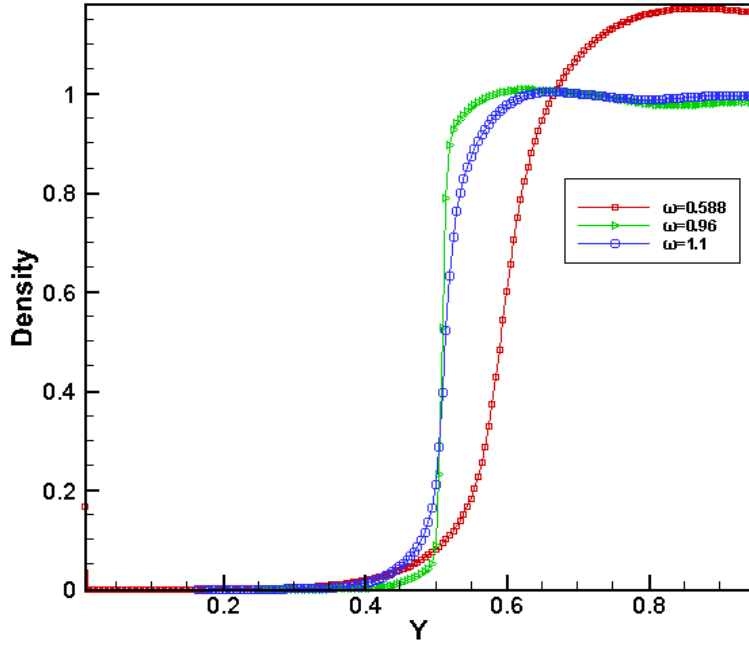


Figure 72. Density profiles across the interface for various values of the relaxation frequencies and $G = 1.2$ at $t = 0.46$ sec.

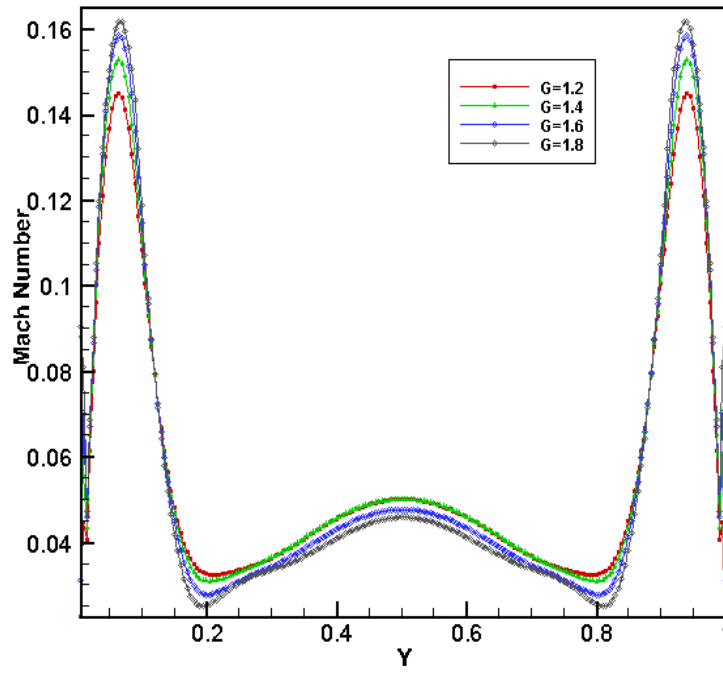


Figure 73. Mach number profiles across the interface for various values of “G” at $t = 0.46$ sec.

In summary, multi-phase multi relaxation lattice Boltzmann method have been developed to study two and three dimensions interfacial flows. Flow field induced by rising droplets in confined geometry are examined. The dynamics of the interface separating two fluids have been characterized for various geometry. Flows induced by Rayleigh–Taylor instability are examined at the linear and nonlinear stage of the instability. Dynamics of the interface is studied in confined geometry near walls.

CHAPTER 6: CONCLUSIONS

A detailed description of a single relaxation time lattice Boltzmann model and its variations has been presented. Implementation of various types of velocity and thermal boundary conditions was discussed. Extension of interactive forces between phases and the surface tension for modeling interfacial flows was described in detail for various methods. Stability of lattice Boltzmann model has been improved significantly by adopting a multi-relaxation and regularized model. A novel regularized multi relaxation lattice Boltzmann model has been proposed by the present author to overcome the stable shortcomings of the lattice Boltzmann model. The new model has been successfully applied to turbulent flows past bluff bodies at high Re to resolve spatial and temporal characteristics of the flow in the wake. Thermal lattice Boltzmann model has been developed to study flows induced by the density stratifications.

Unsteady turbulent flow around a square and arrays of square cylinders confined in a channel were studied computationally by employing regularized multi-relaxation lattice Boltzmann method. Spatial and temporal characteristics of the flow created by vortex shedding were examined for Re up to 21400. The frequency of the vortex shedding predicted here agrees well with the results measured and predicted by large eddy simulations for a wide range of Re . Flow field in the wake near body is similar to those observed and predicted by large eddy simulations. Vortices shed by the bluff body interact strongly with the boundaries away from the body, in the more confined case. It is also noticed that, for flows past an array of cylinders, multiple frequencies are seen in the power spectrum of the lift coefficient. This implies that the complexity of the vortex growth and the shedding from cylinders is greater than in the single cylinder case. It is observed even

for the first row of the arrayed cylinder. This study clearly demonstrates that the lattice Boltzmann method developed here overcomes the stability issues of the lattice Boltzmann method for high Re flows up to $Re=21400$. One of the advantages of the method developed here is orders of magnitude lower computation time when compared with large eddy simulations or direct numerical simulations.

Multi-Relaxation Time Lattice Boltzmann method was implemented to study lighter droplets rising in a heavier fluid. Both an infinite and bounded fluid domains were considered. Density distribution functions for each fluid and the function for the coloring step to identify the location of interface separating each immiscible fluid was determined at various stages. The evolution of the rising droplet and the temporal and spatial characteristics of the flow induced by such motion were examined for various arrangements. The present method was validated by comparing our results against well-known regimes in droplet dynamics. Interactions between multiple droplets and the interactions between droplets and a solid boundary were illustrated. These interactions create a complicated velocity, vorticity and the pressure field in the vicinity of rising droplets. It is also illustrated here how droplets rise when they are placed on the no-slip boundary initially. First, droplets from a long thin filament and at a later stage of evolution the filament breaks and droplet dis-attach from the boundary. As the residue of the droplet spreads over the no-slip surface dis-attached droplet continue to rise away from the surface. This study proves that Lattice Boltzmann method could be an effective computational fluid dynamics (CFD) tool to simulate multi-phase flows with interfaces evolving with complex fashion.

Multi-Relaxation Time Lattice Boltzmann Method with D2Q9 lattice arrangement has been employed to study the nonlinear dynamics of the Rayleigh Taylor instabilities in confined geometries. The expected mushroom structures, which are well documented in Rayleigh Taylor studies, are distorted by the choice of initial disturbances and by the effects of boundary walls. A growing ripple at the interface can be seen in the case of the non-periodic initial disturbance. Streamlines at various times show that the circulation begins around the interfaces and rapidly grows outward in time. The odd angles of the circulations again indicate the effect of the no slip boundaries. It is demonstrated that the Lattice Boltzmann method is efficient at handling complex interfacial flows manifested by flow transitions such as the one discussed here. Both linear and nonlinear stages of the instabilities can be captured accurately near and away from boundaries.

A three dimensional nineteen velocity, D3Q19, multi relaxation lattice Boltzmann model has been developed to study the nonlinear dynamics of the Rayleigh Taylor instabilities in a three dimensional cavity. Early and late stages of three dimensional Rayleigh Taylor instabilities were characterized.

Multi-relaxation thermal lattice Boltzmann model has been developed to study buoyancy-driven convections. Convection cells in a closure with a presence of no-slip surfaces were characterized. The results presented here agree well with those documented in the literature for classical flow patterns manifested by Rayleigh Benard instabilities.

It has been shown that the lattice Boltzmann method is an effective computational fluid dynamics tool. It can be an alternative to direct numerical simulations in resolving spatial and temporal structure of turbulent flows. It is also shown that the lattice Boltzmann method is a great tool to study the interfacial flows.

Stability of lattice Boltzmann method can be further improved by implementing Entropy lattice Boltzmann model to study high speed flows. The model can be made more flexible by introducing different lattice arrangements. Triangular, hexagonal or other placement of lattices in the computational domain can make model easily applied to solve flows in complex geometries.

APPENDIX A

A. Unknown and Known Distribution Functions for D3Q19 Arrangement.

A1. No-slip boundary Conditions

y-z plane

$f_5, f_{11}, f_{12}, f_{15}, f_{17}$

y-z plane:

$f_6, f_{13}, f_{14}, f_{16},$ and f_{18}

A. Left and right boundary conditions:

x-y plane:

$f_3, f_7, f_9, f_{15},$ and f_{16}

x-y plane:

$f_4, f_8, f_{10}, f_{17},$ and f_{18}

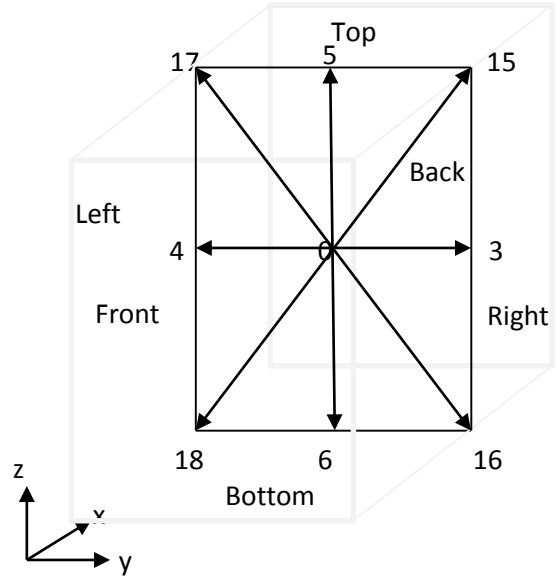


Figure A.1. Distribution functions in the y – z plane

B. Front and back boundary conditions:

x-z plane :

$f_2, f_9, f_{10}, f_{12},$ and f_{14}

x-z plane:

$f_1, f_7, f_8, f_{11},$ and f_{13}

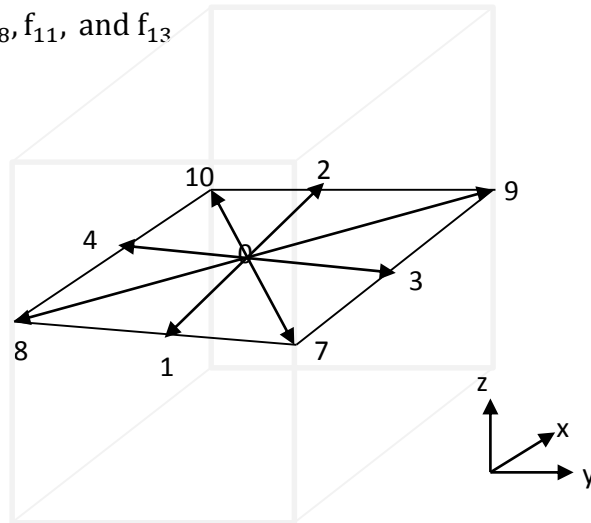


Figure A.2. Distribution functions in the x-y plane

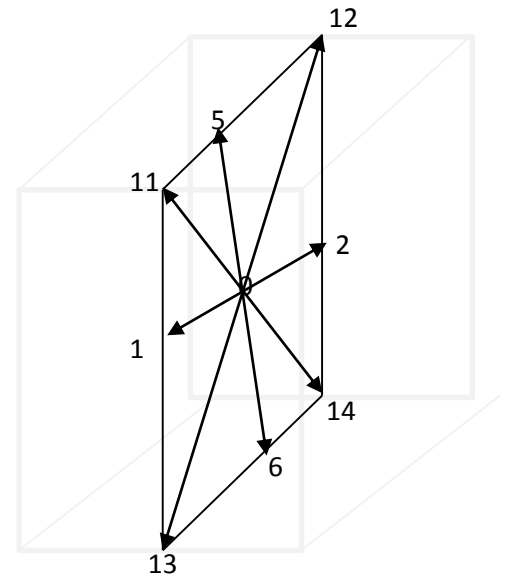


Figure A.3. Distribution functions in the x-z plane

To summarize all known and unknown distribution functions as follow:

At X=0 (Front wall)		At X=1 (Back wall)	
Unknown distribution functions	Known distribution functions	Unknown s distribution functions	Known distribution functions
f_2	f_1	f_1	f_2
f_9	f_8	f_8	f_9
f_{10}	f_7	f_7	f_{10}
f_{12}	f_{13}	f_{13}	f_{12}
f_{14}	f_{11}	f_{11}	f_{14}

Table 1.10 Distribution functions at the front and the back walls.

At Y=0 (left)		At Y=1	
Unknown distribution functions	Known distribution functions	Unknown s distribution functions	Known distribution functions
f_{15}	f_{18}	f_{18}	f_{15}
f_3	f_4	f_4	f_3
f_{16}	f_{17}	f_{17}	f_{16}
f_7	f_{10}	f_{10}	f_7
f_9	f_8	f_8	f_9

At Z=0		At Z=1	
Unknown distribution functions	Known distribution functions	Unknown distribution functions	Known distribution functions
f_{11}	f_{14}	f_{14}	f_{11}
f_{12}	f_{13}	f_{13}	f_{12}
f_5	f_6	f_6	f_5
f_{15}	f_{18}	f_{18}	f_{15}
f_{17}	f_{16}	f_{16}	f_{17}

Table 1.11. Distribution functions at the left and the right walls.

In order to determine five unknown distribution functions at the boundaries listed in Table A.1.10 and A.1.11 following five equations are used

$$\rho = \sum_{k=0}^{18} f_k \quad (1)$$

$$\rho u = \sum_{k=0}^{18} f_k c_{xk} \quad (2)$$

$$\rho v = \sum_{k=0}^{18} f_k c_{yk} \quad (3)$$

$$\rho w = \sum_{k=0}^{18} f_k c_{zk} \quad (4)$$

$$f_i - f_i^{eq} = f_{i+1} - f_{i+1}^{eq} \quad (\text{where } i = 5 \text{ and } 12) \quad (5)$$

Coupled linear set of equations (1-5), can be solved to determine the unknown distribution functions along the boundary.

A.2. Reflection Boundary Conditions

Simple reflection boundary conditions employ dummy nodes located near the walls to evaluate distribution functions at the boundary. A fluid domain particle colliding with boundary site reserves the direction of its velocity. The particle distribution functions locally can be determined from

$$f_k^{\text{out}}(\mathbf{r}, t) = f_k^{\text{in}}(\mathbf{r}, t) \quad (6)$$

where $f_k^{\text{in}}(\mathbf{r}, t)$ is the particle distribution function entering the boundary site and $f_k^{\text{out}}(\mathbf{r}, t)$ is the particle distribution function leaving the boundary site. The distribution functions can be re-written as listed in Table A1.1 and A1.2. On a boundary site, the mass and the momentum are conserved and the velocity on the boundary site is zero. Any particle entering the site with a given velocity leaves the boundary with the same velocity in the opposite direction. In case of the reflection conditions, the collision process doesn't occur at the boundary.

A.3. Periodic Boundary Conditions

The periodic boundary conditions can be utilized in case of the infinite domain. They are implemented in the streamwise direction by treating nodes on inflow and outflow faces as nearest neighbours if they share common y and z coordinates. With this convention, the streaming operation automatically defines the population on all incoming links at the end of lattice. Imposing periodic as a natural part of the streaming operations; outgoing populations at the end the lattice become incoming populations at the other end. For example: at the left end ($y=0$) and right end ($y=N_y-1$) in which N_y is the number of lattices in y -direction, the following zero derivative condition is imposed after the collision steps:

$$f_k^{\text{out}}(x, 0, z, t) = f_k^{\text{in}}(x - \Delta x, Ny, z - \Delta z, t) \quad (7)$$

The periodic boundary conditions should satisfy the conservation of mass and the conservation of momentum.

REFERENCES

- [1] S. Chen, G. D. Doolen, Lattice Boltzmann Method for Fluid Flows, *Annu. Rev. Fluid Mech*, 30 (1998)329-364.
- [2] S.Succi, *The Lattice Boltzmann Equation for Fluid Dynamics and Beyond*, Oxford Science Publications, UK (2001).
- [3] D. Bouzidi, M. hamed, D. D'huimières, P. Lallemand, L. Luo, Lattice Boltzmann Equation on a Two-Dimensional Rectangular Grid, *Journal of Computational Physics* 172.2 (2001) : 704-17.
- [4] D. O. Martínez, W. H. Matthaeus, S. Chen, D. C. Montgomery, Comparison of Spectral Method and Lattice Boltzmann Simulations of Two-dimensional Hydrodynamics, *Physics of Fluids* 6.3 (1994): 1285.
- [5] G.Házi, C. Jiménez, Simulation of Two-dimensional Decaying Turbulence Using the “incompressible” Extensions of the Lattice Boltzmann Method, *Computers & Fluids* 35.3 (2006) : 280-303.
- [6] R. Benzi, S. Succi, Two-dimensional Turbulence with the Lattice Boltzmann Equation, *Journal of Physics A: Mathematical and General* 23.1 (1990): L1-L5.
- [7] K.Rothman, D.Daniel, S. Zaleski, Lattice-Gas Models of Phase Separation: Interfaces, Phase Transitions and Multiphase Flow, *Reviews of Modern Physics* 66.4 (1994): 1417-479.
- [8] X.Shan, H. Chen, Lattice Boltzmann Model for Simulating Flows with Multiple Phases and Components, *Physical Review E* 47.3 (1993): 1815-819.
- [9] W.Swift, M. Sukop, W. Osborn, J. Yeomans, Lattice Boltzmann Simulation of Non-ideal Fluids, *Physical Review Letters* 75.5 (1995): 830-33.
- [10] H. Xiaoyi and G. D. Doolen, Thermodynamic Foundations of Kinetic Theory and Lattice Boltzmann Models for Multiphase Flows, *Journal of Statistical Physics* 107.1 (2002): 309-28.
- [11] H. Xiaoyi, L. Luo, Lattice Boltzmann Model for the Incompressible Navier–Stokes Equation, *Journal of Statistical Physics* 88.3/4 (1997): 927-44.
- [12] S. J. Almalowi, A. Öztekin, Flow Simulations Using Thermal Lattice Boltzmann Method, *Journal of Applied Mathematics*, 10.1155/(2012)/135173.
- [13] S. J. Almalowi, D. E. Oztekin, A. Oztekin, Rayleigh-Taylor Instability Studied with Multi-relaxation Lattice Boltzmann Method, *ASME 2013 International Mechanical Engineering Congress and Exposition, California, Nov.15-12,(2013)*.
- [14] M. McCracken, J. Abraham, Multiple-Relaxation-Time Lattice-Boltzmann Model for Multiphase Flow, *Physical Review E*, (2005) : vol. 71, No. 3.

- [15] T. Fukui, K. Morinishi, Application of Regularized Lattice Boltzmann Method for Incompressible Flow Simulation at High Reynolds Number and Flow with Curved Boundary, *Journal of Fluid Science and Technology*, (2011) : vol. 6, No. 6.
- [16] S. J. Almalawi, D.E. Oztekin, A. Oztekin, Regularized Multi-relaxation Lattice Boltzmann Method for Flow Past Square Cylinders, *Computers and Fluids*, (2013) (under review).
- [17] O. Martin, A. Odlyzko, S. Wolfram, Algebraic Properties of Cellular Automata, *Communications in Mathematical Physics*, (1984) : vol. 93 p.219-258.
- [18] D. A. Wolf-Gladrow, *Lattice-Gas Cellular Automata and Lattice Boltzmann Models - An Introduction*, Springer, June 26, (2005).
- [19] P.L. Bhatnagar, E.P. Gross, M. Krook, A Model for Collision Processes in Gases. I. Small Amplitude Processes in Charged and Neutral One-Component Systems, *Physical Review*, (1954) :94(3), 511-525.
- [20] D. O. Martinez, W. H. Matthaeus, S. Chen, D. C. Montgomery, Comparison of Spectral Method and Lattice Boltzmann Simulations of Two-Dimensional Hydrodynamics, *Physics of Fluids* vol. 6, p. (1994):1285–1298.
- [21] G. Hazi , C. Jimenez, Simulation of Two-Dimensional Decaying Turbulence Using the ‘Incompressible’ Extensions of the Lattice Boltzmann Method, *Computers & Fluids*, (2006) : vol. 35, No. 3, p. 280–303.
- [22] S. Chapman, T. G. Cowling, *The Mathematical Theory of Non-Uniform Gases*, Digital Edition, Cambridge Mathematical Library, (1999).
- [23] X. He, L. Luo, Lattice Boltzmann Model for the Incompressible Navier-Stokes Equation, *Journal of Statistical Physics*, (1997) : 88(3).
- [24] D. d’Humieres, Generalized Lattice Boltzmann Equations, In *Rarefied Gas Dynamics: Theory and Simulations*, (ed. B. D. Shizgal & D. P. Weaver). Prog. Aeronaut. Astronaut. (1992) : vol. 159, p. 450-458.
- [25] D. d’Humieres, I .Ginzburg, M. Krafczyk, P. Lallemand, L. Luo, Multiple-Relaxation-Time Lattice Boltzmann Models in Three Dimensions, *Philosophical Transactions Royal Society of London*, (2002): vol. 360, p. 437-451.
- [26] S. J. Almolawi, D. E. Oztekin, A. Oztekin, Numerical Simulations of Lid-Driven Cavity Flows using Multi-relaxation Time Lattice Boltzmann Method, *Engineering Applications of Computational Fluid Dynamics (Advanced Structured Materials)* (2014) : vol.44, edited by: Shaari, K., Zlati, K. and Mokhtar, A. Springer
- [27] J. Latt, B. Chopard, Lattice Boltzmann Method with Regularized Precollision Distribution Functions, *Mathematics and Computers in Simulation*, (2006) : vol.72, p. 165-168.

- [28] X. Shan, H. Chen, Lattice Boltzmann Model for Simulating Flows with Multiple Phases and Components, *Physical Review E*,(1993) : vol47(3), 1815-1819
- [29] H. Huang, Z. Li, S. Lui, Z. Lu, Shan-and-Chen-type Multiphase Lattice Boltzmann Study of Viscous Coupling Effects for Two-Phase Flow in Porous Media, *International Journal for Numerical Methods in Fluids*, (2009) : vol 61, 341-354
- [30] A. Kuzmin, A.A. Mohamad, Multirange Multi-relaxation Time Shan-Chen Model with Extended Equilibrium, *Computers and Mathematics with Applications*,(2010) : vol 59, 2260-2270
- [31] S. J. Almalowi, A.Oztekin, Two and Three Dimensions Lid-Driven Cavity Using D2Q9,D3Q15, and D3Q19, proceeding 6th International Conference on Advanced Computational Engineering and Experimenting, Istanbul-Turkey,(2012).
- [32] W. Regulski, J. Szumbariski, Numerical Simulation of Confined Flows Past Obstacles –The Comparative Study of Lattice Boltzmann And Spectral Element Methods, *Arch. Mech.*, (2012) : vol.164, 4, pp. 423–456.
- [33] Q. Zou and X. He, On Pressure and Velocity Boundary Conditions for the Lattice Boltzmann BGK Model, *Physics of Fluids*,(1997):vol.9,p.1591-1063.
- [34] L. S. Kuo, P. H. Chen, A Unified Approach for Nonslip and Slip Boundary Conditions in the Lattice Boltzmann Method,*Computers & Fluids*,(2008): vol. 38 p. 883-887.
- [35] S.J. Almalowi, Lattice Boltzmann Applied to Fluid Flow and Heated Lid-Driven 2D Square Lattice Dimension (D2Q9), Lehigh University (Thesis), (2012).
- [36] R.W. Davis, E F Moore, L. P. Purtell, A Numerical-Experimental Study of Confined Flow Around Rectangular Cylinders, *Physics of Fluids*, (1984) :vol. 27, No 1, p. 46–59.
- [37] D. Lyn ,W. Rodi, The Flapping Shear Layer Formed by Flow Separation from the Forward Corner of a Square Cylinder, *Journal of Fluid Mechanics*, (1994) : vol. 267, p. 353-376.
- [38] D. Lyn, S. Einav, W. Rodi, J. Park, A Laser Doppler Velocimetry Study of Ensemble-Averaged Characteristics of the Turbulent Near Wake of a Square Cylinder, *Journal of Fluid Mechanics*, (1995) : vol. 304, p. 285-319.
- [39] S. Murakami, A. Mochida, On Turbulent Vortex Shedding Flow Past 2D Square Cylinder Predicted by CFD,*Journal of Wind Engineering and Industrial Aerodynamics*, (1995) : vol. 54/55, p. 191-211.
- [40] D. Bouris, G. Bergeles, 2D LES of Vortex Shedding from a Square Cylinder, *Journal of Wind Engineering and Industrial Aerodynamics*, (1999) : vol. 80, p. 31-46.

- [41] J. S. Ochoa, N.Fueyo, Large Eddy Simulation of the Flow Past a SquareCylinder, Area de Meacanica de Fluidos, Centro Politecnico Superior, C/Maria de Luna 3 50018 Zaragoza, Spain.
- [42] W. Rodi, On the Simulation of Turbulent Flow Past Bluff Bodies, Journal of Wind Engineering and Industrial Aerodynamics, (1993) : vol. 46/47, p. 3-19.
- [43] R.Allen,T.Reis, A lattice Boltzmann model for natural convection in cavities, International Journal of Heat and Fluid, (2013).
- [44] A. Gupta, R. Kumar, Lattice Boltzmann simuulation to Study Multiple Bubble Dynamics, Int. J. of Heat and Mass Transfer, (2008):vol.51,5192-5203.
- [45] A. Gupta, R. Kumar, Two-Dimensional Lattice Boltzmann Model for Droplet Impingenment and Breakup in low density Ratio Liquids,Commun.Comput, (2011) : vol.10,No.3,pp767-784.
- [46] J.J. Huang, C. Shu, J.J. Feng, Y.T. Chew ,A Phase-Field Based Hybrid Lattice Boltzmann Finite-Volume Method and Its Application to Simulate Droplet Motion under Electro wetting Control, Journal of Adhesion Science and Technology,(2012) : vol.26,p.1825-1851.
- [47] H. Gu, M. H. G. Duits, F. Mugele, Droplets Formation and Merging in Two-Phase Flow Microfluidics, Int J Mol Sci.,(2011) : vol.12(4) : 2572–2597.
- [48] N. Azwadi, C. Sidik, M. Goudarzi, M. Afiq Witri, Prediction of the dynamics of droplet on solid surface using lattice Boltzmann method international review of Mechanical Engineering , (2011) : vol. 5, No.7.
- [49] S. F. Lunkad, V. V. Buwa, K.D.P. Nigam, Numerical simulations of drop impact and spreading on horizontal and inclined surfaces, Chemical Engineering Science (2007) : vol. 62, p7214 – 7224.
- [50] L. Amaya-Bower,T. Lee, Single bubble rising dynamics for moderate Reynolds number using Lattice Boltzmann Method, Computers& Fluids, (2010) :vol. 39,p. 1191-1207.
- [51] G. Bozzano, M. Dente, Shape and terminal velocity of single bubble motion: a novel approach, Computers and Chemical Engineering, (2001) : vol.25, p.571–576.
- [52] S. J. Almalowi, D. E. Oztekin, A.Oztekin, Computational Study of Droplets Rising Using Lattice Boltzmann Method, 10th international conference on Heat Transfer and Thermodynamics, Orlando, Florida; 14-16 July,(2014).
- [53] M. Cheng, J. Hua, J. Lou, Simulation of Bubble-Bubble Interaction Using a Lattice Boltzmann Method., Computers & Fluid, (2010) : vol.39, p.260-270
- [54] D. RM and S.Taylor GI, The Mechanics Of Large Bubbles Rising Through Extended Liquids In Tube, Proceeding of the Royal society, (1950) : vol.200,No.1062.

- [55] D.Rodrigue, Generalized correlation for bubble motion. *AICHe J*, (2001) : vol. 47, No. 47:39–44.
- [56] S. J. Almalowi, D.E. Oztekin ,A. Oztekin, Computational study of multi-phase flows using lattice Boltzmann model, *Canadian Journal of Physics*,(2014) (under review).
- [57] X. He, R. Zhang, S. Chen,G. D. Doolen, On The Three-Dimensional Rayleigh–Taylor Instability, *Physics of Fluids*, (1999) : vol.11,No.5.
- [58] S.J. Almalowi. D.E. Oztekin, Rayleigh-Taylor Instability Studied with Multi-relaxation Lattice Boltzmann Method, *J. Mechanics Engineering and Automation*, (2014): 4(5), p. 365-371.
- [59] X. He, S. Chen, R. Zhang, A Lattice Boltzmann Scheme for Incompressible Multiphase Flow and Its Application in Simulation of Rayleigh–Taylor Instability, *Journal*,(1999) : vol.152(2).
- [60] A. Parmigiani, Lattice Boltzmann Calculations of Reactive Multiphase Flows in Porous Media, thesis, (2010).
- [61] D. Chiappini, G. Bella¹, S.Succi, F. Toschi, S. Ubertini⁴, Improved Lattice Boltzmann Without Parasitic Currents for Rayleigh-Taylor Instability, (2010) : vol. 7, No. 3, p. 423-444.
- [62] S. H. Kim, H. Pitsch, On the Lattice Boltzmann Method for Multiphase flows, Center for Turbulence Research annual Research Briefs, (2009).
- [63] A. Banari, C. F. Janßen, S.T. Grilli, An Improved Two-Phase Lattice Boltzmann Model For High Density ratios: Application To Wave Breaking, University of Rhode Island, Department of Ocean Engineering, Narragansett, RI, USA.
- [64] H. Liu , A.J. Valocchi, Q. Kang,, Three-Dimensional Lattice Boltzmann Model For Immiscible Two-Phase Flow Simulations, *Physical Review*,(2012) E85, 046309.
- [65] C. F. Hou, C. Chang, K.H. Lin,C. An Lin, Consistent Boundary Conditions for 2D and 3D Lattice Boltzmann Simulations, *Tech Science Press*,(2009): vol.44,no.2,p.137-155.
- [66] H. Yu, L. Luo , S. S. Girimaji, LES of turbulent square jet flow using an MRT lattice Boltzmann model, *Computers & fluids*, (2006) : vol. 35,p 957-965.
- [67] P.A. Skordos, Initial And Boundary Conditions For The Lattice Boltzmann Method, *Phys Rev E* , (1993) : vol.48:4823-42.
- [68] M. C. Sukop, D. Or, Lattice Boltzmann Method For Modeling Liquid-Vapor Interface Configurations In Porous Media, *Water Resources Research*, (2004) : vol 40(1).
- [69] M. Sbragaglia, R. Benzi, L. Biferali, S. Succi, K. Sugiyama, F. Toschi, Generalized Lattice Boltzmann Method with Multirange Potential. *Phys. Rev.E*,(2007) : vol.75p.13.

Vita

Saeed J. Almalawi was born in the southern region of Saudi Arabia. He got his high school from Al-Fisal secondary school in Makkah province in 1999. He joined the College of Engineering at King Abdul-Aziz University in 2000. He got his Bachelor degree (2nd honor) from KAU in 2005 and joined Saline Water Conversion Corporation (SWCC). He spent two years and a half in SWCC before he joined Taibah University in 2007. He started working in the College of Engineering at Taibah University as Teaching Assistant (TA). He was awarded with a scholarship from Taibah University in 2009 to attend graduate program in USA. He joined Lehigh University, USA in 2010 and he received Master of Science degree in 2012 (GPA: 3.82/4). He joined a PhD program at Lehigh University in 2012. He has published more than eight journal articles and attended several international conferences inside and outside of USA.



UNITED STATES PATENT AND TRADEMARK OFFICE

UNITED STATES DEPARTMENT OF COMMERCE
United States Patent and Trademark Office
Address: COMMISSIONER FOR PATENTS
P.O. Box 1450
Alexandria, Virginia 22313-1450
www.uspto.gov

Table with 6 columns: APPLICATION NUMBER, FILING or 371(c) DATE, GRP ART UNIT, FIL FEE REC'D, ATTY. DOCKET NO, TOT CLAIMS, IND CLAIMS. Row 1: 14/475,108, 09/02/2014, 3748, 1600, 437666US8, 19, 3

CONFIRMATION NO. 9623

FILING RECEIPT



Date Mailed: 09/10/2014

22850
OBLON, SPIVAK, MCCLELLAND MAIER & NEUSTADT, L.L.P.
1940 DUKE STREET
ALEXANDRIA, VA 22314

Receipt is acknowledged of this non-provisional patent application. The application will be taken up for examination in due course. Applicant will be notified as to the results of the examination. Any correspondence concerning the application must include the following identification information: the U.S. APPLICATION NUMBER, FILING DATE, NAME OF APPLICANT, and TITLE OF INVENTION. Fees transmitted by check or draft are subject to collection. Please verify the accuracy of the data presented on this receipt. If an error is noted on this Filing Receipt, please submit a written request for a Filing Receipt Correction. Please provide a copy of this Filing Receipt with the changes noted thereon. If you received a "Notice to File Missing Parts" for this application, please submit any corrections to this Filing Receipt with your reply to the Notice. When the USPTO processes the reply to the Notice, the USPTO will generate another Filing Receipt incorporating the requested corrections

Inventor(s) Saeed J. Almalawi, Bethlehem, PA;

Applicant(s) Saeed J. Almalawi, Bethlehem, PA;

Power of Attorney: The patent practitioners associated with Customer Number 22850

Domestic Priority data as claimed by applicant
This appln claims benefit of 62/014,237 06/19/2014

Foreign Applications for which priority is claimed (You may be eligible to benefit from the Patent Prosecution Highway program at the USPTO. Please see http://www.uspto.gov for more information.) - None. Foreign application information must be provided in an Application Data Sheet in order to constitute a claim to foreign priority. See 37 CFR 1.55 and 1.76.

Permission to Access - A proper Authorization to Permit Access to Application by Participating Offices (PTO/SB/39 or its equivalent) has been received by the USPTO.

If Required, Foreign Filing License Granted: 09/09/2014

The country code and number of your priority application, to be used for filing abroad under the Paris Convention, is US 14/475,108

Projected Publication Date: 12/24/2015

Non-Publication Request: No

Early Publication Request: No